ORIENTATIONAL DYNAMICS OF WATER AT HYDROPHOBIC INTERFACES

By

Florian Figge

A DISSERTATION

Submitted to
Michigan State University
in partial fulfillment of the requirements
for the degree of

Physics – Doctor of Philosophy

2018

ABSTRACT

ORIENTATIONAL DYNAMICS OF WATER AT HYDROPHOBIC INTERFACES

By

Florian Figge

Water surfaces play an important role in many biological, chemical and physical processes. Many reactions occur at the water interface and some are even favored to happen there. Microscopically, many of the interfacial properties, such as the structure or dynamics of water molecules, are related to the termination of the dynamic hydrogen-bond network that is present in bulk water.

Time resolved pump-probe vibrational sum-frequency generation spectroscopy at the water/hydrophobic interface in combination with total internal reflection geometry allows the observation of the surface dynamics with a large signal-to-noise ratio. Pump and probe beams are both resonant with the surface-specific dangling OH stretch vibration. The pump-induced orientational anisotropy is measured by pumping with polarizations parallel and perpendicular to the probe polarization. The measurements show that the decay of the dangling OH stretch excitation is dominated by a 1.61 ± 0.10 ps jump to a hydrogen-bonded configuration. The dangling OH jump time at hydrophobic interfaces is twice as fast as a jump between hydrogen-bonded configurations in bulk water and about 50% slower than what is reported for the water/air interface.

Upon introduction of salt, changes in structure of water are observed in the bulk and at aqueous interfaces. This is reflected in macroscopic observables such as altered viscosity or surface tension. Moreover, research on bulk salt solutions shows significant changes in dynamics that, in some cases, extend beyond the first solvation shell and might be expected to alter the interfacial dynamics. However, our experiments suggest that the reorientation dynamics associated with the jump from a dangling to a bonded OH is not affected by the dissolved salts used in our research.

ACKNOWLEDGEMENTS

First of all, I would like to thank my advisor John McGuire. I have never met anybody this dedicated to research and science. I am very appreciative of his support, patience, guidance, and wisdom throughout the years.

I want to thank my fellow grad students Cheng Sun for the introduction to the lab and Yanhao Tang for many helpful discussions. Completing our research group, I want to thank postdoc Shunhao Xiao for the work that he put into the experimental setup that I eventually took over and was doing my dissertation research with.

A lot of appreciation goes out to the staff at the physics department of Michigan State University, especially secretary Kim Crosslan, the machine shop crew, Reza Loloee, and whoever paid for the pizza at the CORE-CM (Center of Research Excellence in Complex Materials) seminars.

I would like to thank my dear friends, close by and far away. Even though I have not seen many of them recently but I do not know what I would have done without them.

Of course, this list would be incomplete without my parents, Gabriele Göhringer and Manfred Figge. Without their unlimited support, I would be nowhere near where I am today. Their encouraging words via Skype were essential during grad school.

Last, but not least, I would like to thank my girlfriend Celina Wanek for her unconditioned love and support that ranged from keeping me fed to meeting me for little coffee dates during the day at times when I left our apartment in the early morning and did not return until midnight on a regular basis. Furthermore, I want to thank her for all the countless sacrifices that she has made during the last few years. I will never forget them.

TABLE OF CONTENTS

LIST OF TABLES

LIST OF FIGURES

CHAPTER 1

INTRODUCTION

The properties of water have fascinated humans for millennia, and many of its properties are well known from introductory physics and chemistry lessons. Compared to fluids of similar molecular size it provides us with a variety of interesting properties, including its phase transitions and density anomaly. For example, molecules made of hydrogen and elements surrounding oxygen in the periodic table are all gases at standard conditions (N, F, P, S, Cl). In contrast, water is of course liquid under the same conditions. Many of these unusual properties are due to the fact that water forms strong hydrogen bonds with four neighboring water molecules. These bonds, schematically displayed in figure 1.1, form due to the much larger electronegativity of oxygen compared to hydrogen.

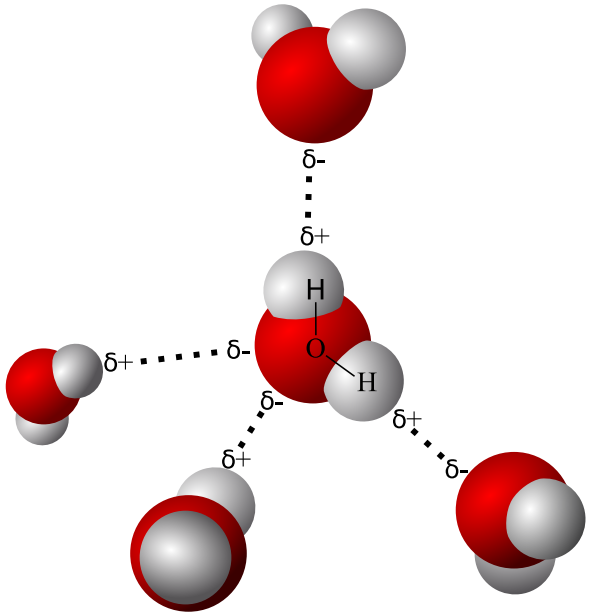

Figure 1.1: Polarization of a water molecule and the resulting hydrogen bonds with neighboring water molecules. The oxygen of the central water molecule is considered to be an acceptor of two hydrogen bonds (with the water molecules in the lower left corner of the figure) and a donor of two hydrogen bonds (with the water molecules in the top and the lower right corner of the figure).

1.1 Structure and orientational dynamics in bulk water

In bulk, a water molecule generally forms four hydrogen bonds with its neighboring water molecules. Focusing on the water molecule in the center of figure 1.1, the oxygen supplies two lone pairs of electrons that can each form a hydrogen bond with a hydrogen atom of an adjacent water molecule. Conversely, each hydrogen atom of the central water molecule can form a hydrogen bond with lone electron pairs of an oxygen atom of a neighboring water molecule. Throughout this dissertation this type of bond is called a bonded oxygen-hydrogen group or bOH. At room temperature, hydrogen bonds are very dynamic: They break and form rapidly and enable the bOH to reorient. The dynamics of bulk water has been studied in theory and experiment. Molecular dynamics (MD) simulations show that the reorientation of bOHs occurs with a large angular jump motion covering 68° on a 3.3ps time scale.[10] Further MD studies suggest that hydrogen atoms can participate in two hydrogen bonds simultaneously – they bifurcate – as an "old" hydrogen bond breaks and a "new" one forms.[11, 1] Experimentally, the orientational dynamics in bulk water can be accessed via infrared (IR) pump-probe spectroscopy by separately measuring the pump-induced change in absorption with pump and probe polarizations being parallel ($\Delta\alpha_{\parallel}$) and then orthogonal

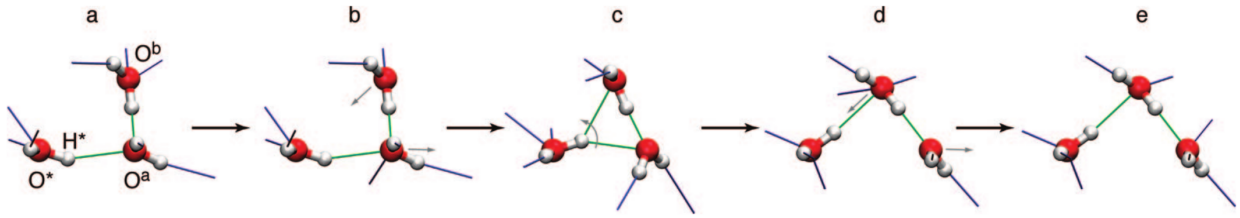

Figure 1.2: Schematic reorientation in bulk illustrated by Laage and Hynes[1]. a-b) Initially fluctuations lead to an overcoordinated water molecule (O^a) and an undercoordinated water molecule (O^b). The water molecules rearrange so that $\overline{O^*O^a} = \overline{O^*O^b}$ and therefore reach a symmetric configuration where both hydrogen-bond acceptors are energetically equivalent. c) During the transition state the original hydrogen bond $O^*H^* \cdots O^a$ bifurcates symmetrically. d-e) The formation of the new hydrogen bond and the breaking of the old hydrogen bond happen simultaneously which is accompanied by an angular jump of O^*H^*. The initial overcoordination of O^a and undercoordination of O^b are interchanged.

($\Delta\alpha_\perp$) with respect to each other. The rotational anisotropy can then be calculated[12, 13] to be

$$R(t) \equiv \frac{\Delta\alpha_\parallel(t) - \Delta\alpha_\perp(t)}{\Delta\alpha_\parallel(t) + 2\Delta\alpha_\perp(t)} = \frac{2}{5} C_2(t), \tag{1.1}$$

with the second-order Legendre polynomial orientational correlation function $C_2(t) = \langle P_2[\hat{\mu}(t) \cdot \hat{\mu}(0)] \rangle$ and the transition dipole $\hat{\mu}$. Since bulk water is an isotropic medium, the population dynamics can be easily disentangled from the orientational dynamics by performing pump-probe spectroscopy in a magic-angle geometry: Adjusting the angle between pump and probe polarizations to $\theta_m = \arccos \frac{1}{\sqrt{3}} \approx 54.7°$ has the effect that all interactions governed by the second order Legendre polynomial ($P_2(\cos 54.7°) = 0$), including orientational dynamics, cancel out and one measures the population dynamics directly. This is equivalent to measuring $\Delta\alpha_\parallel + 2\Delta\alpha_\perp$.

1.2 Structure and orientational dynamics at the water interface

At the water interface several issues arise that make its study more challenging. In order to study the interface, it is necessary to separate the surface from the bulk response. This rules out the possibility of obtaining the population dynamics of the system at the interface through a non-surface-specific magic angle measurement. Particularly, on the experimental side new approaches were needed.

At the interface with air or other hydrophobic matter the hydrogen bond network terminates and

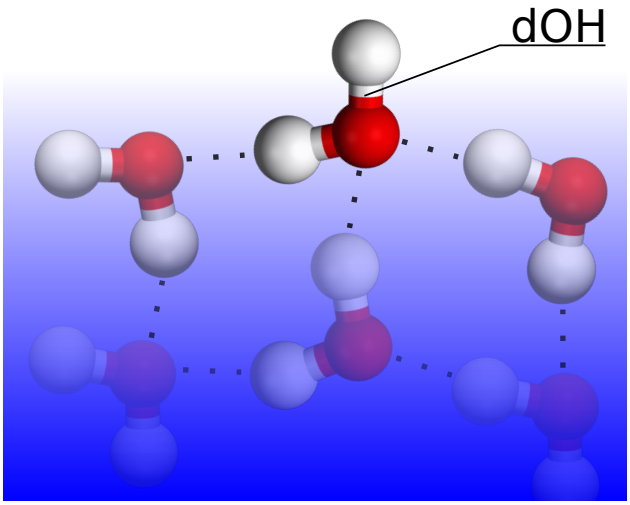

Figure 1.3: Dangling OH (dOH) at the water/air interface.

leaves behind dangling oxygen-hydrogen groups (dOH) on at least 20% of the water molecules at the surface.[14] A dOH is an OH group that by definition does not form hydrogen bonds with other water molecules. They stick out of the bulk, with the vector from the oxygen to the hydrogen atom pointing towards the air or the hydrophobic matter (figure 1.3). dOH groups can also briefly exist in bulk water for $< 200\,\text{fs}$ before they participate in a hydrogen bond with another water molecule again.[15] They can be neglected in our experiment due to their short lifetime and their on average random orientation. Looking at the vibrational OH stretch spectrum of water at an interface (figure 1.4), one can see a broad and a narrow feature. The broad feature is associated with bOH, and its width can be explained by the various strengths of hydrogen bonds with which a bOH can be involved. In general, the weaker the hydrogen bond is the higher the OH stretch vibrational frequency. Of course, this means that we will find the dOH feature, which is associated with OH groups that are not involved in any hydrogen bonds, at a higher, narrower range of frequencies compared to the bOH. In figure 1.4 we can also see that the spectrum of the water/air interface differs from the spectrum of the water/OTS interface. Although the interfaces with air and OTS are both considered to be hydrophobic interfaces, it is interesting to see such a significant difference in their spectra. This raises the question of whether the rotational dynamics of the dOH at those interfaces differ, too.

In deed, such a difference has been found theoretically: Stirnemann et al. [10] investigated the reorientation dynamics at a model hydrophobic surface with MD simulations. Their result puts the dOH reorientation time at $1.6\,\text{ps}$, which is in contrast to the $0.8 - 1.1\,\text{ps}$ reorientation time at the water/air interface obtained computationally by Vila Verde et al. [16] and experimentally by Hsieh et al. [17]. Even though the difference is significant, it is hard to distinguish the difference experimentally because of the challenge of obtaining a sufficiently high signal-to-noise ratio. This dissertation elaborates on how this problem can be solved.

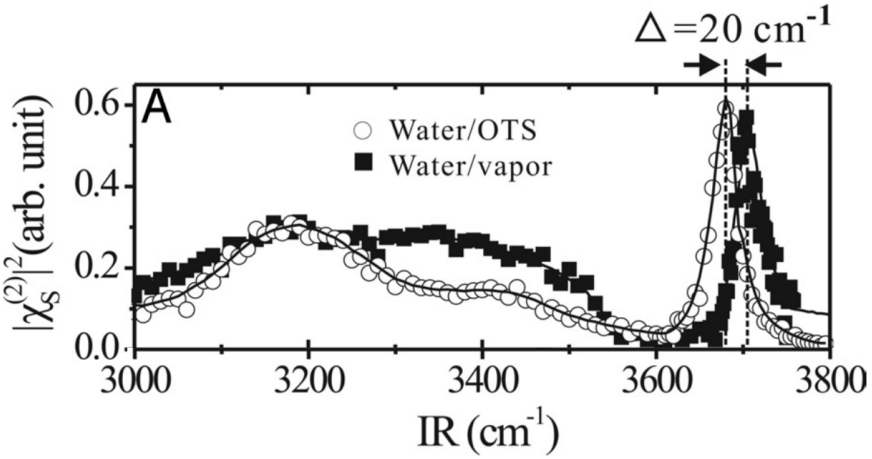

Figure 1.4: Water spectrum from C.S. Tian et al. showing the broad bOH feature ($3000-3600\,\mathrm{cm}^{-1}$) and narrow dOH feature at the interface with OTS ($3680\,\mathrm{cm}^{-1}$) and with air ($3695\,\mathrm{cm}^{-1}$).[2]

CHAPTER 2

THEORY

In order to measure the interfacial orientational dynamics of water, one needs a surface-specific probe. This can be understood easily because only after about 5 Å into the bulk water molecules adopt bulk properties.[18, 19] Sum-frequency generation, a second order process, is an established technique for this task. Its surface specificity is rooted in the fact that for systems with inversion symmetry, for example bulk water, the second order susceptibility vanishes in the electric-dipole approximation. Only at the surface, where inversion symmetry is broken, is the electric dipolar contribution to the second order susceptibility non-zero. The following section covers the theoretical aspects of sum-frequency generation (SFG) spectroscopy which allow the collection of surface-specific spectra. The connection is made between the orientational dynamics of a molecules and the orientational dynamics of the orientational distribution of vibrational excitations. In addition, I discuss how measurements in a total-internal reflection geometry can lead to an improved SFG signal compared to measurements at the interface between water and air. Moreover, this chapter introduces the concept of time-resolved pump-probe SFG that enables the measurement of dynamics at the interface and the challenge of separating population relaxation from orientational dynamics.

2.1 Light-matter interaction

Let's start with the macroscopic description of the light-matter interaction. In a dielectric medium an electric field **E** induces electric dipoles, whose density is described by the polarization density **P**, also just called polarization. For homogeneous and isotropic dielectrics the relationship between **E** and **P** is of linear and scalar nature:

$$\mathbf{P} = \varepsilon_0 \chi \mathbf{E} \tag{2.1}$$

The scalars ε_0 and χ are the electric constant and the electric susceptibility, respectively. The susceptibility is related to the relative permittivity by the following relationship:

$$\varepsilon_r = 1 + \chi \tag{2.2}$$

χ and ε_r are dimensionless and in general complex quantities. ε_r also determines the complex refractive index of a material:

$$\underline{n} = \sqrt{\varepsilon_r \mu_r}, \tag{2.3}$$

where μ_r is the relative permeability, which for many materials is ≈ 1. The real and imaginary parts of $\underline{n} = n + i\kappa$ are the refractive index n and the extinction coefficient κ, respectively: The latter is related to the attenuation coefficient $\alpha = 4\pi\kappa/\lambda_0$ with the vacuum wavelength λ_0, known from the Lambert's law describing the transmittance of a material sample of a given thickness l:

$$T(l) = \frac{I(l)}{I(0)} = \exp(-\alpha l), \tag{2.4}$$

where $I(l)$ is the light intensity after a sample thickness of l. In the case of anisotropic dielectrics, for which the polarization and the electric field are not in the same direction, the susceptibility in equation 2.1 becomes a tensor:

$$P_i = \varepsilon_0 \sum_j \chi_{ij} E_j \tag{2.5}$$

2.1.1 Non-linear polarization

In the presence of a sufficiently strong electric field, deviations from a linear response are seen. Assuming sufficiently weak fields and no permanent dipole moments, a Taylor series in $\mathbf{E}$ can describe the polarization:

$$P_i = P_i^{(1)} + P_i^{(2)} + P_i^{(3)} + \dots \tag{2.6}$$

$$= \varepsilon_0 \sum_j \chi_{ij}^{(1)} E_j + \varepsilon_0 \sum_{jk} \chi_{ijk}^{(2)} E_j E_k + \varepsilon_0 \sum_{jkl} \chi_{ijkl}^{(3)} E_j E_k E_l + \dots \tag{2.7}$$

We are especially interested in the second term, which is the source of polarization for sum-frequency generation spectroscopy and is described in the following section in more detail:

$$P_i^{(2)} = \varepsilon_0 \sum_{jk} \chi_{ijk}^{(2)} E_j E_k \tag{2.8}$$

From here on ε_0 is omitted to improve the readability, unless otherwise noted.

2.2 Sum-frequency generation spectroscopy

Sum-frequency generation (SFG) spectroscopy is a non-linear process where two laser beams with frequencies ω_1 and ω_2 overlap at a surface of a material or the interface between two materials and create an output beam with frequency $\omega_3 = \omega_1 + \omega_2$. More specifically, the two input photons at ω_1 and ω_2 are annihilated, while one output photon at ω_3 is created. For this second order process to be observed sufficiently intense laser beams have to interact with non-centrosymmetric matter, for example, surfaces or interfaces.

2.2.1 Surface specificity of SFG

For any system with inversion symmetry, for example bulk water, the second order polarization vanishes. This can be understood by the following proof. Consider the inversion operator I_{inv} that inverts any arbitrary vector $\mathbf{V}$: $I_{\text{inv}}\mathbf{V} = -\mathbf{V}$. Applying I_{inv} to the second order polarization then results in $I_{\text{inv}}\mathbf{P}^{(2)} = -\mathbf{P}^{(2)}$. Using the definition in equation 2.12 and the fact that for a centrosymmetric medium the electric susceptibility satisfies $I_{\text{inv}} \overleftrightarrow{\chi}^{(2)} = \overleftrightarrow{\chi}^{(2)}$ yields

$$I_{\text{inv}}\mathbf{P}^{(2)} = I_{\text{inv}} \left\{ \overleftrightarrow{\chi}^{(2)} \tilde{\mathbf{E}}_{\text{VIS}} \tilde{\mathbf{E}}_{\text{IR}} \right\} \tag{2.9}$$

$$= \mathbf{P}^{(2)} \tag{2.10}$$

From $-\mathbf{P}^{(2)} = \mathbf{P}^{(2)}$ one can deduce that $\mathbf{P}^{(2)} = 0$. The consequence is that the second order susceptibility has to vanish: $\overleftrightarrow{\chi}^{(2)} = 0$. By extension, all polarization terms of even order vanish in the electric-dipole approximation for systems with inversion symmetry. At interfaces this symmetry is broken, allowing a non-zero $\overleftrightarrow{\chi}^{(2)}$ and the generation of a second order signal.

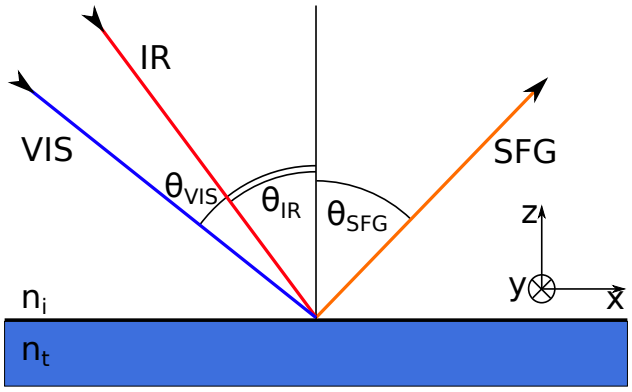

Figure 2.1: Sum-frequency generation at the interface between two media with respective refractive indices n_i and n_t.

2.2.2 Polarization and susceptibility

To further examine the properties of SFG, let us consider two electromagnetic plane waves $\tilde{\mathbf{E}}_n(\mathbf{r},t) = \mathbf{E}_n(\mathbf{r},t)\exp(-i\omega_n t) + c.c.$, where $\mathbf{E}_n(\mathbf{r},t) = \mathbf{A}_n(t)\exp(i\mathbf{k}_n\cdot\mathbf{r})$, with different frequencies ω_{VIS} and ω_{IR} to be incident onto a nonlinear medium with the second order susceptibility, a third rank tensor, $\overleftrightarrow{\chi}^{(2)}$ with the components $\chi^{(2)}_{ijk}$. The total electric field is

$$\tilde{\mathbf{E}}(\mathbf{r},t) = \tilde{\mathbf{E}}_{\text{VIS}}(\mathbf{r},t) + \tilde{\mathbf{E}}_{\text{IR}}(\mathbf{r},t) = \mathbf{E}_{\text{VIS}}(\mathbf{r},t)\exp(-i\omega_{\text{VIS}}t) + \mathbf{E}_{\text{IR}}(\mathbf{r},t)\exp(-i\omega_{\text{IR}}t) + c.c. \tag{2.11}$$

The resulting second order polarization is then of the form (and dropping $\mathbf{r}$ and t)

$$\begin{aligned}
\tilde{\mathbf{P}}^{(2)}(\mathbf{r},t) &= \overleftrightarrow{\chi}^{(2)}\tilde{\mathbf{E}}(\mathbf{r},t)^2 && && (2.12)\\
&= \overleftrightarrow{\chi}^{(2)}\left[\mathbf{E}^2_{\text{VIS}}\exp(-2i\omega_{\text{VIS}}t) + c.c.\right] && (SHG) && (2.13)\\
&+ \overleftrightarrow{\chi}^{(2)}\left[\mathbf{E}^2_{\text{IR}}\exp(-2i\omega_{\text{IR}}t) + c.c.\right] && (SHG) && (2.14)\\
&+ 2\overleftrightarrow{\chi}^{(2)}\left[\mathbf{E}_{\text{VIS}}\mathbf{E}_{\text{IR}}\exp(-i(\omega_{\text{VIS}}+\omega_{\text{IR}})t) + c.c.\right] && (SFG) && (2.15)\\
&+ 2\overleftrightarrow{\chi}^{(2)}\left[\mathbf{E}_{\text{VIS}}\mathbf{E}^*_{\text{IR}}\exp(-i(\omega_{\text{VIS}}-\omega_{\text{IR}})t) + c.c.\right] && (DFG) && (2.16)\\
&+ 2\overleftrightarrow{\chi}^{(2)}\left[\mathbf{E}_{\text{VIS}}\mathbf{E}^*_{\text{VIS}} + \mathbf{E}_{\text{IR}}\mathbf{E}^*_{\text{IR}}\right] && (OR) && (2.17)
\end{aligned}$$

The terms are grouped to illustrate the different interactions that contribute to the second order polarization. They are second harmonic generation (SHG), sum frequency generation (SFG),

difference frequency generation (DFG), and optical rectification (OR). All terms conserve energy and momentum. Looking specifically at the SFG term of the polarization, this means that $\hbar\omega_{\mathrm{SFG}} = \hbar\omega_{\mathrm{VIS}} + \hbar\omega_{\mathrm{IR}}$ and $\hbar\mathbf{k}_{\mathrm{SFG}} = \hbar\mathbf{k}_{\mathrm{VIS}} + \hbar\mathbf{k}_{\mathrm{IR}}$. Momentum and energy conservation can be used to separate the SFG signal from the other signals. This can be accomplished spectrally or for noncollinear input beams, spatially because each signal propagates in a different direction according to its momentum. Remembering that $\mathbf{E}_n(\mathbf{r},t) = \mathbf{A}_n(t)\exp(i\mathbf{k}_n \cdot \mathbf{r})$ one can rewrite the SFG polarization term

$$\mathbf{P}^{\mathrm{SFG}} = 2\overleftrightarrow{\chi}^{(2)}\left[\mathbf{E}_{\mathrm{VIS}}\mathbf{E}_{\mathrm{IR}}\exp\left(-i(\omega_{\mathrm{VIS}}+\omega_{\mathrm{IR}})t\right) + c.c.\right] \tag{2.18}$$

$$P_i^{\mathrm{SFG}} = 2\sum_{jk}\chi_{ijk}^{(2)}\left[E_{j,\mathrm{VIS}}E_{k,\mathrm{IR}}\exp\left(-i(\omega_{\mathrm{VIS}}+\omega_{\mathrm{IR}})t\right) + c.c.\right] \tag{2.19}$$

$$= 2\sum_{jk}\chi_{ijk}^{(2)}\left[A_{j,\mathrm{VIS}}A_{k,\mathrm{IR}}\exp\left(-i\omega_{\mathrm{SFG}}t + i\mathbf{k}_{\mathrm{SFG}}\cdot\mathbf{r}\right) + c.c.\right] \tag{2.20}$$

where the indices i, j, k are the Cartesian components of the fields.

2.2.3 Connection between macroscopic and microscopic description

The second order susceptibility in equation 2.19 can be described with a resonant and a non-resonant term labeled $\chi_R^{(2)}$ and $\chi_{NR}^{(2)}$, respectively:[20]

$$\chi_{ijk}^{(2)} = \chi_{NR,ijk}^{(2)} + \chi_{R,ijk}^{(2)} = \chi_{NR,ijk}^{(2)} + \left\langle \alpha_{ijk}^{(2)}(\omega_{IR})\right\rangle_{\mathbf{\Omega}} \tag{2.21}$$

The resonant part of the macroscopic susceptibility $\chi_R^{(2)}$ is related to the microscopic level by the ensemble average $\langle\ldots\rangle_{\mathbf{\Omega}}$ of the molecular hyperpolarizability tensor[21]

$$\alpha_{ijk}^{(2)}(\omega_{IR}) = \sum_q \frac{(\hat{\boldsymbol{i}}\cdot\overleftrightarrow{\alpha}(\Omega)\cdot\hat{\boldsymbol{j}})(\boldsymbol{\mu}(\Omega)\cdot\hat{\boldsymbol{k}})}{\omega_{IR}-\omega_q+i\Gamma_q} \tag{2.22}$$

with the molecular orientation $\Omega(t) = (\theta(t),\phi(t))$, the Raman polarizability tensor $\overleftrightarrow{\alpha}$, the dipole derivative $\boldsymbol{\mu}$, the frequency of the IR beam ω_{IR}, the resonant frequency ω_q and damping constant Γ_q of the q-th vibrational mode. Within this dissertation the IR laser is resonant with the vibrational stretch mode of the dangling OH. Therefore, by dropping the sum over all vibrational modes, the

resonant term becomes:

$$\chi^{(2)}_{R,ijk} = \frac{\left\langle (\hat{\boldsymbol{i}} \cdot \overleftrightarrow{\alpha}(\Omega_t) \cdot \hat{\boldsymbol{j}})(\boldsymbol{\mu}(\Omega_t, \omega_q) \cdot \hat{\boldsymbol{k}}) \right\rangle_{\boldsymbol{\Omega}}}{\omega_{IR} - \omega_{dOH} + i\Gamma_{dOH}} \tag{2.23}$$

2.2.4 Measured SFG intensity

A quantitative treatment of the nonlinear response requires that we take into account that the media that form the interface have different indices of refraction. In that case the intensity of the sum frequency signal created by the polarization is

$$I_{\mathrm{SFG}} = \frac{\omega^2_{\mathrm{SFG}}}{8\varepsilon_0 c^3 n_i(\omega_{\mathrm{SFG}}) n_i(\omega_{\mathrm{VIS}}) n_i(\omega_{\mathrm{IR}}) \cos^2(\theta_{\mathrm{SFG}})} \left|\chi^{(2)}_{\mathrm{eff}}\right|^2 I_{\mathrm{VIS}} I_{\mathrm{IR}}. \tag{2.24}$$

where $\chi^{(2)}_{\mathrm{eff}}$ is the effective surface nonlinear susceptibility:

$$\chi^{(2)}_{\mathrm{eff}} = [\mathbf{L}_{\mathrm{SFG}} \cdot \hat{\mathbf{e}}_{\mathrm{SFG}}] \cdot \overleftrightarrow{\chi}^{(2)} : [\mathbf{L}_{\mathrm{VIS}} \cdot \hat{\mathbf{e}}_{\mathrm{VIS}}] [\mathbf{L}_{\mathrm{IR}} \cdot \hat{\mathbf{e}}_{\mathrm{IR}}]. \tag{2.25}$$

$\hat{\mathbf{e}}_j$ is the unit polarization vector of the optical field at ω_j, and $\mathbf{L}(\omega_j)$ are the local field corrections (the transmission Fresnel factors), which are covered in more detail during section 2.2.6. But first, let us address how the polarization of the laser beams affects $\chi^{(2)}_{\mathrm{eff}}$.

2.2.5 Laser beam polarization and non-zero tensor elements of $\chi^{(2)}$

A common way to describe the polarization of laser beams is if they are parallel ("p-polarized") or perpendicular ("s-polarized") to the optical plane. Using the coordinate system in figure 2.1 to describe the direction of the polarization, "s" polarization is parallel to the y-axis. Consider, for example, an s-polarized ($\hat{\mathbf{e}}_{\mathrm{SFG}} = \hat{\mathbf{e}}_y$) SFG term in equation 2.25:

$$\mathbf{L}_{\mathrm{SFG}} \cdot \hat{\mathbf{e}}_{\mathrm{SFG}} = L_{yy,\mathrm{SFG}} \hat{\mathbf{e}}_y \cdot \hat{\mathbf{e}}_y = L_{yy,\mathrm{SFG}} \tag{2.26}$$

In contrast, since a "p"-polarized beam has polarization components in the x-z plane ($\hat{\mathbf{e}}_{\mathrm{SFG}} = -\cos(\theta_{\mathrm{SFG}})\hat{\mathbf{e}}_x + \sin(\theta_{\mathrm{SFG}})\hat{\mathbf{e}}_z$) the SFG term in 2.25 would have two contributions to the Fresnel transmission factor:

$$\mathbf{L}_{\mathrm{SFG}} \cdot \hat{\mathbf{e}}_{\mathrm{SFG}} = -L_{xx,\mathrm{SFG}} \cos(\theta_{\mathrm{SFG}}) + L_{zz,\mathrm{SFG}} \sin(\theta_{\mathrm{SFG}}) \tag{2.27}$$

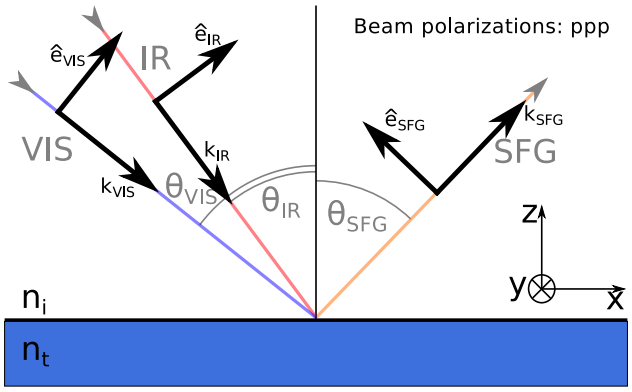

Figure 2.2: Illustration of the direction of beam polarizations for the polarization combination ppp.

The minus sign originates in the fact that the x-component of $\hat{\mathbf{e}}_{\mathrm{SFG}}$ is pointing in the negative x-direction, as visualized in figure 2.2. In the experiment the beam polarization combinations ssp (denoting the polarization of the SFG signal, the VIS and the IR beam, respectively) and ppp (analogously: SFG, VIS and IR all polarized in p-direction) are used. The effective susceptibility for the polarization combination ssp can be calculated using the previous examples and equation 2.25:

$$\chi^{(2)}_{\mathrm{eff,ssp}} = L_{yy,\mathrm{SFG}} \cdot L_{yy,\mathrm{VIS}} \cdot L_{xx,\mathrm{IR}} \cdot \cos\theta_{\mathrm{IR}} \cdot \chi^{(2)}_{yyx} + L_{yy,\mathrm{SFG}} \cdot L_{yy,\mathrm{VIS}} \cdot L_{zz,\mathrm{IR}} \cdot \sin\theta_{\mathrm{IR}} \cdot \chi^{(2)}_{yyz} \quad (2.28)$$

However, the water interface has $C_{\infty,v}$ symmetry, which reduces the 27 elements of the second-order susceptibility tensor to just four distinct non-zero elements:

$$\chi^{(2)}_{zxx} = \chi^{(2)}_{zyy}, \quad \chi^{(2)}_{xzx} = \chi^{(2)}_{yzy}, \quad \chi^{(2)}_{xxz} = \chi^{(2)}_{yyz}, \quad \chi^{(2)}_{zzz}, \quad (2.29)$$

where we have taken the z-axis to be parallel to the surface normal. Since $\chi^{(2)}_{yyx} = 0$, the effective susceptibility $\chi^{(2)}_{\mathrm{eff,ssp}}$ in equation 2.28 simplifies to only one term:

$$\chi^{(2)}_{\mathrm{eff,ssp}} = L_{yy,\mathrm{SFG}} \cdot L_{yy,\mathrm{VIS}} \cdot L_{zz,\mathrm{IR}} \cdot \sin\theta_{\mathrm{IR}} \cdot \chi^{(2)}_{yyz} \quad (2.30)$$

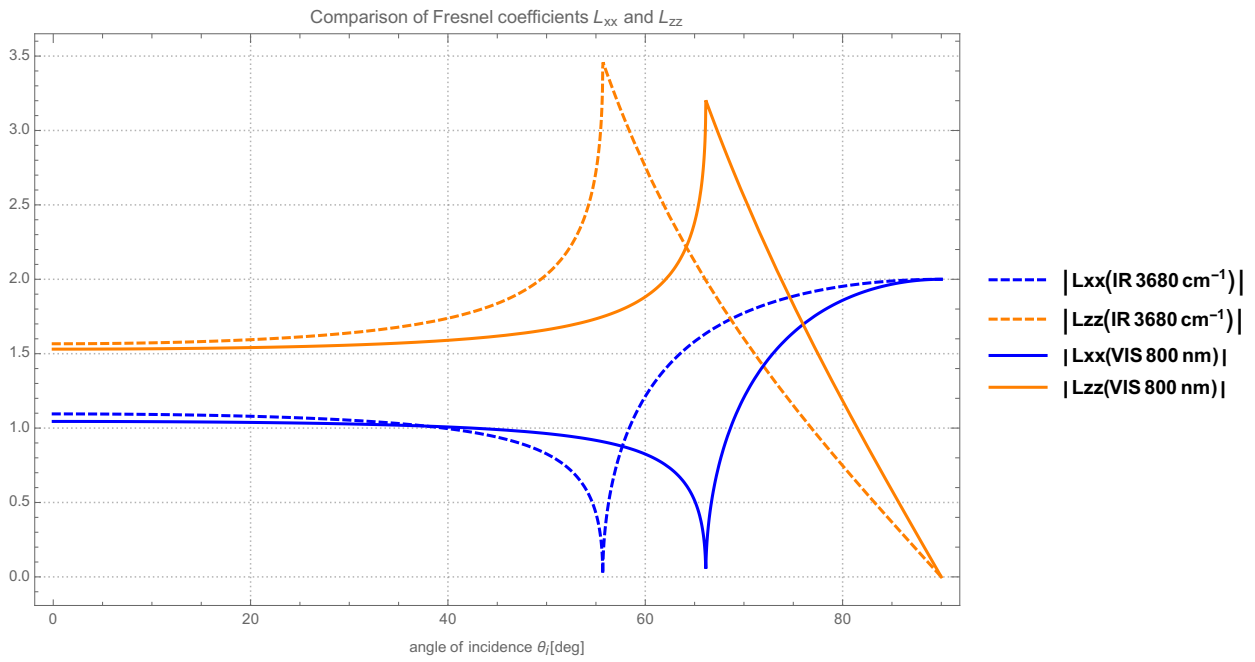

Figure 2.3: Comparison of the Fresnel coefficients L_{zz} and L_{xx} at the water-OTS-FS interface.

Analogously, for the polarization combination ppp, the effective susceptibility $\chi^{(2)}_{\text{eff,ppp}}$ simplifies from $2^3 = 8$ terms to four non-zero terms:

$$\chi^{(2)}_{\text{eff,ppp}} = -L_{xx,\text{SFG}} \cdot L_{xx,\text{VIS}} \cdot L_{zz,\text{IR}} \cdot \cos\theta_{\text{SFG}} \cdot \cos\theta_{\text{VIS}} \cdot \sin\theta_{\text{IR}} \cdot \chi^{(2)}_{xxz} \tag{2.31}$$

$$-L_{xx,\text{SFG}} \cdot L_{zz,\text{VIS}} \cdot L_{xx,\text{IR}} \cdot \cos\theta_{\text{SFG}} \cdot \sin\theta_{\text{VIS}} \cdot \cos\theta_{\text{IR}} \cdot \chi^{(2)}_{xzx} \tag{2.32}$$

$$+L_{zz,\text{SFG}} \cdot L_{xx,\text{VIS}} \cdot L_{xx,\text{IR}} \cdot \sin\theta_{\text{SFG}} \cdot \cos\theta_{\text{VIS}} \cdot \cos\theta_{\text{IR}} \cdot \chi^{(2)}_{zxx} \tag{2.33}$$

$$+L_{zz,\text{SFG}} \cdot L_{zz,\text{VIS}} \cdot L_{zz,\text{IR}} \cdot \sin\theta_{\text{SFG}} \cdot \sin\theta_{\text{VIS}} \cdot \sin\theta_{\text{IR}} \cdot \chi^{(2)}_{zzz} \tag{2.34}$$

For large incident angles θ_{VIS} and θ_{IR}, the exit angle of the SFG beam, θ_{SFG}, becomes large too. This enhances the $\chi^{(2)}_{zzz}$ component compared to the other three contributions to the effective susceptibility. In the next chapter it will become apparent that the Fresnel coefficient L_{xx} approaches zero (figure 2.3) at the angle of total internal reflection and one can approximate:

$$\chi^{(2)}_{\text{eff,ppp}} \approx L_{zz,\text{SFG}} \cdot L_{zz,\text{VIS}} \cdot L_{zz,\text{IR}} \cdot \sin\theta_{\text{SFG}} \cdot \sin\theta_{\text{VIS}} \cdot \sin\theta_{\text{IR}} \cdot \chi^{(2)}_{zzz} \tag{2.35}$$

The Fresnel coefficients L_{xx}, L_{yy} and L_{zz} are derived and their role for our experiment discussed in more detail in section 2.2.6.

2.2.6 Fresnel equations and transmission coefficients

The Fresnel equations determine the transmission and reflection coefficients of an electromagnetic wave at an interface between two non-magnetic media ($\mathbf{B} = \mathbf{H}$). Consider an incident, a reflected and a transmitted electromagnetic wave with:

$$\mathbf{E_i} = \mathbf{E_i^0} \exp(i(\mathbf{k}_i \cdot \mathbf{r} - \omega t)) \qquad \mathbf{H_i} = \frac{n_1}{k_i} \mathbf{k}_i \times \mathbf{E}_i \tag{2.36}$$

$$\mathbf{E_r} = \mathbf{E_r^0} \exp(i(\mathbf{k}_r \cdot \mathbf{r} - \omega t)) \qquad \mathbf{H_r} = \frac{n_1}{k_r} \mathbf{k}_r \times \mathbf{E}_r \tag{2.37}$$

$$\mathbf{E_t} = \mathbf{E_t^0} \exp(i(\mathbf{k}_t \cdot \mathbf{r} - \omega t)) \qquad \mathbf{H_t} = \frac{n_1}{k_t} \mathbf{k}_t \times \mathbf{E}_t \tag{2.38}$$

The directions of the reflected and transmitted beams can be easily determined ($\theta_i = \theta_r$ and Snell's law $n_i \sin\theta_i = n_t \sin\theta_t$). To determine the field amplitudes one needs to look at the boundary conditions:

$$(\mathbf{E}_i + \mathbf{E}_r) \times \mathbf{n} = \mathbf{E}_t \times \mathbf{n} \tag{2.39}$$

$$(\mathbf{H}_i + \mathbf{H}_r) \times \mathbf{n} = \mathbf{H}_t \times \mathbf{n}, \tag{2.40}$$

where $\mathbf{n}$ is the unit normal vector of the interface pointing into medium 2. In experiments the fields are usually either s or p polarized.

2.2.6.1 s-polarized light

In the case of s-polarized light the electric field is perpendicular to the optical plane. The first boundary condition gives:

$$E_i^0 + E_r^0 = E_t^0 \tag{2.41}$$

Using the relationships between **E** and **H**, the second boundary condition can be rewritten with the use of expansion of the triple product in the following form:

$$\mathbf{n}\times(\mathbf{k}_i\times\mathbf{E}_i)+\mathbf{n}\times(\mathbf{k}_r\times\mathbf{E}_r)=\mathbf{n}\times(\mathbf{k}_t\times\mathbf{E}_t) \tag{2.42}$$

$$\mathbf{k}_i(\mathbf{n}\cdot\mathbf{E}_i)-\mathbf{E}_i(\mathbf{n}\cdot\mathbf{k}_i)+\mathbf{k}_r(\mathbf{n}\cdot\mathbf{E}_r)-\mathbf{E}_r(\mathbf{n}\cdot\mathbf{k}_r)=\mathbf{k}_t(\mathbf{n}\cdot\mathbf{E}_t)-\mathbf{E}_t(\mathbf{n}\cdot\mathbf{k}_t) \tag{2.43}$$

$$\mathbf{E}_i(\mathbf{n}\cdot\mathbf{k}_i)+\mathbf{E}_r(\mathbf{n}\cdot\mathbf{k}_r)=\mathbf{E}_t(\mathbf{n}\cdot\mathbf{k}_t) \tag{2.44}$$

$$\mathbf{E}_i k_i\cos\theta_i+\mathbf{E}_r k_r\cos\theta_r=\mathbf{E}_t k_t\cos\theta_t \tag{2.45}$$

Using the fact that momentum parallel to the surface is conserved ($k_i\sin\theta_i=k_r\sin\theta_r=k_t\sin\theta_t$), which is more commonly known in the form of Snell's law ($n_i\sin\theta_i=n_t\sin\theta_t$), and $\theta_r=\theta_i$:

$$k_i=k_r \tag{2.46}$$

$$\frac{k_t}{k_i}=\frac{n_t}{n_i} \tag{2.47}$$

$$\left(E_i^0-E_r^0\right)\cos\theta_i=\frac{n_t}{n_i}E_t^0\cos\theta_t \tag{2.48}$$

Combining the two boundary conditions (equ. 2.41, 2.48), one can solve for E_r and E_t:

$$E_r^0=\frac{\sin(\theta_t-\theta_i)}{\sin(\theta_t+\theta_i)}E_i^0=r_S E_i^0 \tag{2.49}$$

$$E_t^0=\frac{2\cos\theta_i\sin\theta_t}{\sin(\theta_t-\theta_i)}E_i^0=t_S E_i^0 \tag{2.50}$$

The dependence on θ_t of the coefficient t_S can be easily eliminated by using Snell's law. One obtains the following relationship which is typically denoted as L_{yy} in the literature:

$$L_{yy}=\frac{2\cos\theta_i\sin\theta_t}{\sin(\theta_t-\theta_i)}. \tag{2.51}$$

2.2.6.2 p-polarized light

If the light is p-polarized, the E-field is parallel to the optical plane (x-z plane) and the H-field points out of the optical plane. Essentially the roles of E and H have been interchanged. Knowing this, one can use the result from the s-polarized case to write down the two boundary conditions

$(H_j^0 = n_j E_j^0)$:

$$n_i \left(E_i^0 + E_r^0 \right) = n_t E_t^0 \tag{2.52}$$

$$\left(E_i^0 - E_r^0 \right) \cos\theta_i = E_t^0 \cos\theta_t . \tag{2.53}$$

Solving for E_r and E_t yields:

$$E_r^0 = \frac{\tan(\theta_t - \theta_i)}{\tan(\theta_t + \theta_i)} E_i^0 = r_P E_i^0 \tag{2.54}$$

$$E_t^0 = \frac{2\cos\theta_i \sin\theta_t}{\sin(\theta_i + \theta_t)\cos(\theta_i - \theta_t)} E_i^0 = t_P E_i^0 . \tag{2.55}$$

The Fresnel coefficients for the electric field projections in x and z directions, r_{xx}, r_{zz}, t_{xx} and t_{zz} can be easily obtained. Here we are only interested in the transmission coefficients:

$$E_t^{xx} = E_t^0 \cos\theta_t \tag{2.56}$$

$$= t_P E_i^0 \cos\theta_t \tag{2.57}$$

$$= t_P \frac{E_i^{xx}}{\cos\theta_i} \cos\theta_t \tag{2.58}$$

$$= t_{xx} E_i^{xx} . \tag{2.59}$$

where $t_{xx} = t_P \frac{\cos\theta_t}{\cos\theta_i}$. Analogously, one can derive $t_{zz} = t_P \frac{\sin\theta_t}{\sin\theta_i}$. When using the typical notation for SFG spectroscopy, t_{xx} and t_{zz} are denoted as L_{xx} and L_{zz}, respectively.

$$L_{xx} = \frac{2\cos\theta_i \sin\theta_t}{\sin(\theta_i + \theta_t)\cos(\theta_i - \theta_t)} \frac{\cos\theta_t}{\cos\theta_i} \tag{2.60}$$

$$L_{zz} = \frac{2\cos\theta_i \sin\theta_t}{\sin(\theta_i + \theta_t)\cos(\theta_i - \theta_t)} \frac{\sin\theta_t}{\sin\theta_i} \tag{2.61}$$

2.2.6.3 Fresnel coefficients at the angle of total internal reflection

In our experiment we have chosen the water-fused silica (FS) interface in the form of a prism over the water-air interface because significant signal enhancements can be made by operating with a beam geometry that is close to the angle of total internal reflection (TIR). TIR is not possible at the water-air interface because $n_i < n_t$. At the water-FS interface $n_i > n_t$, so signal enhancement through

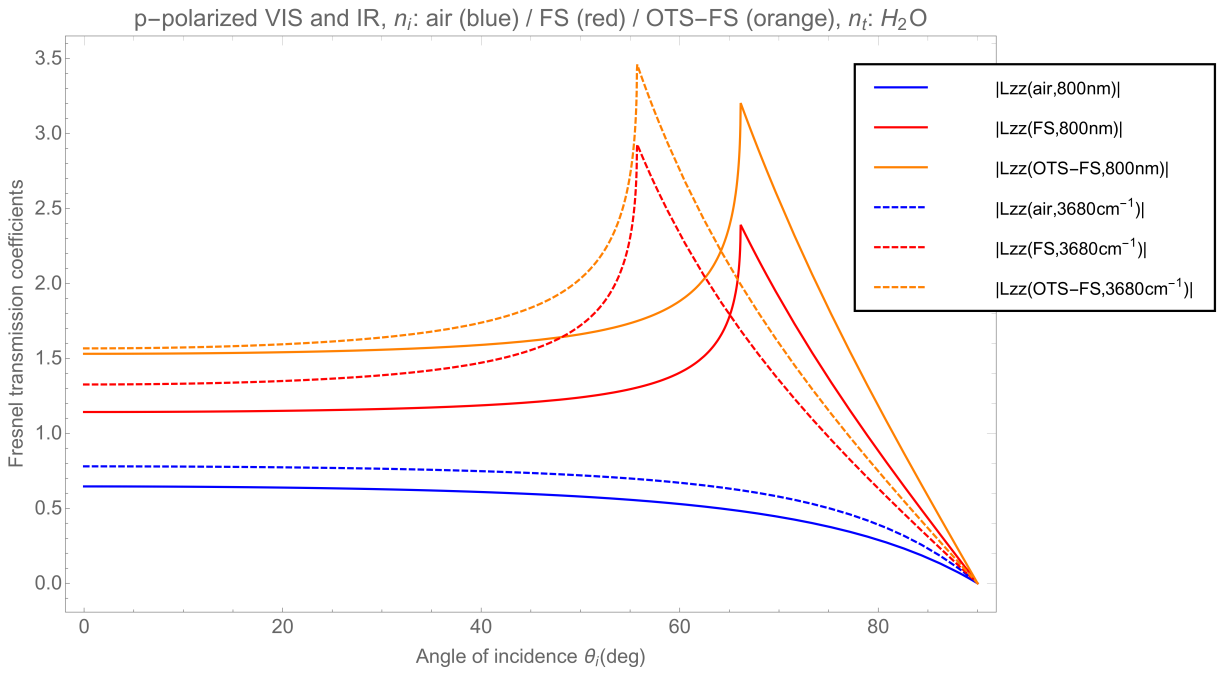

Figure 2.4: Fresnel transmission coefficients L_{zz} for p-polarized VIS at 800 nm (solid plots) and p-polarized IR at 3680 cm^{-1} (dashed plots). The blue plots describe the coefficient for the water-air interface. The red plots describe the coefficient for the water-FS interface. The orange plots describe the coefficients for the water-OTS-FS interface. Note that $|L_{zz}|$ for SFG would be essentially the same as L_{zz} for VIS. This is due the fact that L_{zz} depends on indices of refraction which are only weakly wavelength-dependent between $\lambda_{SFG} = 618$ nm and $\lambda_{VIS} = 800$ nm for water and OTS-FS.

TIR is possible. For example, at 800 nm the refractive indices are $n_i = 1.4533$ and $n_t = 1.3290$. Figure 2.4 shows the angle-dependence of the Fresnel coefficients and gives an estimate of how much the signal is boosted compared to the water-air interface. Nevertheless, FS is considered, as opposed to air, a hydrophilic material that forms hydrogen bonds with water. Since we are interested in investigating the dangling OH it is necessary to create a hydrophobic interface. This is accomplished by coating the FS prism with an octadecyltrichlorosilane (OTS) self-assembled monolayer (SAM).

For our purposes, another advantage of this configuration is the absolute magnitude of the Fresnel transmission coefficients L_{zz} and L_{xx}. In figure 2.3 it can be seen that at the angle of TIR, where L_{zz} has its maximum, L_{xx} approaches zero. We can therefore neglect all terms of $\chi^{(2)}_{\text{eff,ppp}}$ that contain

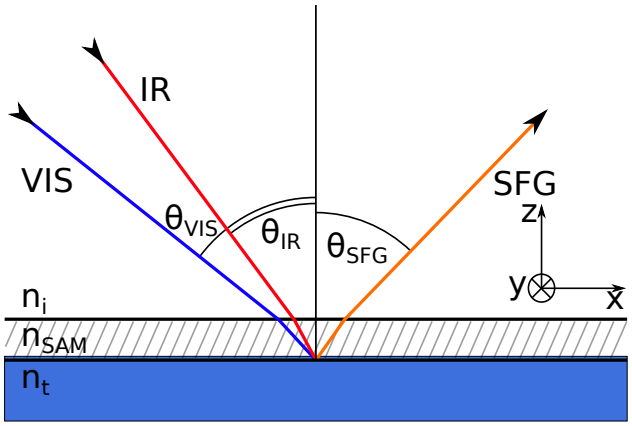

Figure 2.5: Sum-frequency generation at the interface of a monolayer and the medium below.

L_{xx} and arrive at equation 2.35. This means if we use the polarization combination ppp, for SFG, VIS and IR, respectively, the only significant contribution to the sum-frequency signal is going to be from $\chi^{(2)}_{zzz}$:

$$\chi^{(2)}_{\text{eff,ppp}} \propto \chi^{(2)}_{zzz} \tag{2.62}$$

2.2.6.4 Fresnel coefficients for experiments involving a monolayer

Now let's look closer at the case where the FS prism is coated with a monolayer, separating the FS and water shown in figure 2.5. In this case, the Fresnel coefficients need to be modified slightly by introducing a factor for the coefficient describing the relative field amplitude in the z-direction (perpendicular to the monolayer)[22], resulting in:

$$L^{SAM}_{zz} = L_{zz}\frac{n_t^2}{n^2_{SAM}} \tag{2.63}$$

where n_{SAM} can be approximated to be

$$n^2_{SAM} = \frac{n_t^2(n_t^2+5)}{4n_t^2+2} \tag{2.64}$$

The angle dependence of $|L_{zz}|$ for different water interfaces (water/air, water/FS, water/SAM/FS) is shown in figure 2.4 for VIS and IR light.

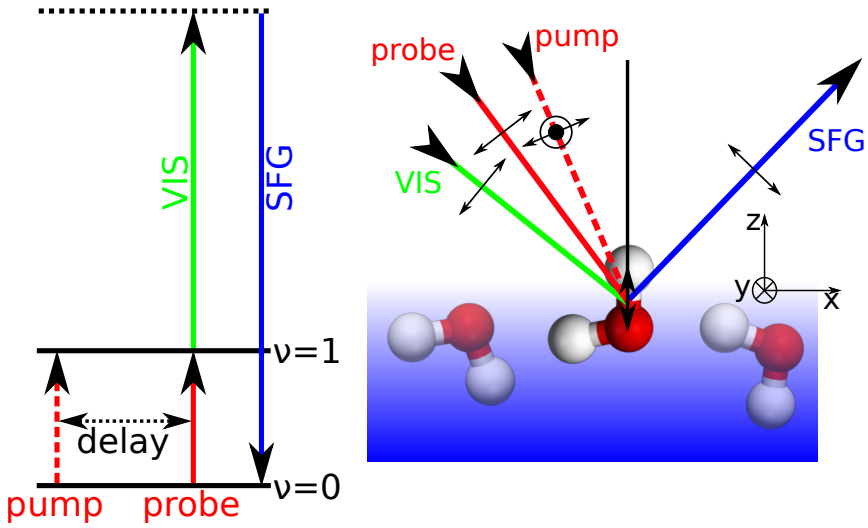

Figure 2.6: Schematic of time-resolved SFG spectroscopy using an additional IR pump beam. The probe SFG polarization is ppp. The pump polarization can be changed from p to s with a waveplate.

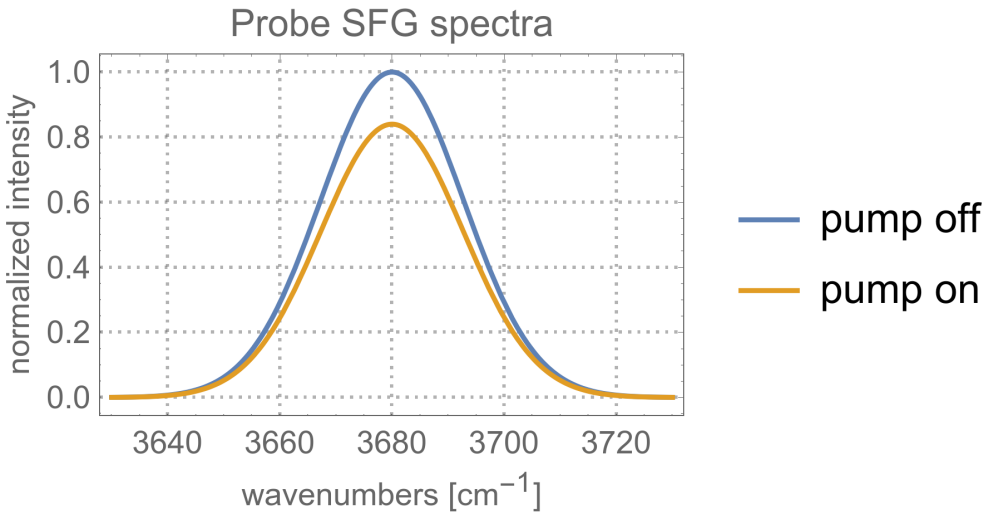

Figure 2.7: Schematic probe SFG spectra for pump-off ($I^{\text{off}}(\lambda;t_k)$) and pump-on ($I^{\text{on}}(\lambda;t_k)$) at a pump-probe delay of t_k.

2.3 Time- and polarization-resolved SFG spectroscopy

In order to research the dynamics of the water interface, we use time-resolved SFG spectroscopy by employing a pump beam with polarization and delay with respect to the probe beam that can be varied through a delay stage and a waveplate (figure 2.6). The pump to excites the water molecules from the ground state $v = 0$ to the first excited state $v = 1$ of the dangling vibrational stretch mode which leads to a decrease or bleach in probe SFG signal. The anharmonicity of the dOH stretch vibration is such that the excited state transition $v = 1 \rightarrow 2$ is redshifted by 90 cm^{-1} relative to the $v = 0 \rightarrow 1$ transition.[23] With our IR having a bandwidth of $45\,\mathrm{cm}^{-1}$ this suggests that excited state absorption is not significant. Overall, this means that with the pump laser on we observe a reduction of probe SFG signal intensity simply proportional to the square of the difference in excited and ground state populations $(N_0 - N_1)^2$ as illustrated in figure 2.7. However, this reduction in probe SFG signal depends on the pump-probe delay: For τ much shorter than the overall population relaxation time, the signal reduction is around 15% in our experiment when using collinear polarized pump and probe. At very long delays between pump and probe the reduction almost completely recovers. We do not observe a complete recovery on the time scale used in the experiment due to transient heating described by a population decay of $v = 1$ into an intermediate state where the stretch modes have returned to their ground state, but the hydrogen bonds have weakened leading to a shift in the bOH spectrum.[24] Until now, we have disregarded the fact that water molecules can reorient, in- and out-of the optical plane.

2.3.1 Orientational dynamics

The reorientation of water molecules at an interface is modeled by rotation around the two axes that the two OH groups form. Using the coordinate system in figure 2.8, where the z-axis is normal to the interface, these two rotations are called "in-plane" and "out-of-plane" reorientation. In the former case, the azimuthal angle ϕ changes while the angle θ persists and therefore the OH group that is pointing up remains in the optical plane. In the latter case, the azimuthal angle stays constant

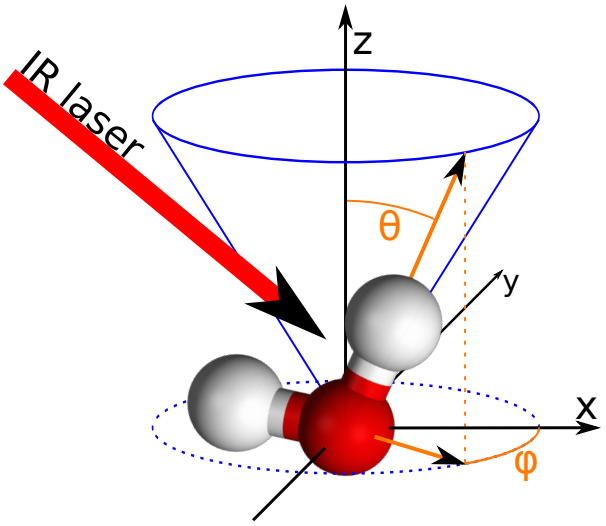

Figure 2.8: A water molecule at the interface excited by an IR laser beam resonant with the dangling OH stretch mode. The z-axis is normal to the interface; x- and y-axes are in the surface plane.

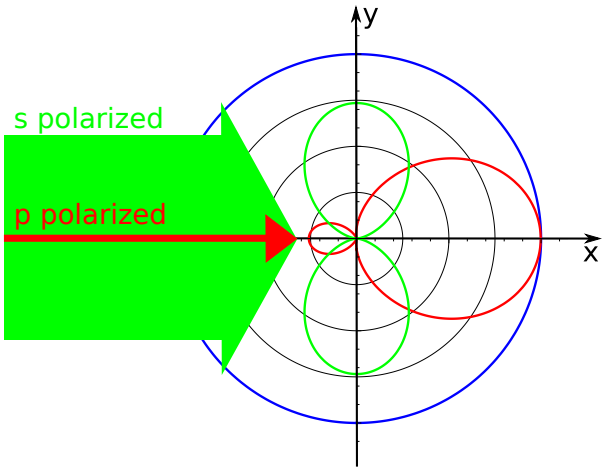

Figure 2.9: Illustration of the azimuthal distribution of the excited dOH groups assuming a dOH tilt angle $\theta_0 = 59°$ [3]. Green indicates the probability distribution of excited dOH produced by an s-polarized pump; red indicates the probability distribution created by a p-polarized pump.

while the polar angle θ changes because the OH group that is pointing upwards rotates out of the optical plane.

2.3.1.1 In-plane orientational dynamics

Reorientation in the optical plane can be thought of in terms of a wobbling motion of the dOH around the z-axis, along the cone shown in figure 2.8. This motion leads to the restoration of the azimuthal isotropy of excited dOH groups (illustrated in figure 2.10). It is of importance to note that in-plane reorientation does not contribute to population decay. To illustrate the effect of population decay, figure 2.11 represents a model scenario in which population relaxation is permitted but that does not allow for in-plane reorientation. In this case, the projection of the angular distribution of the vibrational excited-state distribution onto the z-axis diminishes with the declining population. In reality, the effects of population decay and in-plane orientational dynamics occur at the same time.

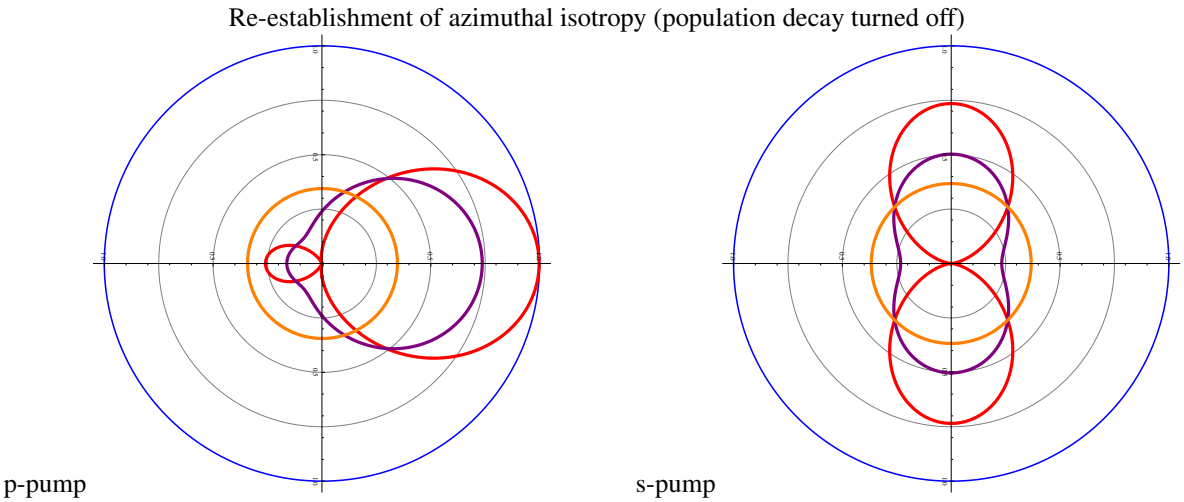

Figure 2.10: Time evolution of the excited-state angular distribution shown in figure 2.9 created by the p-polarized pump pulse (left) and the s-polarized pump pulse (right). To highlight how in-plane reorientational effects contribute to anisotropy decay, population decay is turned off: The pump-induced azimuthal anisotropy decays and azimuthal isotropy is re-established. Color key: Red $t = 0$, purple $t = 0.25T$, orange $t = T$, where T is the decay time associated with in-plane reorientation.

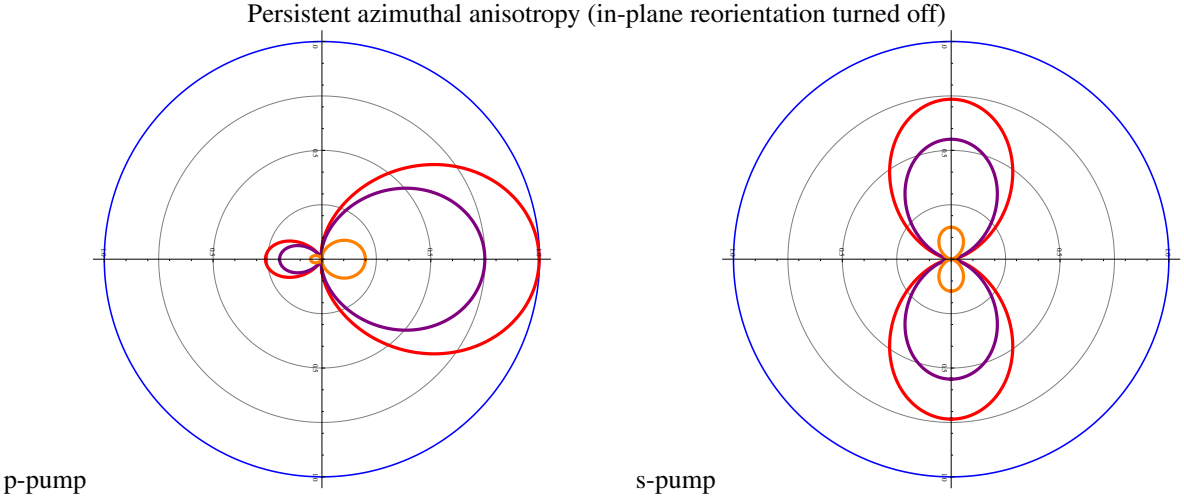

Figure 2.11: Time evolution of the excited-state angular distribution shown in figure 2.9 created by the p-polarized pump pulse (left) and the s-polarized pump pulse (right). To highlight how population decay affects the excited-state angular distribution, in-plane reorientation is turned off: The pump-induced anisotropy persists in this case. Color key: Red $t = 0$, purple $t = 0.25T$, orange $t = T$, where T is the governing population decay time.

2.3.1.2 Out-of-plane orientational dynamics

Out-of-plane reorientation describes the movement where the dOH flips to an orientation that is tangential to the interface and now participates in a hydrogen bond (forward jump), and the corresponding backwards motion (backward jump). Assuming the pump is p-polarized, an excited dOH population with an azimuthal distribution as seen in red in figure 2.9 would be created. The projection of the z-component of the orientational distribution of the population difference of excited- and ground-state dOH groups onto the z-axis can be measured by the probe after a time τ. Within our experiment we follow the development of this projection as a function of the pump-probe delay.

On the other hand, if the pump is s-polarized, the excited dOH population starts out with an azimuthal distribution as shown in green in figure 2.9. The same processes as in the case for p-polarized pump take place, with the difference that the initial population of excited dOH groups that can be probed by the p-polarized probe is smaller. Only the excited dOH groups that are associated with the area where the pumped and probed azimuthal distributions in figure 2.9 overlap contribute to the change in $\chi^{(2)}_{zzz}$.

A hand-waving argument can be made here that the average bleach in the p-pump and s-pump case would essentially only be affected by population decay since the orientational dynamics average out (the reorientation of dOH excited by a p-polarized pump out of the angular distribution seen by the probe is compensated by the reorientation of dOH excited by an s-polarized pump into the angular distribution seen by the probe), whereas the difference of the p-pump and s-pump case is sensitive to orientational dynamics and population decay. These arguments are also supported by calculating the average and difference of the angular distributions and follow their time dependence. (Shown in figures 2.12 and 2.13) It turns out that there are many more processes at work besides reorientation and population relaxation of the dOH groups that dissipate the energy of the stretch vibration and so the validity of the hand-waving argument might not hold. These processes are discussed in section 2.4.

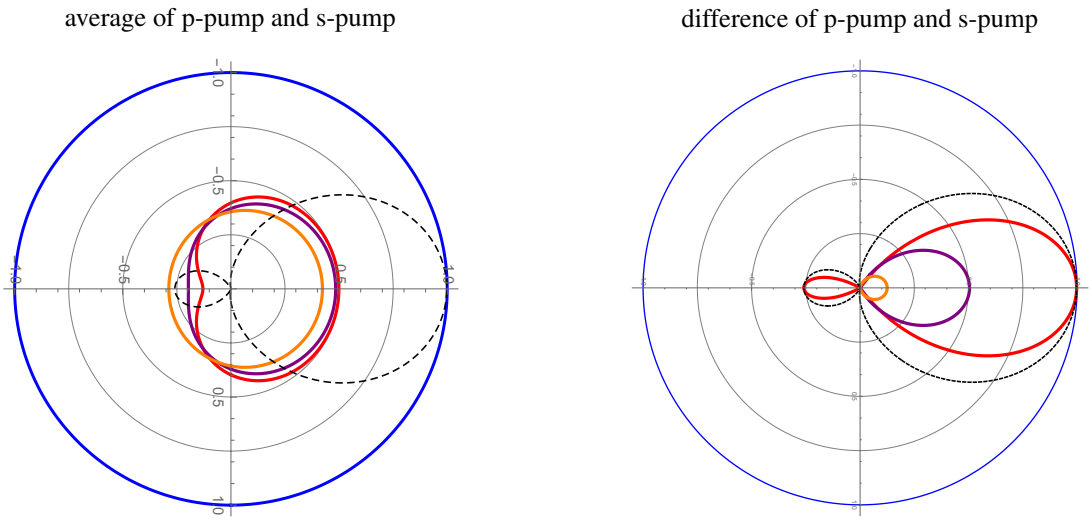

Figure 2.12: The average and difference of p- and s-pump are calculated for the case that population decay is turned off. The results reveal that probing the distribution with a p-polarized probe (shown in black) leads to a large sensitivity to azimuthal anisotropy in the difference of p- and s-pump. The average of the two quantities shows little sensitivity. Color key: Red $t = 0$, purple $t = 0.25T$, orange $t = T$, where T is the decay time associated with in-plane reorientation.

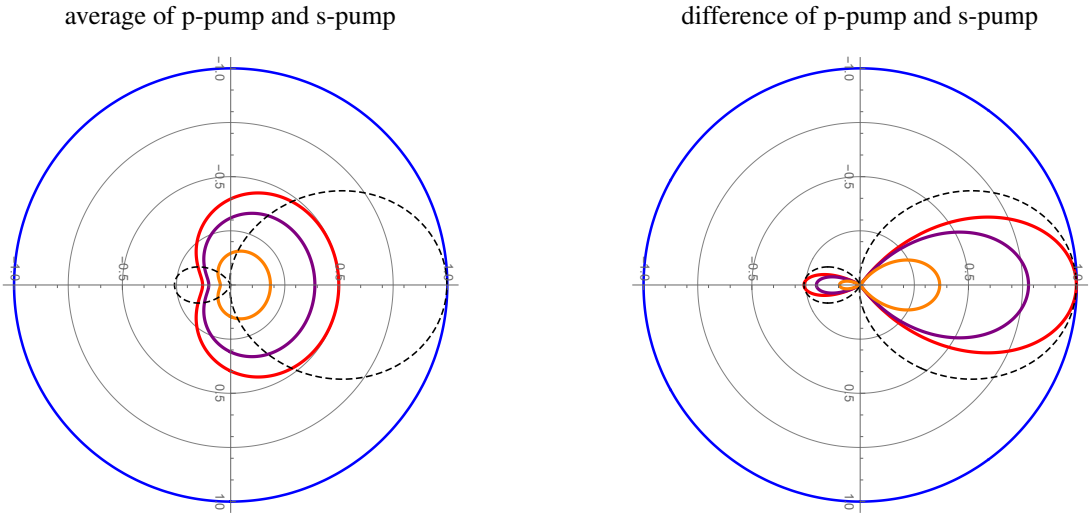

Figure 2.13: The average and difference of p- and s-pump are calculated for the case that no reorientation is allowed. The results reveal that probing the distribution with a p-polarized probe (shown in black) leads to a large sensitivity to population decay in both quantities. Color key: Red $t = 0$, purple $t = 0.25T$, orange $t = T$, where T is the decay time associated with in-plane reorientation.

2.3.1.3 Mathematical description of orientational dynamics

Introducing a pump pulse requires the second order susceptibility to have an additional term that describes the interaction of the pump with the sample (pump-induced bleach) and its evolution until the probe beam interaction. The following equation 2.66 can be understood with the help of the Bloch sphere. The probe SFG intensity $I_{\text{pump on}}$ after the pump interaction is proportional to the square of the difference between ground state N_0 and first excited state N_1 population. Normalized to the pre-pump intensity ($I_{\text{pump off}} \propto \left|\chi^{(2)}_{\text{pump off}}\right|^2 \propto 1$), we get $I_{\text{pump on}} \propto (N_0 - N_1)^2$. On the Bloch sphere, $N_0 - N_1$ is the projection of the Bloch vector onto the z-axis and can be described with the tipping angle θ: $N_0 - N_1 = \cos\theta$. Therefore, $I_{\text{pump on}} \propto \left|\chi^{(2)}_{\text{pump on}}\right|^2 \propto \cos^2\theta =$ or $\chi^{(2)}_{\text{pump on}} \propto \cos\theta$. For a sparsely populated excited state ($N_0 \gg N_1$), the small-angle approximation ($\cos\theta \approx 1 - \theta^2/2$) can be applied so that $\chi^{(2)}_{\text{pump on}} \propto 1 - \theta^2/2$. The tipping angle θ is related to the electric field of the pump and its pulse duration ($\theta \propto |\mathbf{E}_{\text{pu}}| T_{\text{pu}}$), so we arrive at $\chi^{(2)}_{\text{pump on}} \propto 1 - |\mathbf{E}_{\text{pu}}|^2 T_{\text{pu}}^2/2$. It is now possible to recognize and interpret the terms in a mathematically more rigorous description of the second-order probe susceptibility:

$$\chi^{(2)}_{\text{pump on},ijk}(\omega_{IR},t) = \left\langle (\hat{\boldsymbol{i}} \cdot \overleftrightarrow{\alpha}(\Omega) \cdot \hat{\boldsymbol{j}})(\boldsymbol{\mu}(\Omega,\omega_{IR}) \cdot \hat{\boldsymbol{k}}) \right\rangle_{\Omega_t} \tag{2.65}$$

$$+ \left\langle (\hat{\boldsymbol{i}} \cdot \overleftrightarrow{\alpha}(\Omega_t) \cdot \hat{\boldsymbol{j}})(\boldsymbol{\mu}(\Omega_t) \cdot \hat{\boldsymbol{k}}) G(\Omega_t,\Omega_0) \left|\boldsymbol{\mu}(\Omega_0) \cdot \hat{\boldsymbol{l}}\right|^2 \right\rangle_{\Omega_t,\Omega_0} \frac{\left|\mathbf{E}_{\text{pu}}\right|^2 T_{\text{pu}}^2}{\hbar^2}$$

$$= \chi^{(2)}_{\text{pump off},ijk}(\omega_{IR}) - R^{(4)}_{ijkll}(\omega_{IR},t) \left|E_{\text{pu},l}\right|^2 \tag{2.66}$$

where $R^{(4)}_{ijkll}(\omega_{IR},t)$ is the fourth-order temporal response function, $\mathbf{E}_{\text{pu}}$ is the electric field of the pump and T_{pu} its temporal length, $\boldsymbol{\mu}(\Omega_t,\omega_{\text{IR}})$ is the IR dipole derivative, $\overleftrightarrow{\alpha}$ is the Raman polarizability tensor, $\Omega(t) = (\theta(t),\phi(t))$ is the molecular orientation at time t, and $G(\Omega_t,\Omega_0)$ is the Green's function describing the temporal evolution of the molecular orientation between times 0 and t. The angled brackets $\langle\rangle_{\Omega_i}$ indicate averages over each Ω_i.

Gengeliczki et al. [25] showed how the Green's function can be written using spherical harmonics

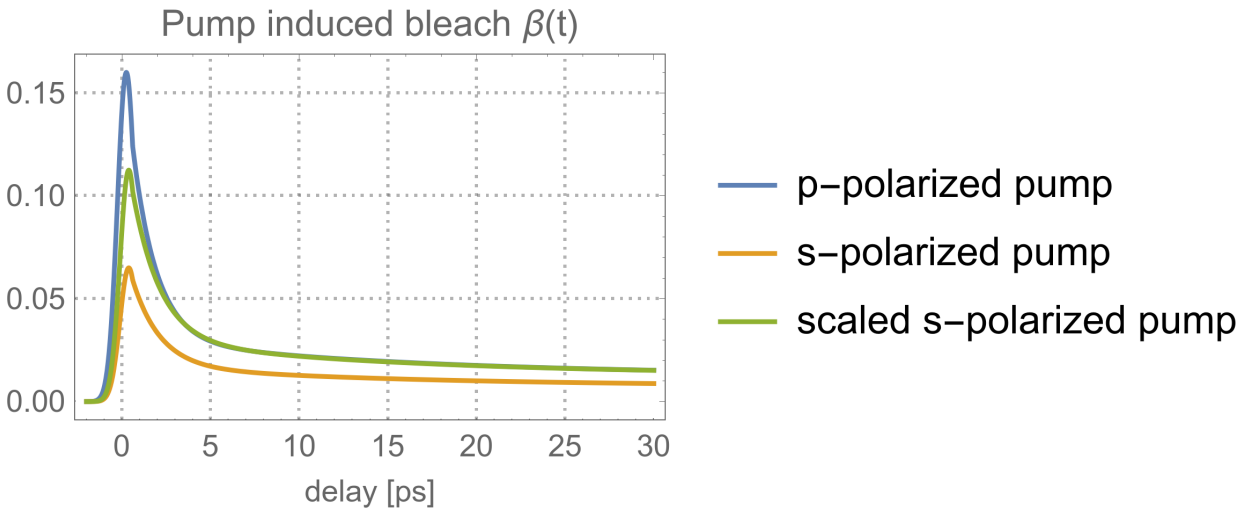

Figure 2.14: Schematic illustration of the pump induced bleach for p-polarized pump $\left(\beta_p(t)\right)$, s-polarized pump $(\beta_s(t))$, and scaled s-polarized pump.

and the rotational diffusion constant D_{or}

$$G(\Omega_t,\Omega_0)=\sum_{n=0}^{\infty}\sum_{m=-n}^{n}Y_n^m(\Omega_t)Y_n^{m^*}(\Omega_0)\exp\left(-n(n+1)D_{or}t\right) \tag{2.67}$$

In our experiment the pump is either s- or p-polarized. Hence, after taking into account the properties of the spherical harmonics, the $C_{\infty,v}$ symmetry of the water interface, and assuming no population relaxation and free diffusion of the dOH within a cone of half angle θ_0, the response function can be written as:

p-pump: $R_{zzzzz}(t)\approx A_{zz}(\theta_0)+B_{zz}(\theta_0)\exp(-k_{or}t)$

s-pump: $R_{zzzyy}(t)\approx A_{yy}(\theta_0)+B_{yy}(\theta_0)\exp(-k_{or}t)$

The reason for considering only the zzzzz and zzzyy contributions is motivated by the discussion of the Fresnel coefficients in the vicinity of TIR in section 2.2.6.3. To experimentally access the rate of molecular reorientation k_{or} with the two available pump-polarizations, we construct the following expression, which is proportional to $\exp(-k_{\mathrm{or}}t)$:

$$R_{zzzzz}(t)-\frac{R_{zzzzz}(t\gg T_{\mathrm{or}}^{-1})}{R_{zzzyy}(t\gg T_{\mathrm{or}}^{-1})}R_{zzzyy}(t)=\left(B_{zz}(\theta_0)-\frac{A_{zz}(\theta_0)}{A_{yy}(\theta_0)}B_{yy}(\theta_0)\right)\exp(-k_{\mathrm{or}}t) \tag{2.68}$$

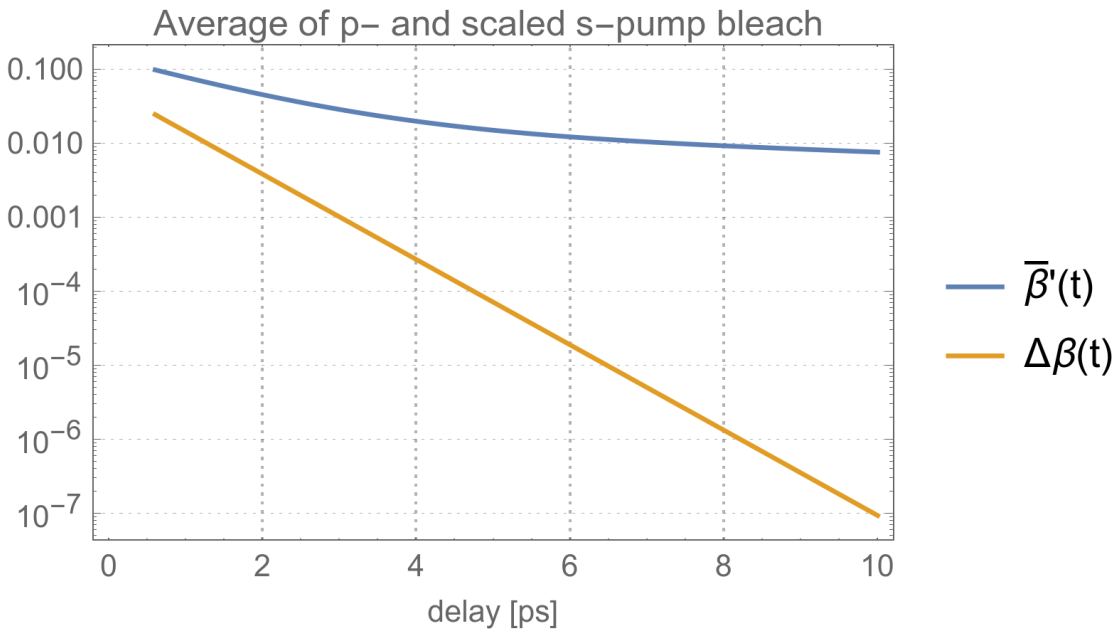

Figure 2.15: Schematic plot of the difference and average of β_p and β_s for time constants observed in the experiment.

It is important to note for later that the coefficients before $B_{zz}(\theta_0)$ and $B_{yy}(\theta_0)$ have opposite signs. In our experiment, we measure the pump-induced bleach $\beta(t)$, depicted in figure 2.14, versus the pump-probe delay t. We do this by measuring the SFG intensity at a given delay with the pump on, $I_{\mathrm{SFG}}^{\mathrm{on}}(t)$, and the pump blocked, $I_{\mathrm{SFG}}^{\mathrm{off}}$, and compute:

$$\beta(t) \equiv 1 - \frac{I_{\mathrm{SFG}}^{\mathrm{on}}}{I_{\mathrm{SFG}}^{\mathrm{off}}} \tag{2.69}$$

Furthermore the bleach of the different pump polarizations s and p is proportional to the correlation function R_{ijkll}:

$$\beta_s(t) \propto R_{zzzyy}(t) \tag{2.70}$$

$$\beta_p(t) \propto R_{zzzzz}(t). \tag{2.71}$$

The orientational dynamics k_{or} can now be obtained when one calculates the difference between β_p and the scaled β_s analogously to equation 2.68 (pictured in figure 2.15):

$$\Delta\beta(t) = \beta_p(t) - \frac{\beta_p(t \gg k_{or}^{-1})}{\beta_s(t \gg k_{or}^{-1})}\beta_s(t) \propto \exp(-k_{or}t) \tag{2.72}$$

Up to this point, the population relaxation time $T_1 = 1/k_{dOH}$ has been neglected, but it can be phenomenologically inserted:

$$\Delta\beta(t) \propto \exp\left(-(k_{or}+k_{dOH})t\right) = \exp\left(-k_{\Delta\beta}t\right) \tag{2.73}$$

An associated quantity that will help to disentangle the orientational dynamics and the population relaxation is the average of β_p and the scaled β_s:

$$\begin{aligned}\bar{\beta}(t) &= \frac{1}{2}\left(\beta_p(t) + \frac{\beta_p(t \gg k_{or}^{-1})}{\beta_s(t \gg k_{or}^{-1})}\beta_s(t)\right) \\ &\propto A_{zz}(\theta_0)\exp\left(-k_{dOH}t\right) + \frac{1}{2}\left(B_{zz}(\theta_0) + \frac{A_{zz}(\theta_0)}{A_{yy}(\theta_0)}B_{yy}(\theta_0)\right)\exp\left(-(k_{or}+k_{dOH})t\right)\end{aligned} \tag{2.74}$$

In equation 2.74, as noted earlier, the opposite signs of B_{zz} and B_{yy} reduces the contribution of the second term, which includes orientational dynamics, in comparison to the first term, which only depends on population decay. To conclude, by measuring $\Delta\beta(t)$ (equation 2.73) and $\bar{\beta}(t)$ (equation 2.74) the two unknowns k_{or} and k_{dOH} can be evaluated.

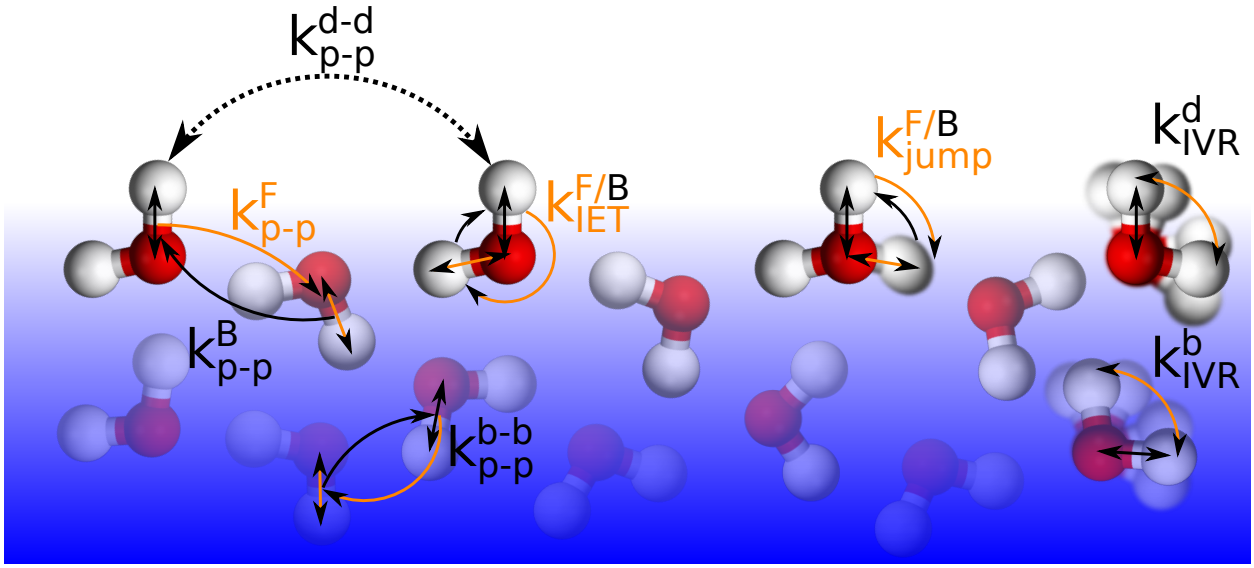

Figure 2.16: Schematic overview of the dangling OH stretch mode decay mechanisms.

2.4 Decay mechanisms of the dangling OH stretch mode

An excited OH stretch mode can decay through several different channels which are schematically shown in figure 2.16. The contributing mechanisms are molecular reorientation, intramolecular vibrational relaxation (IVR), intramolecular energy transfer (IET) and dipole-dipole interactions (p-p). Isotopic dilution of H_2O with D_2O can help suppress some of these mechanisms and may help disentangle their interplay with orientational dynamics. A brief discussion of isotopic dilution follows in section 2.5.

2.4.1 Molecular reorientation - $k_{jump}^{F/B}$

Molecular reorientation is the mechanism of interest in this dissertation. A water molecule at the surface with a dOH sticking out of the bulk water is typically still involved in three other hydrogen bonds: One is formed between the OH group that is oriented tangentially to the surface and lone pair electrons associated with an oxygen atom of another water molecule. The other two hydrogen bonds form between the lone electron pairs of the oxygen and hydrogen atoms of two different, neighboring water molecules. The molecular roerientation happens as a $\sim 90^\circ$ rotation around the bOH axis of the molecule so that the dOH that was sticking out of the bulk is now tangential to the interface and able to form a hydrogen bond with other water molecules. The rate constant for this "forward" reorientation process is denoted k_{jump}^{F}. The generally slower reverse, or "backwards", process is denoted k_{jump}^{B}. The backwards process is slower because there are many more tangentially oriented OH groups at the surface than dangling OH groups. Since detailed balance must hold at equilibrium, the rate of forward jumps must exceed that of backward jumps. MD simulations by our collaborators suggest that $k_{jump}^{F} = (1.6\,\text{ps})^{-1}$ and $k_{jump}^{B} = (21\,\text{ps})^{-1}$ at the interface between water and an idealized hydrophobic surface.[10] Therefore,

$$k_{jump}^{B} = R \times k_{jump}^{F} \tag{2.75}$$

where $R \approx 1/13$. However, at the water/air interface simulations by Vila Verde et al. and experiments by Hsieh et al. indicate that $k_{jump}^{F} = (0.8 - 1.1\,\text{ps})^{-1}$ and $k_{jump}^{B} = (1.9\,\text{ps})^{-1}$ - significantly faster

compared to the water/OTS interface.[17, 16] Using the numbers reported in the paper of Hsieh et al.[17] yields $R \approx 1/1.7$.

2.4.2 Intramolecular vibrational relaxation - $k_{IVR}^{d/b}$

IVR occurs when an excited OH stretch vibration $\nu = 1$ couples to the $\nu = 2$ overtone of the molecular bending mode at $\approx 3150\,\mathrm{cm}^{-1}$.[26]. This process occurs in the bulk with the rate k_{IVR}^{b} where the initial OH stretch vibration involves a bOH group at $3000 - 3500\,\mathrm{cm}^{-1}$. In principle IVR can also occur for a vibrationally excited dOH with the rate k_{IVR}^{d}. Since the dOH stretch vibration mode is about $530\,\mathrm{cm}^{-1}$ to the blue of the $\nu = 2$ bend overtone, the lack of spectral overlap prevents this channel from being a significant decay pathway and $k_{IVR}^{b} \gg k_{IVR}^{d}$. The bulk rate in H_2O has been determined to be $k_{IVR}^{b} = (0.2\,\mathrm{ps})^{-1}$ in several investigations.[26, 27, 28, 29] In the case of isotopic dilution, the intramolecular vibrational relaxation is $\tilde{k}_{IVR}^{b} \approx (0.75\,\mathrm{ps})^{-1}$, where the tilde indicates a quantity associated with isotopic dilution.[30] Since the relaxation from the overtone of the molecular bending mode to its first excited state is very rapid,[26] IVR is for our purposes an irreversible process.

2.4.3 Intramolecular energy transfer - $k_{IET}^{F/B}$

IET describes the transfer of energy with the rate constant k_{IET}^{F} from an excited dOH ($\approx 3680\,\mathrm{cm}^{-1}$) to a bOH ($\approx 3500\,\mathrm{cm}^{-1}$) on the same water molecule.[31] k_{IET}^{F} can be calculated through perturbation theory. The wave function of the excited dOH stretch of an interfacial H_2O molecule can be written

$$|\phi_{dOH}\rangle \propto \frac{\gamma}{\delta}|b\rangle + |d\rangle \tag{2.76}$$

with $|b\rangle$ and $|d\rangle$ being the localized vibrations on the uncoupled bOH and dOH groups, γ being the coupling between bOH and dOH stretch modes, and δ being the frequency difference between the uncoupled modes.

2.4.3.1 Calculation of γ and δ

γ and δ can be derived for H_2O from the work of Stiopkin et al. which focuses on IET in the case of D_2O (and its isotopic dilution with H_2O).[32] There, the coupling between a dOD and a bOD on the same D_2O molecule is $\gamma_{D_2O} = -48\,\mathrm{cm}^{-1}$. This is in contrast to the gas-phase value of $-60\,\mathrm{cm}^{-1}$. Similarly, for H_2O with a gas-phase intramolecular coupling of $-50\,\mathrm{cm}^{-1}$ this would lead to a value of

$$\gamma = \frac{-50}{-60} \times (-48\,\mathrm{cm}^{-1}) = -40\,\mathrm{cm}^{-1}. \tag{2.77}$$

The detuning δ of the uncoupled modes for H_2O can also be derived from what is known about D_2O: First, the observed frequency difference δ'_{D_2O} between the dOD and the bOD, which includes coupling, is calculated as follows:

$$\delta'_{D_2O} = \omega'_{dOD} - \omega'_{bOD} = 2745\,\mathrm{cm}^{-1} - 2580\,\mathrm{cm}^{-1} = 165\,\mathrm{cm}^{-1}. \tag{2.78}$$

The next step is to calculate the detuning of the uncoupled modes δ_{D_2O} of dOD and bOD, which each experience a blue- and redshift of $17\,\mathrm{cm}^{-1}$, respectively, caused by their coupling:

$$\delta_{D_2O} = \delta'_{D_2O} - 2 \times 17\,\mathrm{cm}^{-1} = 131\,\mathrm{cm}^{-1}. \tag{2.79}$$

It is important to note that the surface bOD peak at $2580\,\mathrm{cm}^{-1}$ does not coincide with the bulk bOD peak at $2480\,\mathrm{cm}^{-1}$ (but is well within the broad bulk bOD feature), which indicates that the average bulk bOD is involved in hydrogen bonds that are stronger than the surface bOD. The bulk bOD and the dOD are spectrally separated by $2745\,\mathrm{cm}^{-1} - 2480\,\mathrm{cm}^{-1} = 265\,\mathrm{cm}^{-1}$. The same should apply for the H_2O case. Therefore, scaling δ_{D_2O} by frequency. Stiopkin et al. use $300\,\mathrm{cm}^{-1}$ for the frequency difference between dOH and the bOH on the same H_2O molecule and $250\,\mathrm{cm}^{-1}$ for the dOD and the bOD on a surface D_2O molecule. This leads to

$$\delta_{H_2O} = \delta_{D_2O} \times \frac{300\,\mathrm{cm}^{-1}}{250\,\mathrm{cm}^{-1}} = 157\,\mathrm{cm}^{-1}, \tag{2.80}$$

and finally results in

$$\left|\frac{\gamma}{\delta}\right| = 0.24. \tag{2.81}$$

2.4.3.2 Calculation of k^F_{IET} and k^B_{IET}

During IET the excited dOH transfers its energy to the uncoupled bOH. Therefore we calculate:

$$|\langle b|\phi_{dOH}\rangle|^2 \propto \left|\frac{\gamma}{\delta}\right|^2 = 0.24^2 \tag{2.82}$$

Since the bOH lifetime is governed by intramolecular vibrational relaxation[30] described in the previous section, k^F_{IET} can be estimated to be:

$$k^F_{IET} \approx 0.24^2 k^b_{IVR} = (13\,\mathrm{ps})^{-1} \tag{2.83}$$

The process of IET described so far is reversible. However the "backwards" process k^B_{IET}, from an excited bOH to a dOH, is not energetically favorable and therefore slower compared to the forward process. Using the Arrhenius equation one can establish the ratio between k^F_{IET}/k^B_{IET}, assuming that the system is in equilibrium with respect to IET and that there is there is no energy barrier.[17] This means that the energy gap between dOH and bOH can be used for the calculation:

$$\frac{k^F_{IET}}{k^B_{IET}} = \exp\left(\frac{\Delta E}{k_B T}\right) = \exp\left(\frac{hc(3680-3500)\mathrm{cm}^{-1}}{k_B T}\right) = 2.42 \tag{2.84}$$

where $T = 293\,\mathrm{K}$ has been used. Hence, using the ratio R_{IET} we can express k^B_{IET} in terms of k^F_{IET}:

$$k^B_{IET} = R_{IET} \times k^F_{IET} = \frac{1}{2.42} \times k^F_{IET} = 0.41 \times k^F_{IET} \tag{2.85}$$

R_{IET} is expected to change with isotopic dilution because the bOD feature is located at $\approx 2500\,\mathrm{cm}^{-1}$.[33] Using equation 2.84 leads to $\tilde{R}_{IET} = 0.003$.

2.4.4 Dipole-dipole interactions - k^{i-j}_{p-p}

At the interface, dipole-dipole interactions can couple an excited dOH stretch vibration with dOHs or bOHs of other molecules. The interaction with another dOH is described by the rate constant k^{d-d}_{p-p}. The coupling with a bOH is described by $k^{d\to b}_{p-p}$ or k^F_{p-p} to indicate a "forward" process and by $k^{b\to d}_{p-p}$ or k^B_{p-p} to describe a "backward" process. Dipole-dipole interactions also couple an excited bOH with a bOH of another molecule with the rate constant k^{b-b}_{p-p}. The rates k^{d-d}_{p-p},

k^F_{p-p}, k^B_{p-p} and k^{b-b}_{p-p} in general differ from each other. Cowan et al. determined $k^{b-b,bulk}_{p-p} = (0.075\,\mathrm{ps})^{-1}$ for bulk H_2O.[29] Since we are only sampling water molecule at the interface, the rate is potentially further decreased by a factor of 1/2 due to the absence of OH groups in half of the solid angle: $k^{b-b}_{p-p} \geq (0.150\,\mathrm{ps})^{-1}$. Upon isotopic dilution, this rate decreases according to Förster's theory:[34, 13]

$$k = \left(\frac{4\pi^{3/2}}{3}[\mathrm{OH}]\right)^2 \frac{r_0^6}{T_1} \propto [\mathrm{OH}]^2 \propto \frac{1}{r^6} \tag{2.86}$$

where [OH] is the number concentration of OH groups, r_0 is the Förster radius, T_1 is the lifetime of the excited state without the Förster process and r is the average distance between OH groups. Isotopic dilution according to the ratio 1:2 H_2O:D_2O lowers the OH concentration [OH] by a factor of $2/3$, resulting in a reduction of the undiluted rate by a factor of $(1/3)^2$: $\tilde{k}^{b-b}_{p-p} = 1/9 \times k^{b-b}_{p-p} \geq (1.35\,\mathrm{ps})^{-1}$. Moreover, non-Condon effects (the strong dependence of the dipole derivative of an OH stretch on its hydrogen-bonding environment) reduce the dOH dipole transition matrix element by a factor of 1/3 relative to that of bOH, so that in combination with the dipole-dipole r^{-6} distance dependence and the small spectral overlap between dOH and bOH stretch excitations, it is possible to neglect k^{d-d}_{p-p}, k^F_{p-p} and k^B_{p-p}.[35, 36, 37] In our experiment, dipole-dipole interactions between bOH groups act as an irreversible process: An initially excited dOH transfers its energy via IET to the bOH of the same molecule, from here following the fastest processes are IVR and the k^{b-b}_{p-p} dipole-dipole interactions. While IVR leads to vibrations red shifted from our detection window, k^{b-b}_{p-p} effectively channels the excited dOH stretch population away from the OH groups at the surface and dissipates the energy into the bulk and can therefore be regarded as irreversible for our purposes.

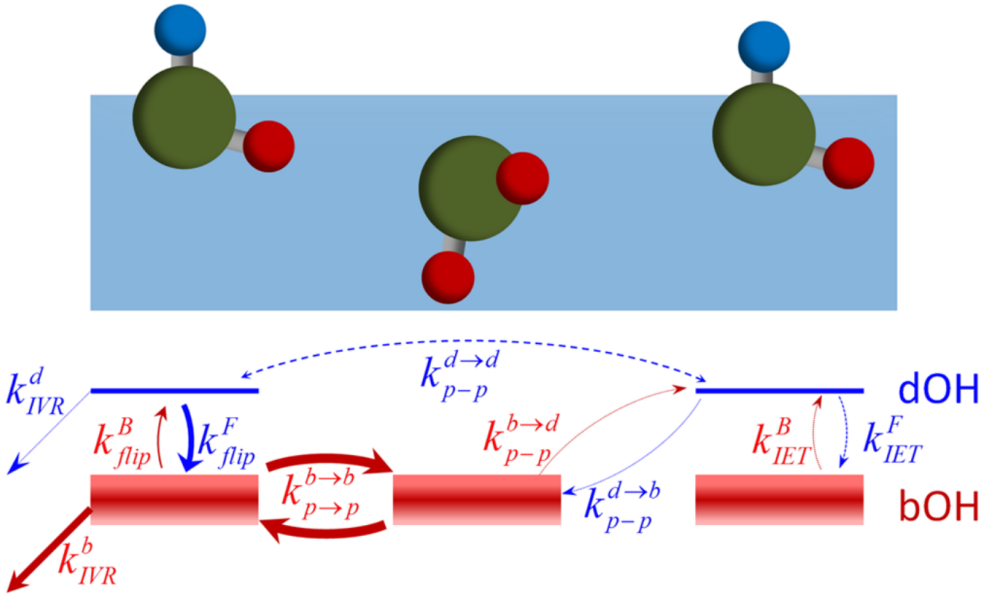

Figure 2.17: Overview from Xiao et al.[4] of the processes involved in the decay of the excited dangling OH stretch vibration.

	H_2O		H_2O:D_2O::1:2	
term	value	source	value	source
k^{b}_{IVR}	$(0.2\,\mathrm{ps})^{-1}$	[27, 28, 29]	$(0.75\,\mathrm{ps})^{-1}$	[30]
k^{b-b}_{p-p}	$\geq (0.15\,\mathrm{ps})^{-1}$	[29]	$\geq (1.6\,\mathrm{ps})^{-1}$	[13]
k^{F}_{IET}	$(13\,\mathrm{ps})^{-1}$	[30, 32]	$\ll (13\,\mathrm{ps})^{-1}$	[30, 32]
R_{IET}	0.37	[17]	0.0025	[17]
R	1/13	[10]	1/13	[10]

Table 2.1: Summary of the rate constants of the dominant processes involved in relaxation of the pump-probe SFG signal.

2.5 Isotopic dilution

Isotopic dilution of H_2O with D_2O can be of great aid in suppressing certain decay mechanisms and better identifying the dominant mechanisms involved in the decay of the pump-probe SFG signal. The introduced D_2O leads through dissociation of H_2O and D_2O and exchange of H and D to the formation of HDO molecules. Sufficiently diluted with D_2O, the heavy water molecules and OD groups effectively isolate the excited dOH spatially and spectrally. The vibrational excitations of OD groups are at a significantly lower frequency than the excitations of the OH groups. If we focus on an HDO molecule with an excited dOH group, the lack of spectral overlap between dOH and bOD will effectively eliminate IET from dOH to bOD. In addition, compared to the case of H_2O the overtone of the bending modes of D_2O and HDO have less overlap with the dOH and bOH stretch vibration, slowing the IVR rate considerably. Reducing the density of OH groups also reduces the dipole-dipole interactions (dOH→dOH, dOH→bOH, bOH→bOH) due to the increased distance between OH groups. The reorientation time is not expected to be affected substantially by isotopic dilution. However, decreasing the H_2O:D_2O ratio decreases the SFG intensity proportionally to N^2_{dOH}, the square of the number density of dOH groups at the interface. We use a molar ratio 1:2 of H_2O:D_2O as a compromise between loss of signal and having the majority of dOH groups associated with HDO molecules.

CHAPTER 3

EXPERIMENTAL SETUP

In order to perform SFG we require an IR source that can be tuned to be resonant with the dOH stretch vibration at $3680\,\mathrm{cm}^{-1}$. Since the SFG signal is relatively weak, there is need for substantial IR power too. Moreover, to resolve the fast processes presented in the previous chapter, it is necessary that those IR pulses are short enough. At the same time, it is of advantage to generate the SF with a narrowband and long VIS pulses to provide the required spectral resolution. This chapter elaborates on the setup of such a system and the signal processing that leads to the data presented in the next chapter.

3.1 Laser source

Our primary laser source is the Spectra Physics Spitfire PRO-XP, which uses a mode-locked Ti:sapphire Mai Tai oscillator as the seed laser and a pulsed green solid state Spectra Physics Empower Nd:YLF laser as the pump laser. The system is designed to produce $\approx 4\,\mathrm{mJ/pulse}$ at

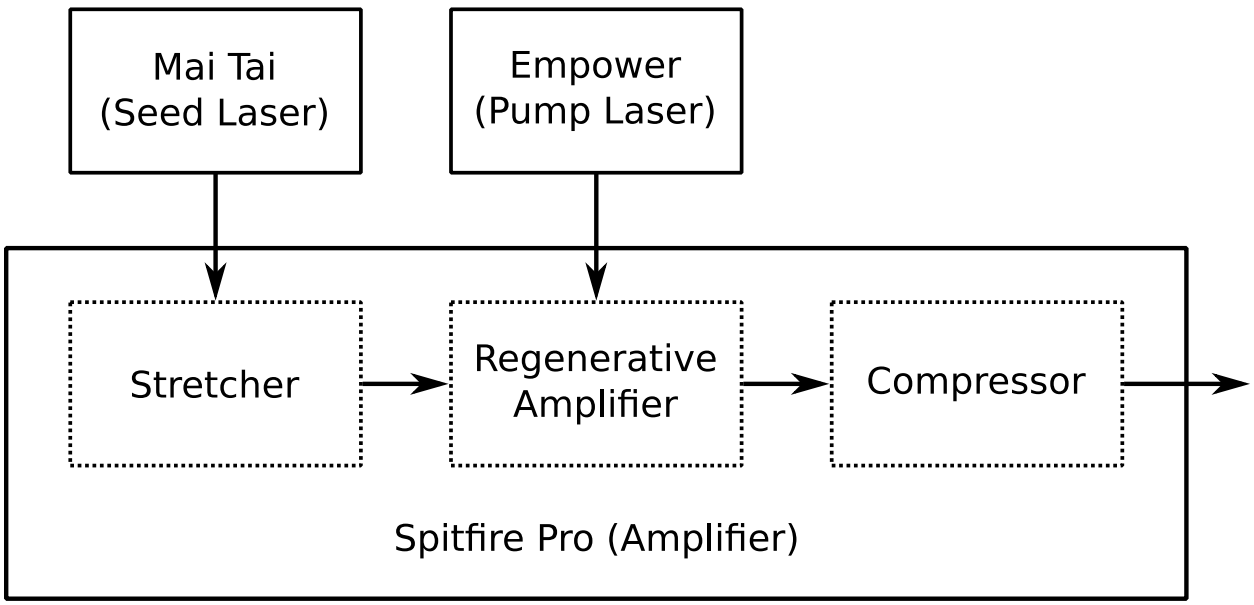

Figure 3.1: Schematic illustration of the Spectra Physics Spitfire PRO-XP system.

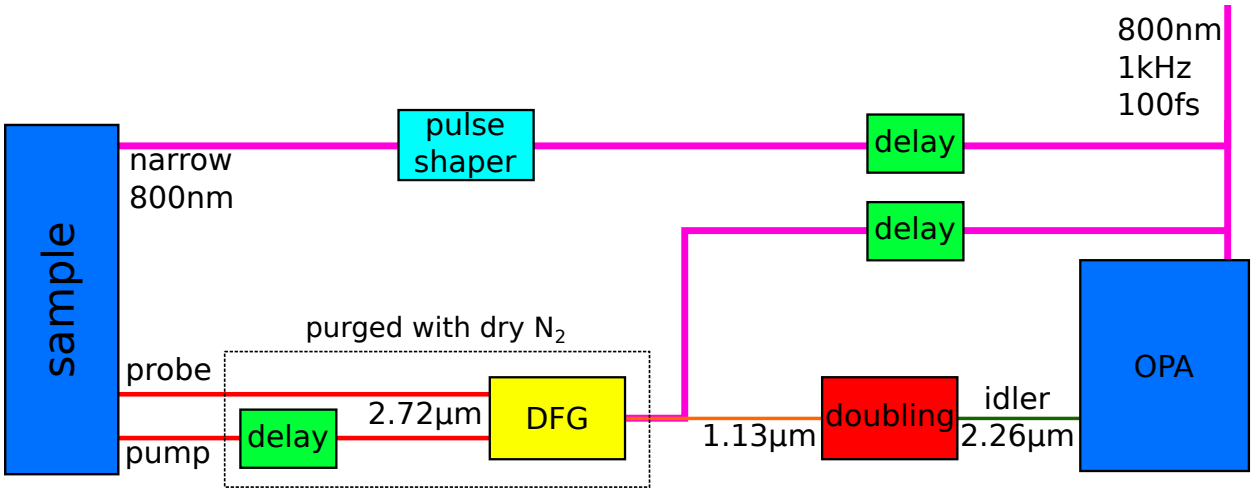

Figure 3.2: Schematic overview of the experimental setup used to investigate the dangling OH.

800 nm with a full-width half-maxiumum bandwidth of 13 nm at a repetition rate of 1 kHz and < 120 fs pulses. About 2 mJ/pulse are used for the water experiments.

3.2 Optical parametric amplifier (OPA)

In order to create infrared beams that are resonant with the dangling and bonded vibrational OH stretch modes there are several stages involved, the first one being an OPA based on the design of Kaindl et al.[38] 1 mJ/pulse is used to power a homemade OPA with two pump stages. A beam splitter (BS) splits the 800 nm beam into the seed and pump beam. The seed 800 nm intensity is regulated with the combination of a thin film polarizer and a $\lambda/2$ waveplate and is then focused by a $f = 75$ mm lens into a 1 mm c-cut sapphire crystal for white light supercontinuum generation. A spherical mirror, with $f = 25$ mm, placed approximately one focal length from the sapphire is used to focus the white light into the nonlinear optical crystal. The 800 nm pump beam is focused with a $f = 500$ mm lens and is split with a beam splitter into pumps for stage 1 and stage 2. The stage 1 pump is sent co-linearly with the white light into a β-BaB_2O_4 crystal ("BBO", 5x6x4mm^3, $\theta = 28°$, $\phi = 0°$, P/P) for type II phase-matching using a dichroic mirror (Side 1: $R \geq 99.0\%$ for $775 - 825$ nm s polarization, $T_{avg} \geq 96\%$ for $950 - 3200$ nm p polarization; side 2: $R \leq 0.5\%$ for $950 - 1600$ nm p polarization). The created signal and idler are retro-reflected at a small non-zero

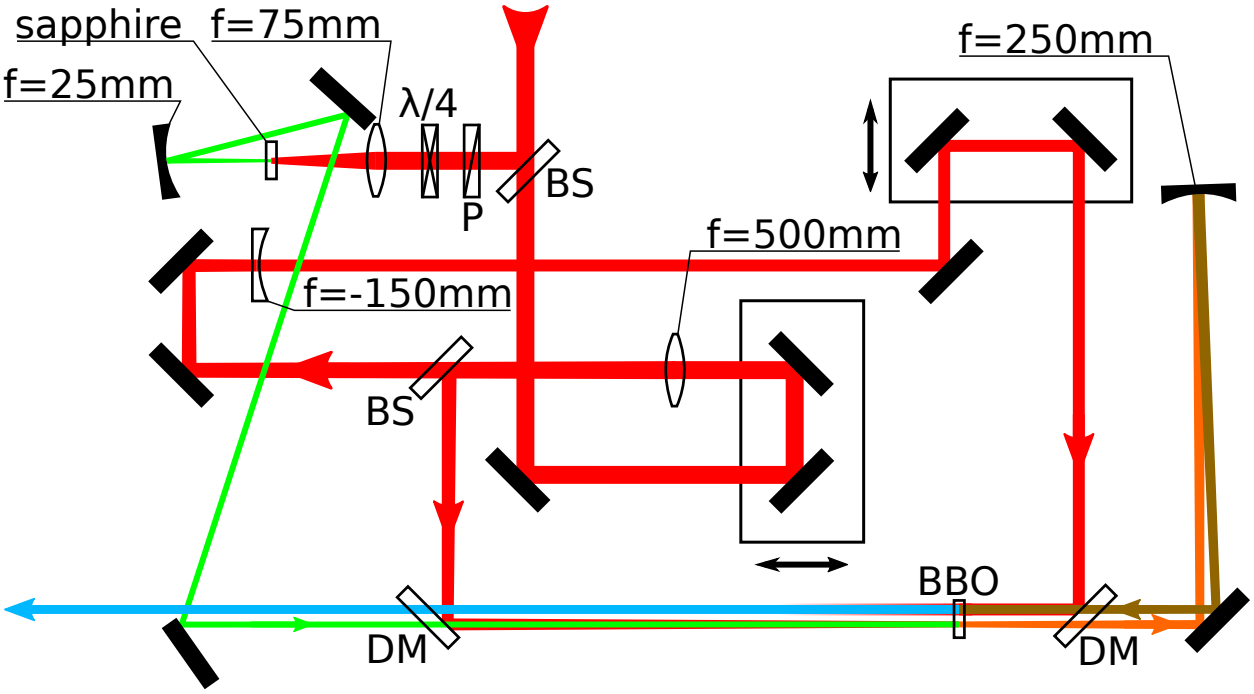

Figure 3.3: Schematic overview of the homemade OPA. The red beam represents the 800nm, the green beam is the supercontinuum white light, the orange beam is the signal and idler after the first pass through the BBO crystal, the brown beam is its reflection from the spherical mirror and the cyan beam is the signal and idler after the second pass through the BBO crystal.

angle into the BBO by a $f = 250\,\text{mm}$ spherical mirror placed about one focal length away from the BBO crystal. The 800 nm for stage 2 is re-collimated by a f$= -150\,$mm lens and then goes through the BBO co-linearly with the retro-reflected signal and idler to pump the second pass.

3.3 IR resonant with the dangling OH stretch vibration

The second stage generates the IR that is resonant with the dangling OH stretch vibration ($3680\,\text{cm}^{-1}$) via difference frequency generation (DFG) between the 800 nm ($12500\,\text{cm}^{-1}$) and the doubled OPA idler ($2 \times 4410\,\text{cm}^{-1} = 8820\,\text{cm}^{-1}$). The OPA idler is doubled with a BBO crystal, its beam diameter expanded by a telescope, and then co-linearly sent through a $KTiOPO_4$ ("KTP", 10x10x6mm^3, $\theta = 42°$) crystal along with the 800 nm beam. Just before the KTP crystal, the 800 nm and doubled idler beam enters a housing through a CaF_2 window. The housing is purged with dry nitrogen gas which allows the generated IR to propagate without getting absorbed by ambient

water vapor. A 2.4 µm longpass filter after the DFG crystal is used to block residual light from the doubled idler and the 800 nm beam. The bandwidth of the IR was measured to be $\approx 45\,\mathrm{cm}^{-1}$ at the full-width half maximum.

3.4 Sum frequency generation with IR pump/probe and VIS 800nm

For SFG, the IR and VIS pulses are overlapped spatially and temporally at the sample. The beam angles in the experiment and shown in figure 3.4 are $\theta_{\mathrm{IR}}^{\mathrm{pump}} = 52.0°$, $\theta_{\mathrm{IR}}^{\mathrm{probe}} = 69.8°$, and $\theta_{\mathrm{VIS}} = 76.5°$. Further details follow in this section.

3.4.1 IR pump and probe beams

After the vibrationally resonant IR is generated, the beam is split into pump and probe beams with a ZnSe window. The reflected beam is the probe and the transmitted beam is the pump, which is sent over a LabView-controlled mechanical delay stage, which determines the delay between pump and

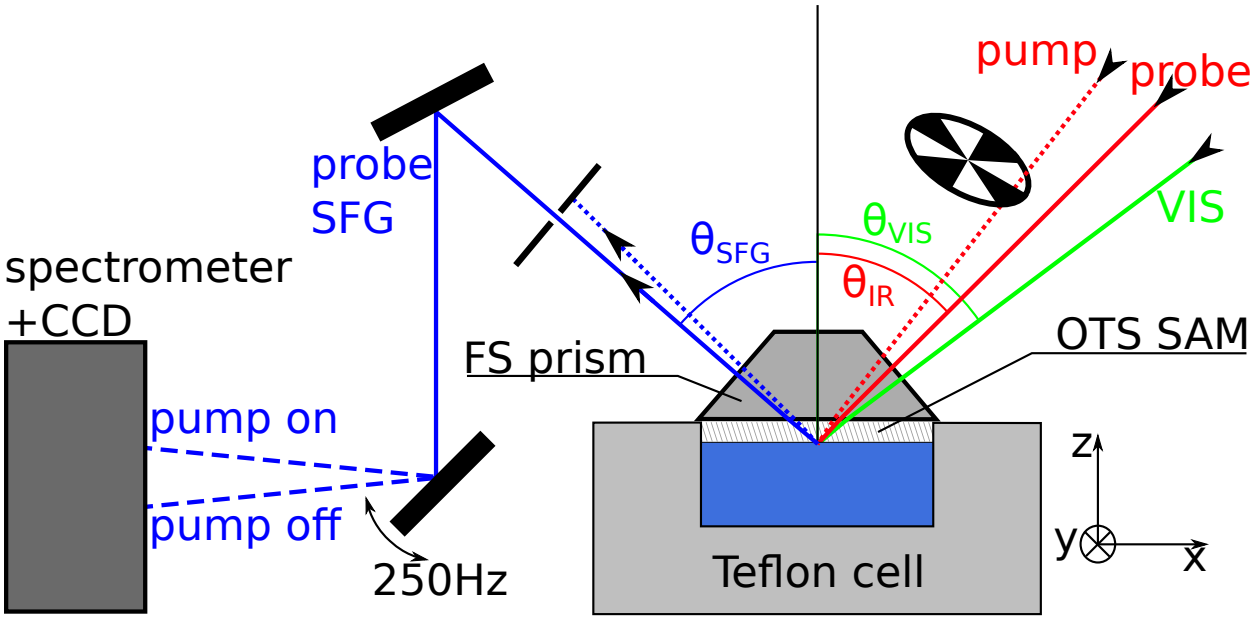

Figure 3.4: Experimental schematic of the beam geometry and sample. The fused FS prism is coated with an OTS SAM. The dotted blue line is the pump SFG (pump+VIS) which is discarded using an iris during the experiment but is of importance for alignment purposes.

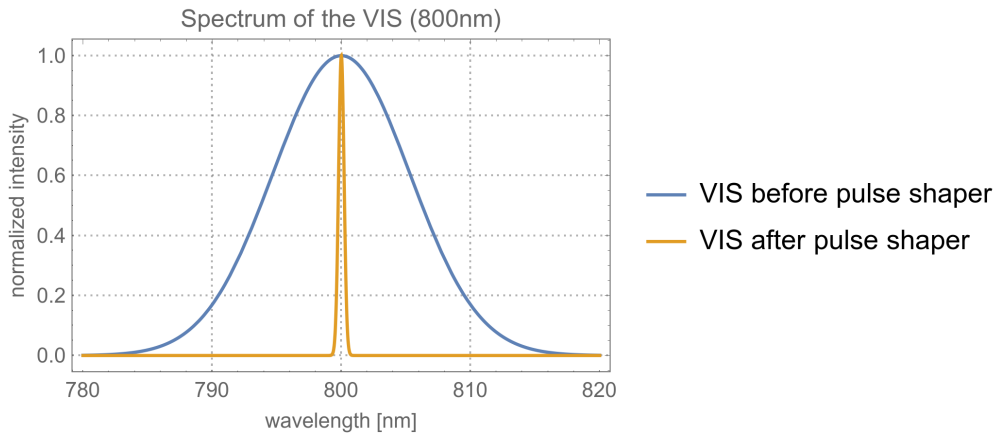

Figure 3.5: Illustration of the spectral narrowing by the pulse shaper.

probe beams during the experiment. On the way to the sample, the polarization of both beams is controlled with $CdGa_2S_4$ $\lambda/2$ (Altechna, anti-reflection coated, zero order, 3000 nm) waveplates. Furthermore, the pump intensity is regulated by using a polarizer in conjunction with the waveplate. When the IR is tuned to the dOH stretch vibration, the IR beams leave the housing purged with dry nitrogen through a 2.4 µm longpass filter about 125 mm before the sample. Pump and probe beams are then focused with CaF lenses, $f = 100$ mm and $f = 80$ mm respectively, onto the sample.

3.4.2 VIS 800nm

For generating the sum-frequency at the sample, we use a 4f pulse shaper to spectrally narrow the 800 nm beam from a full-width half-maxiumum (FWHM) of 12.5 nm to 0.5 nm (8 cm^{-1}) as depicted in figure 3.5. A narrowband 800 nm in combination with a broadband IR has the advantage that there is effectively a one-to-one correspondence between the SFG and IR spectra: $\omega_{IR} = \omega_{SFG} - \omega_{VIS}$. The pulse shaper, displayed in figure 3.6, consists of a grating with 1200 grooves/mm, a $f = 500$ mm spherical mirror and a mirror with an adjustable slit. The spherical mirror is placed one focal length away from the grating to compensate the angular dispersion caused by the grating and to focus the different wavelength components at different lateral positions on the the slit/mirror, which is placed one focal length away from the spherical mirror. Translating the narrowed slit perpendicular to the incoming beams selects for a narrow band. The flat mirror is tilted so that the spectrally narrowed

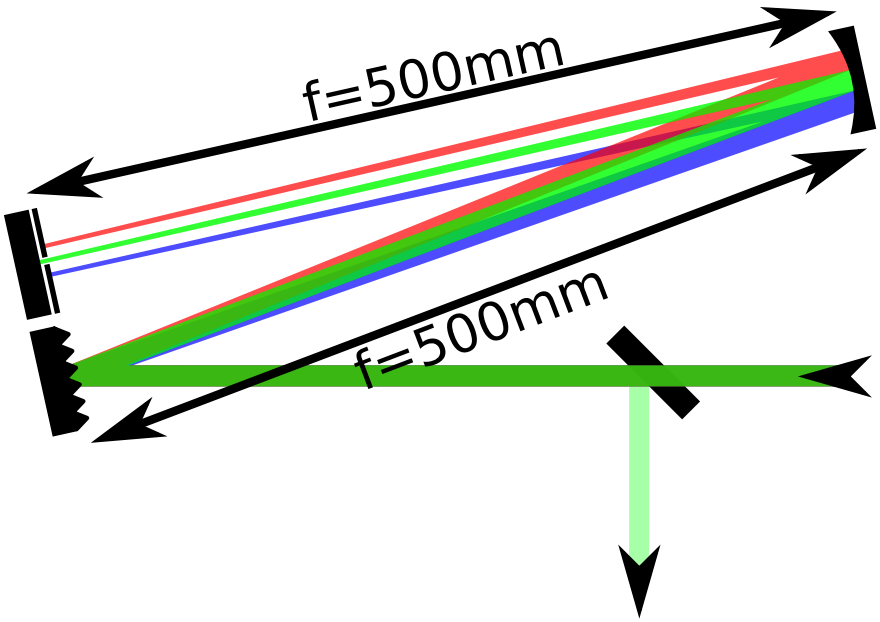

Figure 3.6: Schematic overview of the 4f pulse shaper. To illustrate the pulse shaper's operation, the figure uses three distinct colors (red, green, blue) which would correspond to the red tail, the center and blue tail of the 800 nm spectrum.

beam comes out slightly below the original optical plane and can, therefore, be redirected with a mirror. Next, the spectrally narrowed beam goes through a delay stage, a $\lambda/2$ waveplate, and a thin film polarizer which enables us to control the delay with respect to the pump/probe IR beams, its power, and polarization. Finally, a $f = 500$ mm lens is used to focus the beam onto the sample.

3.5 Signal detection

At the sample, the VIS and both IR beams are overlapped spatially and temporally to create two SFG signals: One from VIS + pump IR and one from VIS + probe IR. The data in this text has been detected in upp configuration (SFG signal unanalyzed, probe and VIS p-polarized).

	slave	master
voltage	23.6V	23.6V
standby current	0.18A	0.21A
operation current	0.31A	0.35A

Table 3.1: Galvanometer power supply (Topward Dual-Tracking DC power supply 63061) settings

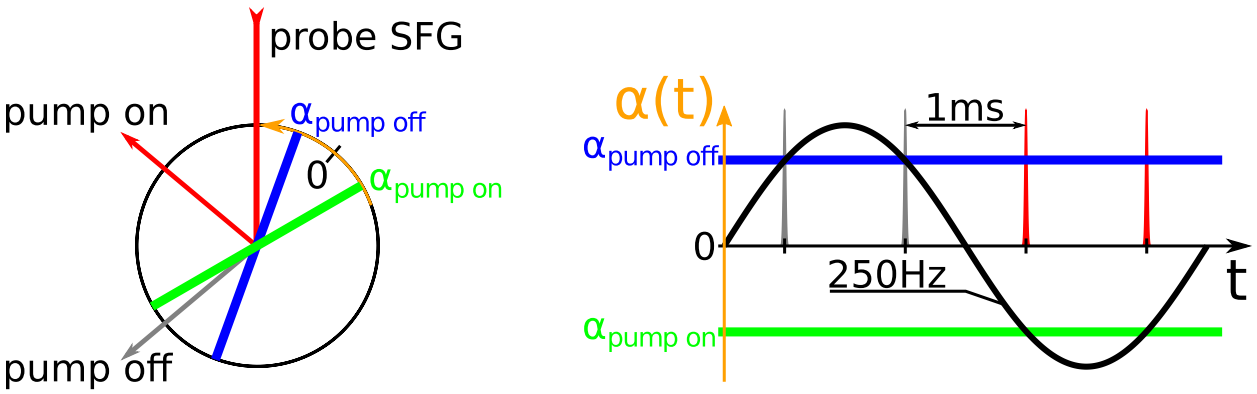

Figure 3.7: Schematic of the galvanometer-driven separation of "pump-on" and "pump-off" beams where $\alpha(t)$ is the galvanometer mirror angle at time t. The gray (red) laser pulses indicate the probe SFG signals corresponding to by the chopper blocked (unblocked) IR pump pulses.

Note: There are other signals from different orders of photon interaction but they are at different wavelengths and propagate into different directions than the beams of interest. Figure 3.4 gives a simple overview of the relevant beams close to the sample. The signals are collimated by a f=100mm lens, placed one focal length away from the sample. Just after the lens, the residual 800 nm VIS and pump SFG beam are blocked by an iris that allows only the probe SFG beam to pass. As described by Ghosh et al.,[39] a galvanometer (Cambridge Technology 6230H) and an optical chopper (Thorlabs), both synchronized with the laser, are used to separate the signal into two beam trajectories: One corresponds to a "pump-off" measurement where the pump is blocked by the chopper wheel so it does not hit the sample. The probe SFG signal in this case serves as a reference measurement. The other one corresponds to the "pump-on" measurement where the pump pulse clears the chopper wheel and excites the sample. More specifically, the chopper and the galvanometer frequency and phase are set so that two consecutive pump laser pulses clear the chopper and the two corresponding probe SFG signals hit the galvanometer when the mirror is at the "pump-on" angle. The next two pump laser pulses are then blocked by the chopper, and their corresponding probe SFG signals hit the galvanometer at the "pump-off" angle. Figure 3.7 provides an illustration of the galvanometric scheme, and table 3.1 shows the galvanometer power supply settings (Topward Dual-Tracking DC Power Supply 6306D) used during the experiment. Finally,

a 150 mm lens is used to focus the beam into the spectrometer slit. To further reduce background light, unwanted wavelengths are blocked by a bandpass filter with a center wavelength of 620 nm and FWHM 60 nm. The signal enters a Princeton Instruments Acton SP 2300 spectrometer with a 1200 lines/mm grating and is collected by a liquid nitrogen cooled, two-dimensional CCD camera from Princeton Instruments (Spec-10:400B/LN). The spectrometer is calibrated with a mercury lamp, in particular by using the yellow-orange line pair at 576.959 nm and 579.065 nm. According to the manufacturer, the spectrometer and camera together have a resolution of $3.46\,\mathrm{cm}^{-1}$ at the sum-frequency (≈ 618 nm). This in combination with the VIS bandwidth of $8\,\mathrm{cm}^{-1}$ yields a resolution for the detected sum-frequency spectra of

$$\sqrt{(3.46\,\mathrm{cm}^{-1})^2 + (8\,\mathrm{cm}^{-1})^2} \approx 9\,\mathrm{cm}^{-1}. \tag{3.1}$$

The y-axis of the chip allows separation of pump-on and pump-off spectra, whereas the x-axis represents the wavelength λ of the detected photons. Before the experiment, we choose a set of pump-probe delays $\{t_1,\ldots,t_N\}$. Then, at a given pump-probe delay $t_k \in \{t_1,\ldots,t_N\}$, the galvanometer creates two vertically separated horizontal regions on the CCD with the intensity $I^{\mathrm{on/off}}(\lambda, y; t_k)$. The CCD exposure ranges typically from a few seconds up to 24 s. Vertical integration of the CCD signal in each of the two regions of interest (ROI) yields the spectra of the pump-off and pump-on signals of the form $I^{\mathrm{on/off}}(\lambda; t_k)$ as illustrated in figure 2.7. At this point, the two spectra are backed up on the computer hard disk drive and the pump-probe delay altered to the next predetermined time. Once one sweep through the set of delays is complete, the next sweep is initialized automatically until the program is stopped after M scans. The labeling of our data is now $I_l^{\mathrm{on/off}}(\lambda; t_k)$, where $l \in \{1,\ldots,M\}$. In some cases, we had to intervene here to correct for distortions by cosmic rays. A detailed description of this procedure can be found in section 3.5.1. The spectra corresponding to the same delays are then averaged across the sweeps:

$$\bar{I}^{\mathrm{on/off}}(\lambda; t_k) = \frac{1}{M} \sum_{l=1}^{M} I_l^{\mathrm{on/off}}(\lambda; t_k) \tag{3.2}$$

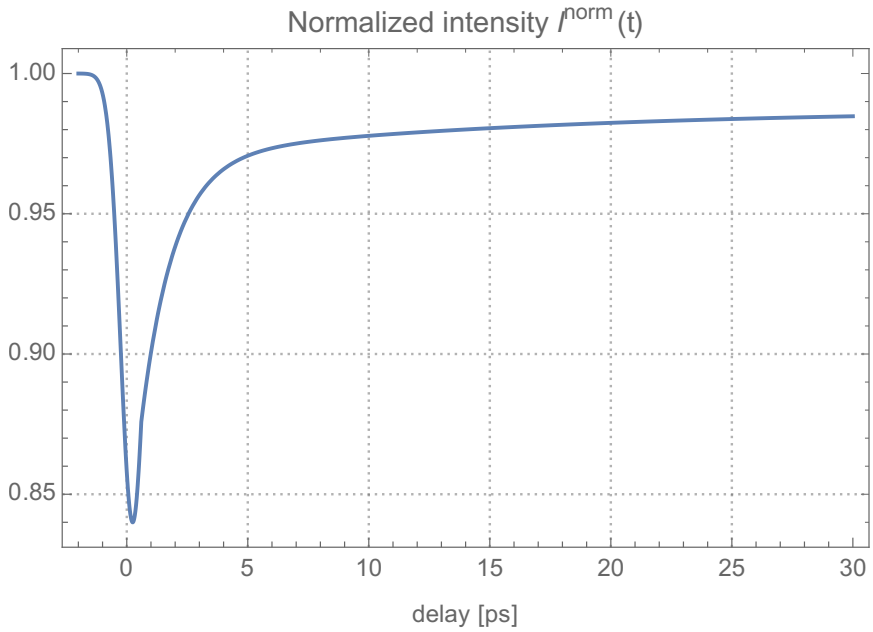

Figure 3.8: Schematic illustration of a typical normalized intensity trace $I^{\mathrm{norm}}(t_k)$.

The next signal processing step is to integrate those spectra over a chosen range of wavelengths to count the total number of detected photons for the pump-on and pump-off signals:

$$I^{\mathrm{on/off}}(t_k) = \sum_{\lambda=\lambda_1}^{\lambda_2} \bar{I}^{\mathrm{on/off}}(\lambda; t_k) \tag{3.3}$$

This process yields the two scalars: $I^{\mathrm{on}}(t_k)$ and $I^{\mathrm{off}}(t_k)$. To display the dynamics of the system a common way to plot the data (as seen in figure 3.8) is to compute the on/off ratio

$$I^{\mathrm{norm}}(t_k) = \frac{I^{\mathrm{on}}(t_k)}{I^{\mathrm{off}}(t_k)} \tag{3.4}$$

versus the pump-probe delay t_k. A homemade LabView program is used to coordinate data collection, the control of the delay stage and the calculation of $I^{\mathrm{norm}}(t_k)$. Probing the sample before the pump interaction at time $t = 0$, yields $I^{\mathrm{norm}}(t < 0) \approx 1$. During and after the pump interaction, a dip in $I^{\mathrm{norm}}(t \approx 0) < 0$ indicates bleaching, which recovers at long delays. For further investigation, the bleach is calculated (figure 3.9):

$$\beta(t_k) \equiv 1 - I^{\mathrm{norm}}(t_k) \tag{3.5}$$

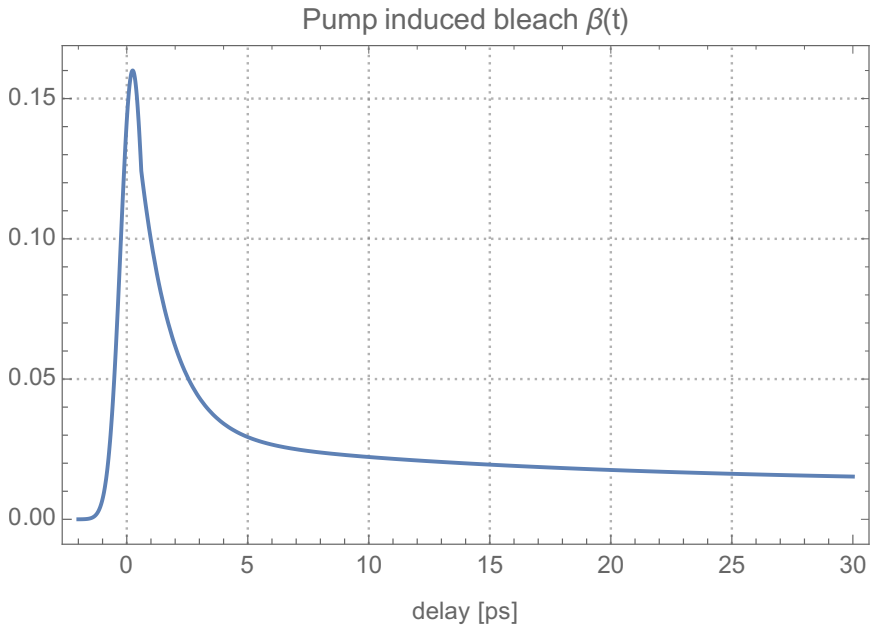

Figure 3.9: Schematic illustration of a typical trace of the pump-induced bleach.

3.5.1 Cosmic ray removal

The CCD chip is sensitive to cosmic rays which result in spikes in the collected spectra. To achieve the best possible signal-to-noise ratio the data is scanned by a Matlab script which removes the cosmic ray spike. An algorithm determines if the derivative of the spectra $\frac{\Delta I}{\Delta \lambda}$ exceeds a predetermined value. If such an abnormality is found, for example in the spectrum corresponding to scan l at delay t_k, it is replaced by the average of the preceding and succeeding scan as illustrated in figure 3.10:

$$I_l(\lambda;t_k) = \frac{I_{l-1}(\lambda;t_k) + I_{l+1}(\lambda;t_k)}{2}. \tag{3.6}$$

The basis for the algorithm is the assumption that it is unlikely that cosmic rays interact with the same detector chip pixel column (which determine the wavelength) during consecutive scans. This procedure is performed for pump-on and pump-off spectra.

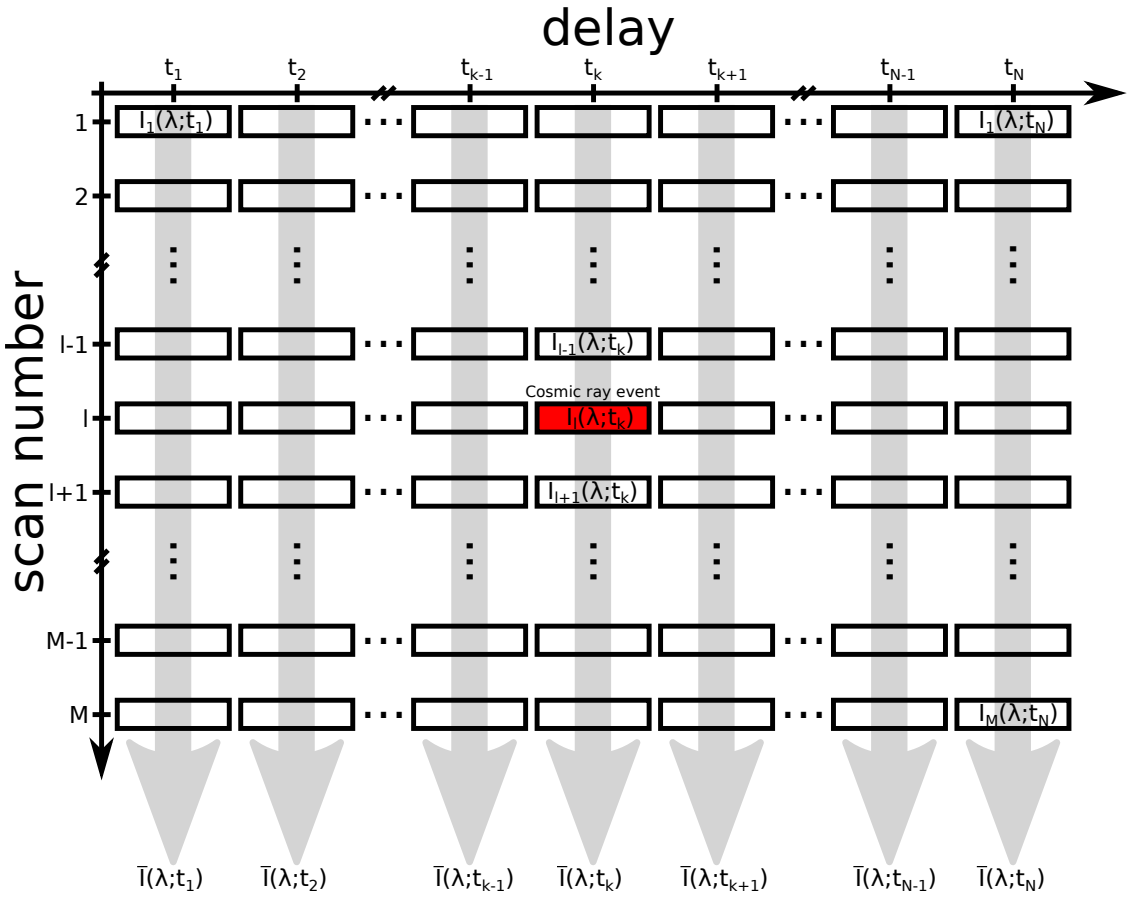

Figure 3.10: Schematic of the data collection and cosmic ray removal process. Each box represents a spectrum collected during scan number l at pump-probe delay t_k.

3.6 General procedure

After overlapping the IR and VIS beams with a pinhole, a BBO crystal is put in place to roughly find the temporal overlap of the beams by maximizing the intensity of the VIS+probe and VIS+pump SFG signals by monitoring the intensity on a white business card by eye while manually moving the delay stages. Usually, after the temporal overlap has been found, small adjustments of the IR beam mirrors are made to increase the spatial overlap. Next, an Ag mirror is positioned at the location of the overlap. The mirror is used to further fine tune both the spatial and temporal overlap by monitoring the pump and probe SFG signals through the monochromator. At this point, it is advisable to confirm that the SFG signal occurs at the intended wavelength ($\omega_{SFG} = \omega_{IR} + \omega_{VIS}$). To accomplish this, an accurate measurement of the VIS spectrum ω_{VIS} has to be performed. Only

then can one proceed with calculating the IR spectrum with confidence. Since the VIS is spectrally very narrow it is sufficient to use the peak frequency ω^*_{VIS} of its spectrum for the calculation. Furthermore, the IR range that we are interested in is far away from any resonances of Ag.[40] This means the SFG signal from the Ag mirror can be directly converted ($\omega_{IR} = \omega_{SFG} - \omega^*_{VIS}$) into the spectrum of the IR as plotted in figure 4.1. Should the IR not be in the desired spectral range, adjustments upstream are necessary. Otherwise one can put the sample in place. Next, it is usually only a matter of translating the sample, while making sure that the reflected VIS beam travels to the monochromator. In our case, the VIS is an appropriate guide because the SFG signal will be close enough to the VIS beam due to the collection lens placed one focal length from the sample. One should be able to see the SFG signal from the water-OTS interface on the CCD after patiently translating the sample in the optical plane. However, after having found the SFG signal, further tweaking of spatial and temporal overlap is usually needed as well as adjustment of the focal points of the IR beams because of refraction of the beams upon entering the fused silica prism. Since the Rayleigh length of the VIS beam is larger than those of the IR beams, the VIS beam lens rarely needs adjustment at this point. In contrast, the SFG signal is more sensitive to the IR lens position. Translating the pump and probe lenses parallel to the beams by only a few millimeters can increase the SFG signal significantly if the IR beams were not focused properly at the sample. After maximizing the pump and probe SFG signals, the third-order signal originating from the mixing of VIS, IR probe, and IR pump is maximized to ensure that not only VIS + probe and VIS + pump are individually overlapped but that all three beams are optimally overlapped. Since the three third-order signals, $\omega_{VIS} + 2\omega_{pump}$, $\omega_{VIS} + 2\omega_{probe}$, $\omega_{VIS} + \omega_{pump} + \omega_{probe}$, emerge at the same wavelength one needs to take advantage of their spatial separation and physically block $\omega_{VIS} + 2\omega_{pump}$ and $\omega_{VIS} + 2\omega_{probe}$ to prevent them from getting to the detector. The remaining signal can now be used to establish the pump-probe delay $t = 0$ and to determine the instrument response function as seen in figures 4.2 and 4.3.

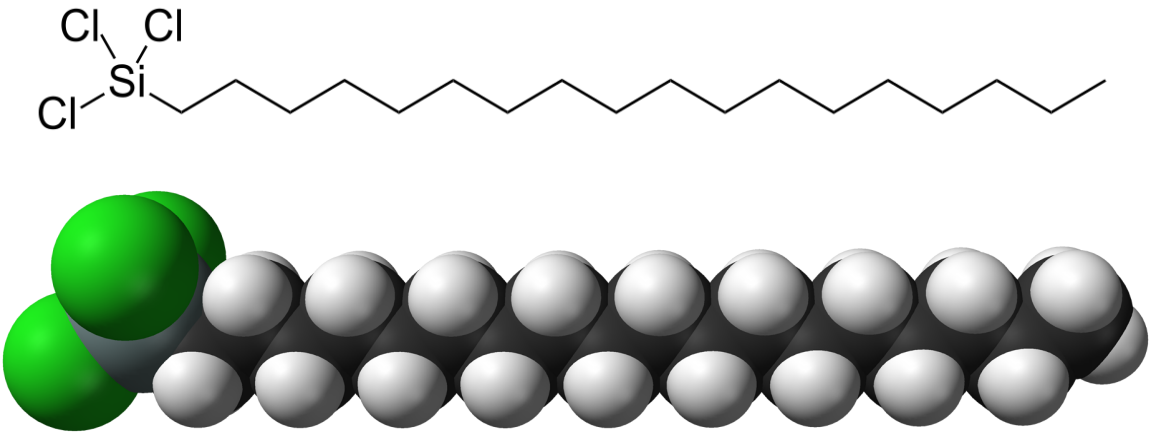

Figure 3.11: Chemical structure and space-filling-model of octadecyltrichlorosilane, CH_3 $(CH_2)_{17}$ $SiCl_3$. Colour code: Carbon, C: grey-black; Hydrogen, H: white; Chlorine, Cl: green; Silicon, Si: turqouise-grey. [5]

3.7 Sample preparation

For all experiments deionized H_2O (Millipore, $\geq 18\,M\Omega$) was used. The D_2O for isotopic dilution was obtained from Sigma-Aldrich (99.9%). A homemade Teflon cell was machined and covered with an IR grade fused silica isosceles trapezoidal prism with a base angle of 60°. The polar silanol groups terminating the fused silica prism provide a hydrophilic surface with which water molecules can form hydrogen bonds. In order to investigate dangling, non-hydrogen-bonded OH groups the fused silica prism is made hydrophobic by growing a self-assembled monolayer of octadecyltrichlorosilane (OTS), following a variation of the procedure outlined in the work by Sagiv.[41] The OTS molecule has a hydrophobic part consisting of a long alkyl group and a hydrophilic polar head group. Storage of OTS, therefore, needs to be in a dry atmosphere to prevent the OTS from reacting with any water. Furthermore, it is important that during the deposition process of the self-assembled monolayer, all beakers need to be pretreated and baked to get rid of excess water molecules.

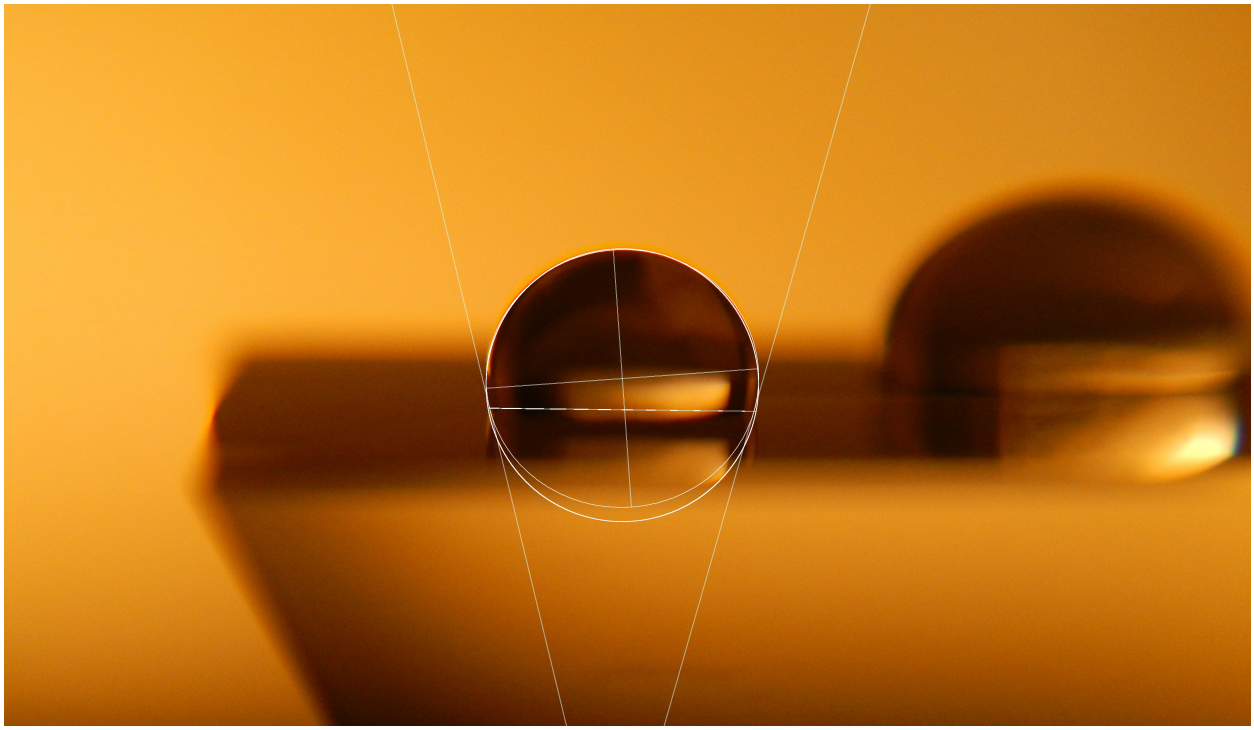

Figure 3.12: OTS coated prism. A circular fit yields a contact-angle of $\theta_C = 100.4 \pm 1.4^\circ$. An elliptic fit yields a contact-angle of $\theta_E = 104.8 \pm 0.94^\circ$.

3.7.1 Growing the octadecyltrichlorosilane self-assembled monolayer (OTS SAM)

To create the SAM on the fused silica prism the following protocol was used. First, the glassware is prepared by washing it with acetone, then methanol, followed by baking it at 150°C for 1 hour. The fused silica prism is pre-cleaned by sonicating it in acetone, then methanol and finally de-ionized water, each for 15 minutes. The prism is then placed into Nochromix oxidizer (Godax Laboratories) for several hours. In a separate beaker, 150 mL of solvent mixture is prepared by combining 120 mL n-hexadecane (Fisher Scientific, 99%), 18 mL carbon tetrachloride (Sigma-Aldrich, 99.5%) and 12 mL chloroform (DriSolv, 99%). The solution is stirred for 10 to 15 minutes. The prism is then taken out of the Nochromix, rinsed with deionized water and blown dry with dry nitrogen gas. Next, 0.15 mL OTS (VWR, 97%) is added to the solvent mixture and stirred until homogenized. Finally, the prism is placed into the OTS solution. The deposition is performed for 30 minutes while stirring. Afterward, the prism is rinsed in chloroform and dried for 1 hour at 50°C.

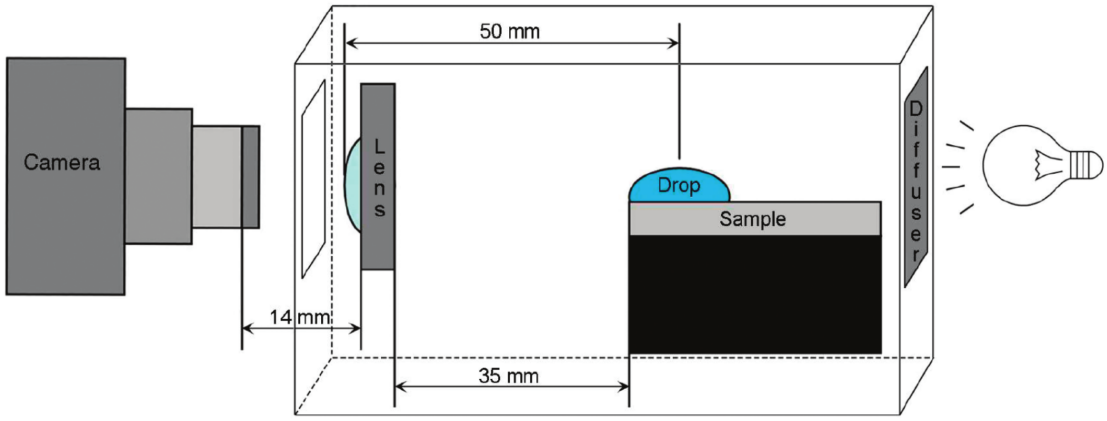

Figure 3.13: Setup by Lamour et al.[6] for the contact-angle measurement optimized for analysis with "ImageJ".

3.7.2 Contact-angle measurement

To determine the quality of the OTS monolayer, a contact-angle measurement is performed following the procedure outlined by Lamour and colleagues.[6] A drawing of the setup is depicted in figure 3.13. In short, a Nikon COOLPIX AW100 digital camera was mounted on the optics table just in front of a $f = 50\,\text{mm}$ lens. One focal length behind the lens a podium on a delay stage was set up that can support and translate the sample. In order to provide good contrast a light bulb and a diffuser was mounted behind the sample. A simple card board enclosure blocks the ambient light. The pictures were transfered to a lab computer where the contact-angles were measured with the ImageJ software [42] in combination with the contact angle plugin[43].

3.7.3 Removing the OTS SAM

To remove the OTS SAM, the prism is pre-cleaned, like previously described, with acetone, methanol and deionized water. The removal itself is done by 10 min of slow O_2 plasma etching with a pressure of 500 mTorr O_2 at 100 W, which leaves extremely hydrophobic fused silica behind.

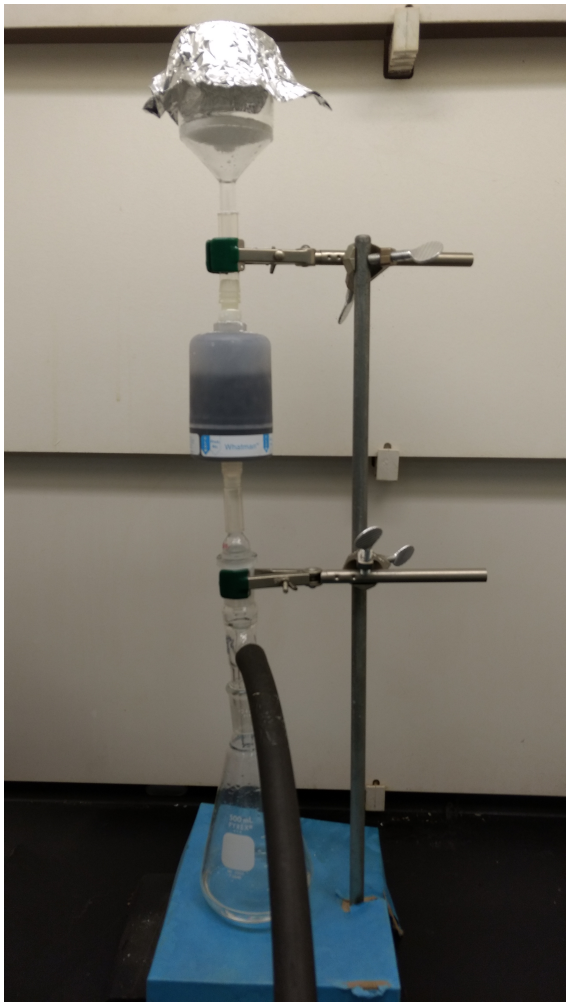

Figure 3.14: Apparatus equipped with a Whatman Carbon Cap 75 to filter salt solutions.

3.7.4 Preparation of salt solutions

Hua et al. have investigated the influence of contaminated salt solutions on SFG spectra.[44] Their recommendation with regard to eliminating organic contaminants can be summarized as follows. Metal-halide salts with high melting temperatures should be baked, then filtered. However, just baking and just filtering individually also yield SFG spectra indistinguishable from those obtained by baking and then filtering. Molecular ion based salts should only be baked if their melting point is high enough ($> 500^{\circ}$C) and then filtered. Hua et al. do not recommend baking only for molecular ion based salts with high melting temperatures and suggest to filter whether the melting temperature allows for baking or not.

3.7.4.1 Sodium chloride

Based on the research of Hua et al., sodium chloride (NaCl, Columbus Chemical Industries, ACS grade, ≥ 99.0) was baked for about 12 h at $\approx 650^{\circ}$C (melting temperature $T_m = 801^{\circ}$C), in a Thermolyne 48000 furnace. A 3 M solution was then prepared by dissolving 0.3 moles of NaCl ($u_{\mathrm{NaI}} = 58.44\,\frac{\mathrm{g}}{\mathrm{mol}}$), equivalent to 17.5 g in 100 mL filtered water from a Millipore Milli-Q water purification system. The solution was then filtered four times using a thoroughly rinsed Whatman Carbon Cap 75 filter with activated carbon from GE Healthcare Life Sciences shown in figure 3.14.

3.7.4.2 Sodium iodide

Similarly to sodium chloride, the sodium iodide (NaI, Sigma-Aldrich, ACS reagent, $\geq 99.5\%$) was baked for about 10 h at $\approx 600^{\circ}$C, approximately 60°C below its melting temperature ($T_m = 661^{\circ}$C), in a Thermolyne 48000 furnace. A 3 M solution was then prepared by dissolving 0.3 moles of NaI ($u_{\mathrm{NaI}} = 149.89\,\frac{\mathrm{g}}{\mathrm{mol}}$), equivalent to 45 g, in 100 mL filtered water from a Millipore Milli-Q water purification system. To prevent the oxidation reaction of the iodide ions, 50 mM of sodium thiosulfate pentahydrate ($Na_2S_2O_2{\cdot}5H_2O$, $u = 248.18\,\frac{\mathrm{g}}{\mathrm{mol}}$, Sigma-Aldrich, ACS reagent, 99.5%) was used by adding 1.24 g to the previous 3 M NaI solution. Furthermore, the solution was then filtered four times using the filter described in the previous section 3.7.4.1.

3.7.4.3 Magnesium sulfate

The magnesium sulfate ($MgSO_4$) solution was prepared with magnesium sulfate heptahydrate ($MgSO_4{\cdot}7H_2O$, $u = 246.47\,\frac{\mathrm{g}}{\mathrm{mol}}$, Sigma-Aldrich, ACS reagent, $\geq 99.0\%$) which starts to decompose at $\approx 150^{\circ}$C. Therefore, it was not baked. A three molar solution was prepared by dissolving 73.9 g of magnesium sulfate heptahydrate in 100 mL from the Millipore Milli-Q. Subsequently, the solution was filtered four times with the filter setup described in the previous section 3.7.4.1.

CHAPTER 4

ORIENTATIONAL DYNAMICS OF WATER AT AN EXTENDED HYDROPHOBIC INTERFACE

To investigate the orientational dynamics of water at an extended hydrophobic interface, we use the setup described in detail in Chapter 3. Specifically, figure 3.4 gives a good overview of the setup. In short, a fused silica prism is coated with an OTS self-assembled monolayer in order to produce an extended hydrophobic interface. VIS, pump and probe beams are overlapped at the water/OTS interface. The IR pulses of pump and probe are resonant with the dOH stretch mode (figure 4.1). By detecting the SFG signal of the probe and VIS from the water/OTS interface, the pump-induced bleach versus the pump-probe delay is measured. Moreover, to obtain further insight into the contribution of non-orientational mechanisms, isotopic dilution is used.

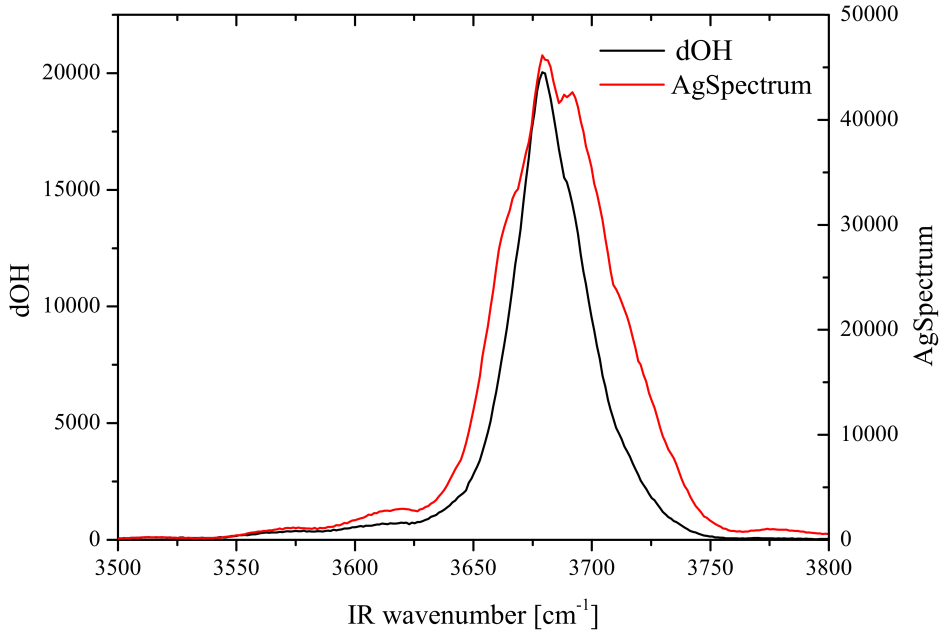

Figure 4.1: Red: IR spectrum with a $\approx 45\,\mathrm{cm}^{-1}$ full-width half-maximum determined from the probe SFG spectrum from a Ag mirror. Black: SFG spectrum of the dOH stretch at the fused-silica/ODS/H_2O interface.

4.1 Neat water

The normalized SFG probe intensity traces shown in figure 4.2 are fit with a biexponential decay:

$$I^{norm}(t) \equiv \frac{I(t)}{I(t<-1.2\,\mathrm{ps})} = 1 - A_1 \exp\left(-\frac{t-0.6\,\mathrm{ps}}{\tau_1}\right) - A_2 \exp\left(-\frac{t-0.6\,\mathrm{ps}}{\tau_2}\right). \tag{4.1}$$

Equivalently the bleach is fit by:

$$\beta(t) = 1 - I^{norm}(t) = A_1 \exp\left(-\frac{t-0.6\,\mathrm{ps}}{\tau_1}\right) + A_2 \exp\left(-\frac{t-0.6\,\mathrm{ps}}{\tau_2}\right) \tag{4.2}$$

Throughout this analysis we only fit to data points with a pump-probe delay of $t \geq 0.6\,\mathrm{ps}$, by which time the pump pulse has almost completely passed. For p-polarized pump, the result $\tau_1 = 1.34 \pm 0.03\,\mathrm{ps}$ for the fast decay time is consistent with earlier measurements at the water/OTS interface[27] but is substantially slower than the result (0.84 ps) for dOH at the water/air interface.[17] Table 4.1 provides an overview of the time constants obtained by the fitting procedure. Since at long delays the orientational anisotropy has decayed, p- and s-pump signals should be governed by the same slow dynamics associated with transient heating which is described in more detail below. Hence, τ_2, the time constant describing the slower dynamics is used globally to fit the data at long delays. The same fit can be done with isotopically diluted water. Here, the same slow dynamics as in the neat case is observed. However, the short dynamics are characterized by a $1.13 \pm 0.04\,\mathrm{ps}$ decay constant for p-pump and a $1.38 \pm 0.08\,\mathrm{ps}$ constant for s-pump. To further analyze the data we have to take into account that at long delays the bleach is proportional to the pump pulse energy absorbed at the surface, which depends on pump polarization and dOH polar distribution. The incomplete recovery on the long (50 ps) time scale can be explained by the aforementioned small,

	H_2O		1:2 H_2O:D_2O	
[ps]	p-pump	s-pump	p-pump	s-pump
τ_1	1.34 ± 0.03	1.55 ± 0.04	1.13 ± 0.04	1.38 ± 0.08
τ_2	15 ± 2		15 ± 2	

Table 4.1: Fast and slow time constants extracted from a fit to the data shown in figure 4.2

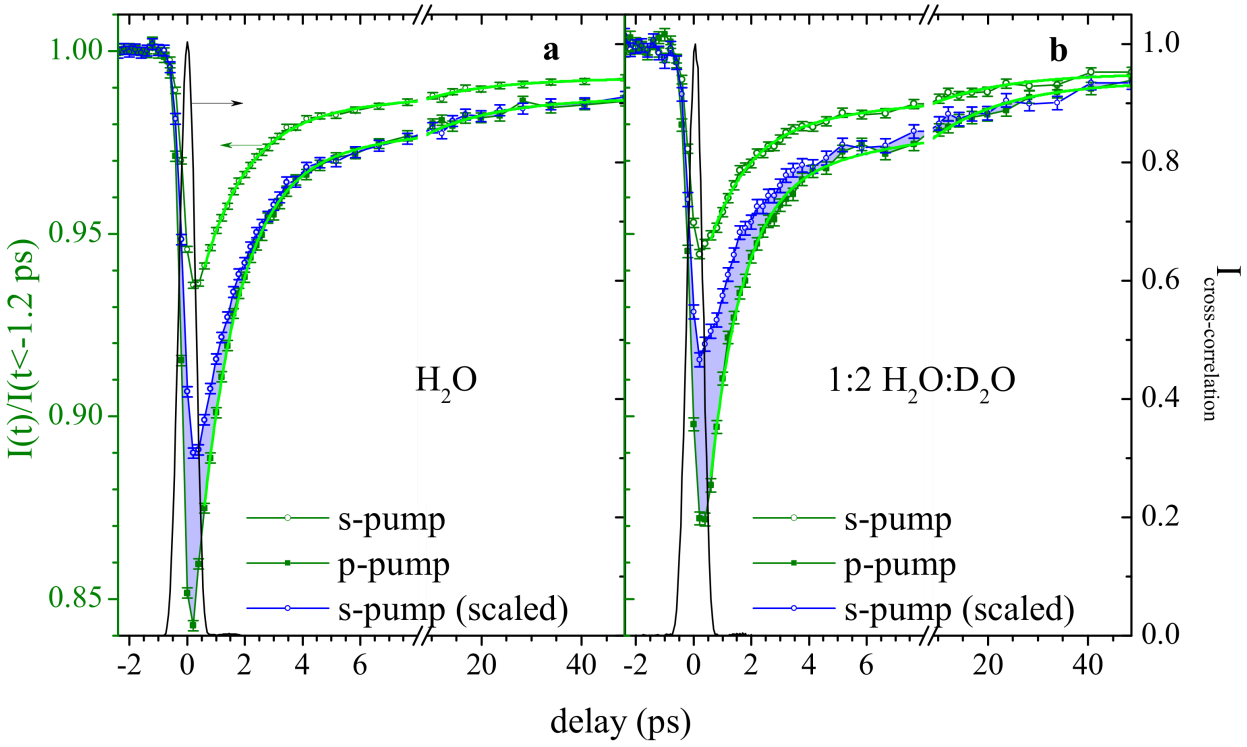

Figure 4.2: Time-resolved sum-frequency signal of the dOH stretch at the ODS/water interface normalized to the SFG signal at $t < -1.2\,\text{ps}$ for pure H_2O and H_2O:D_2O. The blue shading highlights the difference between p- and scaled s-pump data. The black curve is the third-order cross-correlation at $\omega = \omega_{\text{VIS}} + \omega_{\text{pump}} + \omega_{\text{probe}}$ recorded at the same configuration as the measurements to indicate $t = 0$ and the temporal resolution of our instrument. The bright green lines show biexponential fits to the data for $t \geq 0.6\,\text{ps}$.

transient rise in temperature. This leads to a weakening of hydrogen bonds close to the interface, causing a blueshift of the bOH spectrum. Phase resolved spectra by Tian et al. reveal the imaginary part of $\chi^{(2)}$ associated with the blue part of the bOH spectrum to be of opposite sign to the dOH contribution to $\chi^{(2)}$[2]. The blue shift of the bOH spectrum is, therefore, expected to reduce the magnitude of the SFG intensity from the dOH region with respect to the un-pumped sample and therefore prevents a complete recovery to a pre-pump value during the time scale depicted. With this knowledge we proceed by scaling the s-pump trace to match the p-pump trace at long delays:

$$I^{norm}_{s,scaled}(t) = 1 - \beta_{s,scaled}(t) \tag{4.3}$$

$$= 1 - \frac{\langle \beta_p(t > 15\,\text{ps}) \rangle}{\langle \beta_s(t > 15\,\text{ps}) \rangle} \beta_s(t). \tag{4.4}$$

Indeed, as one can see in figure 4.2 the dynamics of the p- and the scaled s-pump data at long delays are identical, while displaying significant differences at short delays.

In some samples, anomalies were observed: The SFG spectrum would exhibit a small second feature blueshifted by $10-20\,\mathrm{cm}^{-1}$ from the main feature at $3680\,\mathrm{cm}^{-1}$. In these cases, a rapidly decaying beating of the signal characterized by a frequency of $\approx 20\mathrm{cm}^{-1}$ and a decay constant $\approx 1\,\mathrm{ps}$ was visible in the time-resolved traces. This phenomenon has been described by Ye et al.[45] and in the work of Eftekhari-Bafrooei[46]. It is caused by water molecules that are trapped between the OTS monolayer and the fused silica. These water molecules are essentially decoupled from the water at the water/OTS interface or the bulk. To minimize the contribution from the trapped water molecules we focus on those samples that did not display any of the signs just mentioned.

We focus on the fast dynamics by calculating the difference between the p- and scaled s-pump bleach traces:

$$\Delta\beta(t) = \beta_p(t) - \beta_{s,scaled}(t) \tag{4.5}$$

and the average of the p- and scaled s-pump bleach traces:

$$\bar{\beta}(t) = \frac{1}{2}\left[\beta_p(t) + \beta_{s,scaled}(t)\right]. \tag{4.6}$$

Figure 4.3 shows $\Delta\beta(t)$ and $\bar{\beta}'(t)$, which is the average bleach $\bar{\beta}(t)$ minus its long-delay value:

$$\bar{\beta}'(t) = \bar{\beta}(t) - \bar{\beta}(t > 25\,\mathrm{ps}). \tag{4.7}$$

According to equation 2.73, $\Delta\beta(t)$ is fit with a single exponential decay starting at $t_0 = 0.6\,\mathrm{ps}$, just after the pump pulse has passed:

$$\Delta\beta(t;t_0) = A\exp\left(-\frac{t-t_0}{\tau_{\Delta\beta}}\right). \tag{4.8}$$

$\bar{\beta}'(t)$ is fit according to equation 2.74 with a double exponential decay

$$\bar{\beta}'(t;t_0) = B_1\exp\left(-\frac{t-t_0}{T_1}\right) + B_2\exp\left(-\frac{t-t_0}{\tau_2}\right). \tag{4.9}$$

$\bar{\beta}'(t;t_0 = 0.6\,\text{ps})$	$\bar{\beta}'(t;t_0 = 2.0\,\text{ps})$	$\Delta\beta(t;t_0 = 0.6\,\text{ps})$
$T_1 = 1.42 \pm 0.02\,\text{ps}$	$T_1 = 1.46 \pm 0.06\,\text{ps}$	$\tau_{\Delta\beta} = 0.74 \pm 0.05\,\text{ps}$
$\tau_{\beta\text{slow}} = 15\,\text{ps}$ *		

Table 4.2: Time constants extracted from fits to $\Delta\beta$ and $\bar{\beta}'$ shown in figure 4.3. * = fixed parameter.

The fit is performed twice, starting at $t_0 = 0.6\,\text{ps}$ and at $t_0 = 2.0\,\text{ps}$ and the time constants from the fits are listed in table 4.2. The compatibility of the fast time constants obtained by the two biexponential fits of $\bar{\beta}'(t)$ starting at 0.6 ps and 2.0 ps indicates that the anisotropy underlying $\Delta\beta(t)$ does not contribute significantly to $\bar{\beta}'(t)$. This is consistent with the earlier discussion of equation 2.74, where it was established that $\bar{\beta}'(t)$ is only expected to have a weak dependence on orientational dynamics. To rule out small contributions of orientational dynamics, the rate $k_{dOH} = \frac{1}{T_1} = (1.46 \pm 0.06\,\text{ps})^{-1}$ from the fit starting at 2.0 ps is used for further analysis. To calculate the rate k_{or} associated with the pump-induced orientational anisotropy, equation 2.73 is used:

$$k_{or} = k_{\Delta\beta} - k_{dOH} \tag{4.10}$$

$$= (0.74\,\text{ps})^{-1} - (1.46\,\text{ps})^{-1} \tag{4.11}$$

$$= 0.67\,\text{ps}^{-1} = (1.50\,\text{ps})^{-1} \tag{4.12}$$

The uncertainty in k_{or} can be calculated using $\frac{\delta k_{\Delta\beta}}{k_{\Delta\beta}} = \frac{\delta\tau_{\Delta\beta}}{\tau_{\Delta\beta}}$ and $\frac{\delta k_{dOH}}{k_{dOH}} = \frac{\delta T_1}{T_1}$:

$$\delta k_{or} = \sqrt{\delta k_{\Delta\beta}^2 + \delta k_{dOH}^2} \tag{4.13}$$

$$= \sqrt{\left(\frac{\delta\tau_{\Delta\beta}}{\tau_{\Delta\beta}} k_{\Delta\beta}\right)^2 + \left(\frac{\delta T_1}{T_1} k_{dOH}\right)^2} \tag{4.14}$$

$$= \sqrt{\left(\frac{0.05\,\text{ps}}{0.74\,\text{ps}} \times \frac{1}{0.74\,\text{ps}}\right)^2 + \left(\frac{0.06\,\text{ps}}{1.46\,\text{ps}} \times \frac{1}{1.46\,\text{ps}}\right)^2} \tag{4.15}$$

$$= 0.096\,\text{ps}^{-1} \tag{4.16}$$

The uncertainty of $\tau_{or} = \frac{1}{k_{or}} = 1.50\,\text{ps}$ is

$$\delta\tau_{or} = \frac{\delta k_{or}}{k_{or}}\tau_{or} \tag{4.17}$$

$$= \frac{0.096\,\text{ps}^{-1}}{0.67\,\text{ps}^{-1}} \times \frac{1}{0.67\,\text{ps}^{-1}} \tag{4.18}$$

$$= 0.22\,\text{ps} \tag{4.19}$$

To conclude:

$$k_{or} = 0.67 \pm 0.10\,\text{ps}^{-1} = (1.50 \pm 0.22\,\text{ps})^{-1} \tag{4.20}$$

Notably, k_{or} is within error the same as k_{dOH}. This is not a coincidence. Rather, since the experimental setup is mainly probing $\chi^{(2)}_{zzz}$, it is sensitive to molecular orientational motions that involve the change in the polar angle θ. Such motion leads to the decay of the pump-induced anisotropy, but it also contributes to population decay by reconfiguring the dOH to a bOH. Keeping in mind that the stretch frequency of a bOH red shifts out of the detection region, this reorientation process appears as part of the population decay.

At this point, it is possible that k_{or} is not purely determined by molecular reorientation. Other processes, like dipole-dipole coupling, intra-molecular energy transfer or intra-molecular vibrational relaxation, described in section 2.4, might alter the angular distribution of excited and ground-state dOH stretch populations without changing the actual orientation of the dOH groups that are involved. Sufficient isotopic dilution of the H_2O sample reduces the latter pathways and helps establish a more reliable rate for the molecular reorientational motion.

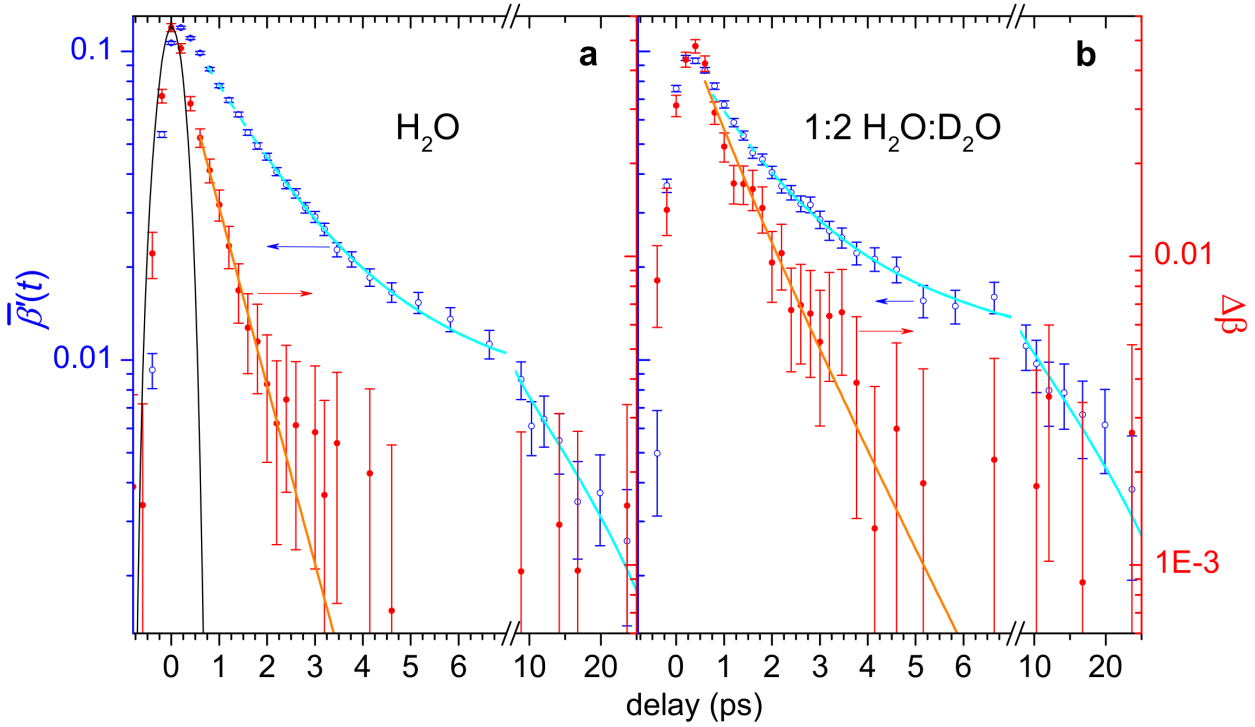

Figure 4.3: dOH stretch SFG dynamics at the ODS/H_2O and ODS/H_2O:D_2O interfaces showing the decay of the average bleach $\bar{\beta}'(t)$ (open blue circles) relative to the long-decay bleach and the difference $\Delta\beta(t)$ (solid red circles) between the p-pump and scaled s-pump data. Solid curves show biexponential fits (cyan) for $t \geq 2.0\,\text{ps}$ and single-exponential fits (orange) for $t \geq 0.6\,\text{ps}$. The third-order cross correlation is shown in solid black.

4.2 Isotopically Diluted Water

As elaborated in section 2.5, a sample with isotopically diluted water can give further insight into how much non-orientational mechanisms, such as IET, IVR or dipole-dipole interactions, contribute to the decay of pump-induced anisotropy. If they indeed play a significant role it is expected that isotopic dilution will slow the observed dynamics due to the reduction of their respective rates. Here, we use a molar ratio of 1:2 of H_2O:D_2O, which after equilibration leads to the ratio 1:4:4 of H_2O:HDO:D_2O. This means that there are two species of dOH: Those associated with an H_2O molecule and those associated with an HDO molecule. Under the assumption that intermolecular dynamics remain unchanged for the H_2O molecules in the isotopic mixture, it is assumed that 1/3 of the signal decays following the neat water dynamics while the remaining 2/3 reflects the new

dynamics of the HDO molecules. In reality intermolecular dynamics of H_2O molecules are slowed by isotopic dilution. Therefore, any actual slowing of H_2O dynamics will manifest in the HDO time constant and yield a slower-than-actual time constant for the HDO dynamics. The fit of $\bar{\beta}'(t)$ is performed with a triple exponential decay consisting of the double exponential decay of neat H_2O plus one additional exponential decay with a fast time constant to capture the HDO dynamics

$$\bar{\beta}'^{HDO}(t) = B_3 \left[\frac{1}{3} \times \exp\left(-\frac{t - 2.0\,\mathrm{ps}}{1.46\,\mathrm{ps}} \right) + \frac{2}{3} \times \exp\left(-\frac{t - 2.0\,\mathrm{ps}}{\tau_{dOH}^{HDO}} \right) \right] + B_4 \exp\left(-\frac{t - 2.0\,\mathrm{ps}}{15\,\mathrm{ps}} \right) + y_0 \tag{4.21}$$

and yields

$$k_{dOH}^{HDO} = \frac{1}{\tau_{dOH}^{HDO}} = (1.41 \pm 0.21\,\mathrm{ps})^{-1}. \tag{4.22}$$

This is statistically indistinguishable from the population decay in neat H_2O determined in the previous section $k_{dOH} = (1.46 \pm 0.06\,\mathrm{ps})^{-1}$. This indicates that population dynamics are not significantly affected by isotopic dilution. With the further assumption that orientational motion is identical for H_2O and D_2O, one can fit $\Delta\beta^{HDO}(t)$ obtained from the isotopic dilution with a single-exponential decay, which yields $k_{\Delta\beta}^{HDO} = (1.02 \pm 0.08\,\mathrm{ps})^{-1}$. Analogous to the neat water case we subtract the population decay to obtain the reorientation time

$$k_{or}^{HDO} = k_{\Delta\beta}^{HDO} - k_{dOH}^{HDO} \tag{4.23}$$

$$= (1.02\,\mathrm{ps})^{-1} - (1.41\,\mathrm{ps})^{-1} \tag{4.24}$$

$$= 0.27\,\mathrm{ps}^{-1} = (3.7\,\mathrm{ps})^{-1} \tag{4.25}$$

and its uncertainty

$$\delta k_{or}^{HDO} = \sqrt{\left(\delta k_{\Delta\beta}^{HDO}\right)^2 + \left(\delta k_{dOH}^{HDO}\right)^2} \tag{4.26}$$

$$= \sqrt{\left(\frac{\delta \tau_{\Delta\beta}^{HDO}}{\tau_{\Delta\beta}^{HDO}} k_{\Delta\beta}^{HDO} \right)^2 + \left(\frac{\delta T_1^{HDO}}{T_1^{HDO}} k_{dOH}^{HDO} \right)^2} \tag{4.27}$$

$$= \sqrt{\left(\frac{0.08\,\mathrm{ps}}{1.02\,\mathrm{ps}} \times \frac{1}{1.02\,\mathrm{ps}} \right)^2 + \left(\frac{0.21\,\mathrm{ps}}{1.41\,\mathrm{ps}} \times \frac{1}{1.41\,\mathrm{ps}} \right)^2} \tag{4.28}$$

$$= 0.13\,\mathrm{ps}^{-1} \tag{4.29}$$

or

$$\delta\tau_{or}^{HDO} = \frac{\delta k_{or}^{HDO}}{k_{or}^{HDO}}\tau_{or}^{HDO} \tag{4.30}$$

$$= \frac{0.13\,\mathrm{ps}^{-1}}{0.27\,\mathrm{ps}^{-1}} \times \frac{1}{0.27\,\mathrm{ps}^{-1}} \tag{4.31}$$

$$= 1.8\,\mathrm{ps}. \tag{4.32}$$

It seems from $k_{or}^{HDO} = (3.7 \pm 1.8\,\mathrm{ps})^{-1}$ that the reorientation has slowed upon isotopic dilution. However, the reduced signal-to-noise ratio that comes hand in hand with isotopic dilution, results in a less accurate scaling of the s-pump data than in the case of neat water. In addition, $k_{\Delta\beta}$ is determined from a difference of the p- and scaled s-pump traces and so is more susceptible to inaccuracies than the average k_{dOH}. This leads to the large uncertainty that allows for any reasonable value within two standard deviations.

4.3 Experimental rates and uncertainties

After examining the decay mechanisms of the dOH stretch vibration summarized in table 2.1, it is apparent that for pure water $k_{IVR}^{b}, k_{p-p}^{b\to b} \gg k_{IET}^{F}, k_{or}$. Therefore, the effectively irreversible population decay described by $k_{dOH} = 1/T_1$ of dOH to bOH is governed by k_{IET}^{F} and k_{or}. The orientational dynamics include out-of-plane (k_{jump}^{F}) and in-plane (k_{ip}) reorientational dynamics

$$k_{or} = k_{jump}^{F} + k_{ip}, \tag{4.33}$$

whereas, as discussed before in section 2.3.1, of the two orientational processes only the out-of-plane reorientation contributes to population decay which leaves us with the following rate equation:

$$k_{dOH} = k_{jump}^{F} + k_{IET}^{F}. \tag{4.34}$$

The average bleach $\bar{\beta}'$ which is accessed experimentally is representative of population decay, and hence we can write:

$$k_{\bar{\beta}'} \equiv k_{dOH} = k_{jump}^{F} + k_{IET}^{F}. \tag{4.35}$$

In addition, the measurement of the isotopically diluted water, where k_{IET}^{F} is essentially turned off, the above equation can be simplified to

$$k_{\bar{\beta}'}^{HDO} \equiv k_{dOH}^{HDO} \approx k_{jump}^{F}. \tag{4.36}$$

The third experimentally measured quantity is the difference between p- and s-pump bleach $\Delta\beta$. There, the contributions are population decay and orientational dynamics. Using equation 4.33 and 4.34 we arrive at

$$k_{\Delta\beta} = k_{or} + k_{dOH} = 2k_{jump}^{F} + k_{ip} + k_{IET}^{F}. \tag{4.37}$$

To summarize, we have three equations (4.35, 4.36, and 4.37) and in principle three unknowns (k_{jump}^{F}, k_{ip}, and k_{IET}^{F}). Although, k_{IET}^{F} can be calculated as described in section 2.4.3, its uncertainty is still unknown.

4.3.1 Determination of the uncertainty of k_{IET}^{F}

An estimation of the uncertainty of k_{IET}^{F} can be obtained from our measurements by subtracting equation 4.36 from 4.35:

$$k_{IET}^{F} \approx k_{\bar{\beta}'} - k_{\bar{\beta}'}^{HDO} \tag{4.38}$$

$$\approx \frac{1}{1.46\,\mathrm{ps}} - \frac{1}{1.41\,\mathrm{ps}} \tag{4.39}$$

$$\approx -0.024\,\mathrm{ps}^{-1} \tag{4.40}$$

and

$$\sigma(k_{IET}^{F}) = \sqrt{\sigma\left(k_{\bar{\beta}'}\right)^2 + \sigma\left(k_{\bar{\beta}'}^{HDO}\right)^2} \tag{4.41}$$

$$= \sqrt{(0.028\,\mathrm{ps}^{-1})^2 + (0.106\,\mathrm{ps}^{-1})^2} \tag{4.42}$$

$$= 0.109\,\mathrm{ps}^{-1}. \tag{4.43}$$

From this result, $k_{IET}^{F} = -0.024 \pm 0.109\,\mathrm{ps}^{-1}$, the conclusion is that the upper limit of k_{IET}^{F} is $k_{IET,max}^{F} = (-0.024 + 0.109)\,\mathrm{ps}^{-1} = 0.085\,\mathrm{ps}^{-1}$. Taking the difference with the value for k_{IET}^{F}

determined in section 2.4.3, $0.077\,\mathrm{ps}^{-1}$, the upper uncertainty is now evaluated to be $\sigma^{+}\left(k_{IET}^{F}\right) = 0.007\,\mathrm{ps}$). On the lower side, the experimentally obtained uncertainty would encompass unphysical values. It is therefore reasonable to limit the uncertainty to the physical range: $k_{IET,min}^{F} = 0$. To conclude:

$$k_{IET}^{F} = 0.077^{+0.007}_{-0.077}\,\mathrm{ps}^{-1} = \left(13^{+\infty}_{-1.24}\,\mathrm{ps}\right)^{-1} \tag{4.44}$$

Note, that the experimental data does not provide an upper limit for the IET timescale.

4.3.1.1 Additional constrains for k_{IET}^{F} based on the research literature

It is possible to determine, not just the value of k_{IET}^{F} as outlined earlier in section 2.4.3, but also the uncertainty based on the literature. The way k_{IET}^{F} was calculated involves the coupling between the bOH and dOH stretch modes, the frequency difference between the uncoupled modes, and the rate describing the intramolecular vibrational relaxation:

$$k_{IET}^{F} = \left|\frac{\gamma}{\delta}\right|^{2} k_{IVR}^{b}. \tag{4.45}$$

In order to calculate a reasonable uncertainty for k_{IET}^{F}, the uncertainties of γ, δ, and k_{IVR}^{b} are needed.

Uncertainty of the coupling γ The uncertainty of the coupling between the bOH and dOH stretch modes on the same molecule can be inferred from the work of Stiopkin et al.[32] There, they describe the coupling between a dOD and the bOD on the same D2O molecule to be $\gamma_{D_2O} = -48\,\mathrm{cm}^{-1}$ with a FWHM of $\approx 12\,\mathrm{cm}^{-1}$. This corresponds to a standard deviation of $\sigma(\gamma_{D_2O}) = 5.1\,\mathrm{cm}^{-1}$. Since the coupling in the case of H_2O is just

$$\gamma = \frac{-50}{-60} \times \gamma_{D_2O}, \tag{4.46}$$

the uncertainty of γ is simply calculated as follows:

$$\sigma(\gamma) = \frac{-50}{-60} \times \sigma(\gamma_{D_2O}). \tag{4.47}$$

To conclude: $\gamma = -40 \pm 4.25\,\mathrm{cm}^{-1}$.

Uncertainty of the frequency difference δ It is known that a bOH group, associated with a water molecule at the surface that exhibits a dOH has stretch frequency on the blue end of the broad bOH spectrum that includes other bOH groups. Ni et al. calculate the spectrum of these particular bOH groups to be at $3480\,\mathrm{cm}^{-1}$ with a FWHM of about $239\,\mathrm{cm}^{-1}$. The spectrum of dOH groups at $3680\,\mathrm{cm}^{-1}$ is very narrow compared to this. This corresponds to a standard deviation of $\sigma(\delta) = 101\,\mathrm{cm}^{-1}$. As it turns out, the uncertainty term resulting from this is three magnitudes larger than the other contributions and not likely to be representative of the actual uncertainty of the frequency difference $\delta = 157\,\mathrm{cm}^{-1}$. In reality, the uncertainty should be significantly smaller. This discussion continues in paragraph 4.3.1.1.

Uncertainty of k^b_{IVR} The source of the value for k^b_{IVR} specifies the uncertainty $\sigma(T^b_{IVR}) = 0.05\,\mathrm{ps}$.[30], therefore

$$k^b_{IVR} = (0.75 \pm 0.05\,\mathrm{ps})^{-1} = 1.33 \pm 0.09\,\mathrm{ps}^{-1}. \tag{4.48}$$

Uncertainty of k^F_{IET} Having determined the uncertainties of γ, δ, and k^b_{IVR} the uncertainty of k^F_{IET} can be calculated with the following formula:

$$\sigma(k^F_{IET}) = \sqrt{\left(2\frac{\gamma}{\delta^2}k^b_{IVR}\sigma(\gamma)\right)^2 + \left(-2\frac{\gamma^2}{\delta^3}k^b_{IVR}\sigma(\delta)\right)^2 + \left(\frac{\gamma^2}{\delta^2}\sigma(k^b_{IVR})\right)^2}. \tag{4.49}$$

As indicated, the uncertainty of δ is not exactly known. Ignoring it ($\sigma(\delta) = 0$) or using the standard deviation of δ as an upper limit are the extreme ends of this estimate. At this point, the real quantity of the uncertainty is not know. Rather than ignoring the uncertainty of δ or randomly using a value in between, this dissertation uses the standard deviation of δ ($\sigma\delta = 101\,\mathrm{cm}^{-1}$) to continue. This will yield larger uncertainties, however, one can be sure that it will encompass the real values.
Inserting the values obtained in the earlier sections yields and remembering the value of k^F_{IET} obtained in section 2.4.3:

$$k^F_{IET} = 0.077 \pm 0.114\,\mathrm{ps}^{-1} = (13 \pm 19\,\mathrm{ps})^{-1}. \tag{4.50}$$

The uncertainty obtained above includes negative, and therefore unphysical, values of k_{IET}^{F}. On the other hand, it provides an upper limit for k_{IET}^{F}:

$$k_{IET}^{F} < 0.190\,\mathrm{ps}^{-1} = (5.25\,\mathrm{ps})^{-1}\,. \tag{4.51}$$

Combining the constraints of k_{IET}^{F} Unfortunately, with the lack of knowledge about a reasonable value for the uncertainty of δ, using the research literature is not helpful to further constrain the experimentally obtained uncertainty of k_{IET}^{F}. The approach laid out, could be helpful to determine a more reasonable value for $\sigma(k_{IET}^{F})$ in the future once the uncertainty of δ has been determined. Continuing from here, solely the experimentally obtained uncertainties are used:

$$k_{IET}^{F} = 0.077^{+0.007}_{-0.077}\,\mathrm{ps}^{-1} = \left(13^{+\infty}_{-1.24}\,\mathrm{ps}\right)^{-1} \tag{4.52}$$

4.3.2 Determination of the uncertainty of k_{jump}^{F}

Finally, the forward out-of-plane jump rate is calculated through equation 4.35:

$$k_{jump}^{F} = k_{\bar{\beta}\prime} - k_{IET}^{F}. \tag{4.53}$$

Since k_{IET}^{F} has asymmetric uncertainties, the uncertainty of k_{jump}^{F} will also be asymmetric. However, since in the process of calculating k_{jump}^{F} the rates are subtracted, the upper limit of k_{IET}^{F} will determine the lower limit of k_{jump}^{F}:

$$\sigma^{\pm}\left(k_{jump}^{F}\right) = \sqrt{\left(\sigma(k_{\bar{\beta}\prime})\right)^{2} + \left(\sigma^{\mp}(k_{IET}^{F})\right)^{2}}. \tag{4.54}$$

The result is:

$$k_{jump}^{F} = 0.608^{+0.082}_{-0.029}\,\mathrm{ps}^{-1} = \left(1.64^{+0.08}_{-0.22}\,\mathrm{ps}\right)^{-1}. \tag{4.55}$$

4.3.3 Determination of the in-plane reorientation

Using equation 4.37 derived in the previous section the rate for in-plane reorientational dynamics can be determined:

$$k_{ip} = k_{\Delta\beta} - 2k_{jump}^{F} - k_{IET}^{F}. \tag{4.56}$$

Again, since the quantities k^F_{jump} and k^F_{IET}, their upper uncertainties will contribute to the lower uncertainty of k_{ip}:

$$\sigma(k_{ip})^{\pm} = \sqrt{\left(\sigma(k_{\Delta\beta})\right)^2 + \left(2\sigma^{\mp}(k^F_{jump})\right)^2 + \left(\sigma^{\mp}(k^F_{IET})\right)^2}. \tag{4.57}$$

This results in $\sigma(k_{ip})^- = 0.19\,\mathrm{ps}^{-1}$ and $\sigma(k_{ip})^+ = 0.13\,\mathrm{ps}^{-1}$. Since the lower uncertainty includes negative unphysical values the uncertainty is truncated to match $k_{ip,min} = 0$:

$$k_{ip} = 0.06^{+0.13}_{-0.06}\,\mathrm{ps}^{-1} = \left(17^{+\infty}_{-12}\,\mathrm{ps}\right)^{-1}. \tag{4.58}$$

Similarly to the determination of the uncertainty of k^F_{IET}, the experiment only yield a meaningful upper limit of the in-plane reorientation rate: $k_{ip} < 0.19\,\mathrm{ps}^{-1} \approx (5ps)^{-1}$.

A hand-waving argument can be made as to why it is expected that in-plane reorientation is slower than out-of-plane reorientation: In contrast to out-of-plane reorientation, in-plane reorientation requires the breaking of an hydrogen bond and consequently the formation of a new one. In bulk, the process of breaking, reorientation of the molecule, and reforming of an hydrogen bond is associated with a time scale of $k_{bulk} = (3.3\,\mathrm{ps})^{-1}$.[10] However, in bulk, this process is the result of either the rotation about the x, y, or z axis. All three rotations are equally likely in bulk ($k_\phi = k_\theta$), whereas at the interface (here the z-axis is fixed to be normal to the interface), due to the broken symmetry, the situation is different. Imagining that the pump and probe pulses are polarized in z-direction, only in-plane reorientation, described by rotations about the z-axis, do not appear like reorientation. In contrast, reorientation about the x- or y-axis look like a forward jump. Therefore, this hand-waving argument is described by the following rate equation:

$$k_{bulk} = k_x + k_y + k_z \tag{4.59}$$

$$= 3k_{ip}, \tag{4.60}$$

where k_{ip} is the in-plane reorientation at the interface. This implies that we expect $k_{ip} = k_{bulk}/3 = (9.9\,\mathrm{ps})^{-1}$, which is certainly compatible with the result derived from our data. In addition to this simple argument, Stirnemann et al. arrive at 9.6 ps in their MD simulations for in-plane reorientation.[10]

	H_2O		H_2O::D_2O	
	k [ps^{-1}]	τ [ps]	k [ps^{-1}]	τ [ps]
experimental values				
$\bar{\beta}'$	0.685 ± 0.028	1.46 ± 0.06	0.709 ± 0.106	1.41 ± 0.21
$\Delta\beta$	1.351 ± 0.091	0.74 ± 0.05	0.98 ± 0.08	1.02 ± 0.08
calculated values				
IET	$0.077^{+0.007}_{-0.077}$	$13.0^{+\infty}_{-1.2}$		
jump^F	$0.608^{+0.082}_{-0.029}$	$1.64^{+0.08}_{-0.22}$		
ip	$0.06^{+0.13}_{-0.06}$	$17^{+\infty}_{-12}$		

Table 4.3: Summary table of experimentally obtained and calculated values.

4.4 Summary and interpretation by MD simulations

Using high sensitivity time-resolved pump-probe SFG spectroscopy in TIR geometry, the orientational dynamics for the out-of-plane orientation of dangling OH bonds at the water/hydrophobic interface occurs on a $1.64^{+0.08}_{-0.22}$ ps timescale.

The out-of-plane reorientation time obtained in this dissertation is twice as fast as the orientational motion of water in bulk and about 50% slower than the out-of-plane orientational motion at the water/air interface.

Furthermore, the in-plane orientational dynamics have been examined. In this case, the scope of this dissertation only yields a lower boundary of $k_{ip} > 5$ ps. This is compatible with expectations and values found in the research literature.

4.4.1 MD simulations and interpretation

Our collaborators, Guillaume Stirnemann and Damien Laage, conducted MD simulations comparing the water/air and water/hydrophobic interfaces.[4] They replicated and refined the results of simulations that have been conducted individually on water/air and water/hydrophobic interfaces. The key points of their work were the simulation of both interfaces with the same model and to implement the instantaneous surface, a more reliable description of the water surface. Previously,

simulations would consider the flat average Gibbs interface which ignores ripples at the interface (figure 4.4 a, b). This detail is of importance because the dOH groups are determined by geometric properties that use the surface as reference system. Modeling the surface more accurately should therefore lead to more accurate results. For the reorientation time of the dOH they obtain 1.4 ps at the water/air interface and 1.7 ps at the water/hydrophobic interface (figure 4.4 c). Independent of the approach used in this dissertation, the uncertainties do not allow a clear experimental distinction between the values obtained from the MD simulations. If the uncertainty of k^F_{IET} is determined using our experimental data, there is a slight bias towards k^F_{jump} being compatible with the MD result for the water/hydrophobic interface.

The MD result for the water/air interface is slightly slower than the 1.1 ps previously reported experimentally by Hsieh et al. and backed by 0.8 ps from MD simulations by Verde et al. [17, 16]. The difference in the MD simulation results are sought to be the result of the improved modeling of the surface. On the experimental side, the signal-to-noise ratio in the data of Hsieh et al. makes it difficult to discriminate experimentally between the different simulation results.

By investigating the free energy difference between the two interfaces (figure 4.4 d), Stirnemann and Laage found that the dOH configuration experiences a stabilization at the water/hydrophobic interface compared to the water/air interface which corresponds to a slowdown of dOH jump dynamics by $\exp(\Delta F_{dOH}/k_B T) \approx 1.2$ and agrees with the ratio they obtained: $1.7\,\text{ps}/1.4\,\text{ps} = 1.2$.

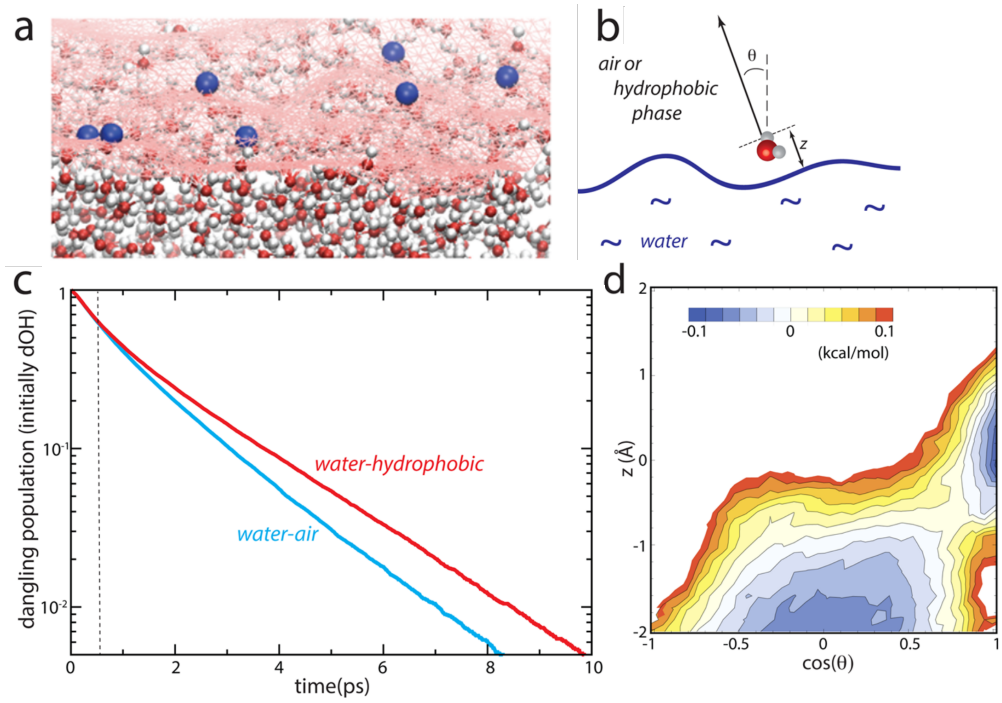

Figure 4.4: MD simulations by Stirnemann and Laage: a) MD snapshot of the water/air interface showing the instantaneous interface as a red mesh. b) Definition of the OH group angle θ and the distance to the instantaneous interface z. c) Population decay of dOH→bOH for water/air and water/hydrophobic interfaces. d) Free energy difference ΔF_{dOH} of the water/air and water/hydrophobic interface.[4]

CHAPTER 5

SALT SOLUTIONS

A well documented macroscopic phenomenon is that aqueous salt solutions have a different viscosity[47] and surface tension than neat water.[48] For a long time the change in viscosity was assumed to be largely related to the strong effect of the ions on the hydrogen bond network.[49] Some ions seem to enhance the hydrogen bond network ("structure makers") while others seem to disrupt it ("structure breakers"). Since 1934 until the 1990s, it was understood that the change in surface tension was caused by a surface ion concentration that is lower than in the bulk[50], which was understood in terms of repulsion of ions from the interface by electrostatic image forces.[51]

5.1 Previous research on bulk salt solutions

Due to the difficulty in distinguishing hydrogen bonds formed by water molecules surrounding ions from the hydrogen bonds of bulk water, molecular dynamic simulations have preceded

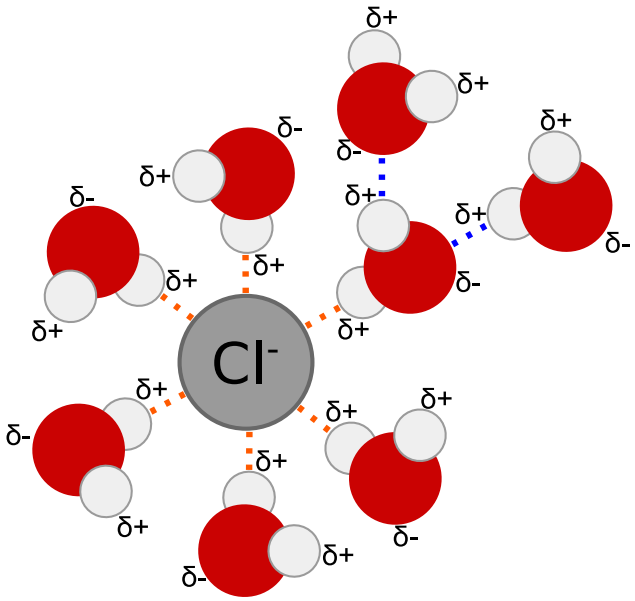

Figure 5.1: Solvated anions, like Cl^-, form hydrogen bonds with surrounding water molecules ($OH\cdots Cl^-$, orange). These hydrogen bonds can have a different absorption spectrum than bOH in bulk water ($OH\cdots O$, blue).

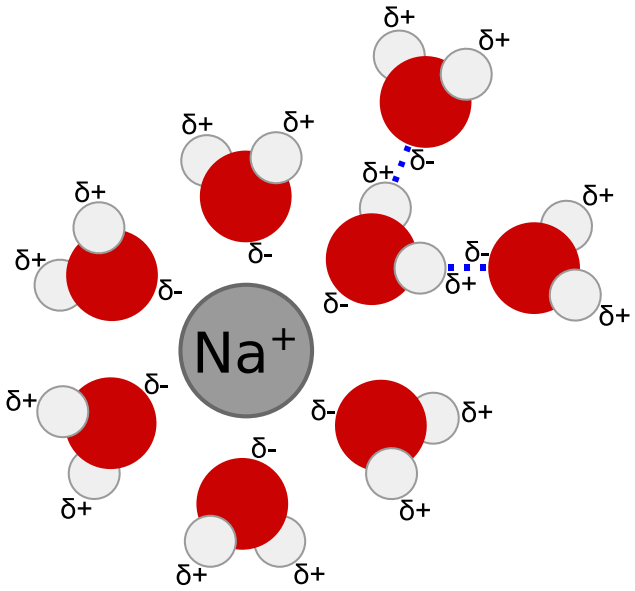

Figure 5.2: Solvated cations, like Na^+, do not form hydrogen bonds with the surrounding water molecules. Due to the positive charge of the cation, the water molecules orient themselves so that the partially positive hydrogen atoms face away from the cation. The hydrogen bonds formed by water molecules in the first solvation shell (OH···O, blue) already exhibit the same frequencies as bOH in bulk.

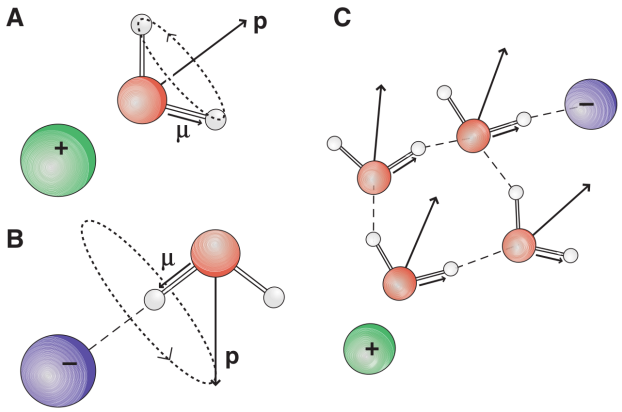

Figure 5.3: Tielrooij et al.[7] show that in a semi-rigid hydration shell water molecules are only locked in one direction (A,B) and the cooperative interaction of cation and anion that locks water molecules in two directions (C) while involving water molecules beyond the first solvation shell.

experiments in answering questions related to the presence of ions at water surfaces. X-ray and neutron diffraction have been used to examine structural properties in salt solutions like coordination numbers and ion-water distances. However, they lack the ability to provide information about dynamics.[52, 53, 54] Nuclear magnetic resonance is able to measure the reorientation time of water molecules, but lacks the specificity required to distinguish bulk water hydrogen bonds from hydrogen bonds in the hydration shell around the ions.[55, 56] The group led by Bakker, reported experimental results using mid-IR time-resolved pump-probe spectroscopy. In their experiments, they were able to isolate the contributions introduced through ions by temporally[57, 58] or spectrally[49] resolving the signals. Their main results can be summarized with the help of Figures 5.1 and 5.2. By performing pump-probe spectroscopy at the magic angle, the vibrational lifetime of the OH stretch vibrations in isotopically diluted (HDO:D_2O) salt solutions was found to consist of two time constants. The fast time constant is similar to what is found in HDO:D_2O bulk water ($T_1 = 800\,\text{fs}$ [30]) and is independent of ion-type and ion concentration. It must therefore correspond to OH groups that form a hydrogen bond with another water molecule OH$\cdots$O, which includes water molecules solvating a cation like in Figure 5.2. The second, slow component is dependent on anion-type and anion concentration, yet independent of cations. This leads to the conclusion that it is associated with OH groups that solvate the anion OH$\cdots Y^-$ like in Figure 5.1. Bakker et al. isolated the orientational correlation time and found like in their previous experiments two distinct species: One that is independent of the salt and its concentration, and has an orientational correlation time that one would expect to find in the bulk (2.5 ps - bOD in HDO:H_2O) and one with a much slower orientational correlation time (7.6 ps) that belongs to the first solvation shell around the anion.[49] It appears that the first solvation shell around an anion is “rigid” on a picosecond scale. Modeling this system with the Stokes-Einstein equation, which relates the diffusion of spherical particles through a liquid to the liquid’s viscosity, explains the observed increased viscosity of aqueous salt solutions.[59]

The MD simulations based on the molecular jump mechanism by Laage and Hynes show how water molecules can depart from a semi-rigid solvation shell.[8] In their research they studied water

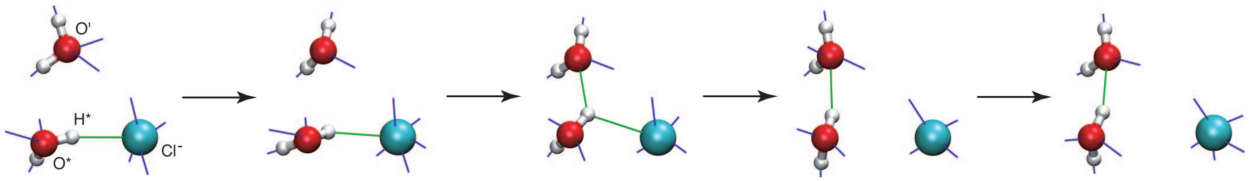

Figure 5.4: Schematic representation by Laage et al.[8] of the molecular jump mechanism in a solvation shell around a chloride atom showing the "departure" of a water molecule from the solvation shell. (Blue sticks: H-bonds involving molecules in the surrounding solution. Green sticks: H-bonds directly involved in reorientation.) The sequence starts with overcoordination of the chloride ion and an undercoordinated water molecule in the second solvation shell. This is followed by a bifurcation and abrupt switch of the hydrogen bond, followed by the departure of the water molecules from the first solvation shell.

molecules surrounding a Cl^- ion, pictured in figure 5.4. Fluctuations in the hydrogen-bond network preceding the departure of a water molecule from the anion lead to an overcoordinated anion and an undercoordinated water molecule in the second hydration shell. These initial conditions facilitate an angular jump motion of the OH bond originally interacting with the anion to the undercoordinated second shell water molecule; bifurcating briefly like in the case of bulk neat water. Furthermore, certain ion combinations have an effect on the structure and dynamics of water beyond the first solvation shell[60, 61, 62]. Bakker's group found that this is the result of strong cooperativity of water molecules located between anions and cations[7]. This effect seems to only arise if the involved anions and cations are strongly hydrated (Figure 5.3-C), for example in the case of $MgSO_4$ resulting from the double charge of the individual solvated ions (Mg^{2+} and SO_4^{2-}). If one of them is weakly hydrated, the picture of a semi-rigid hydration shell around the strongly hydrated ion seems to be a more accurate picture.

5.2 Previous research on interfaces of salt solutions

At the water/air interface, research experienced a large step forward in recent times. Macroscopically measuring and modeling the surface tension was a cornerstone of investigating the composition of interfaces for a long time. Using the "Gibbs-Duhem" or "Gibbs absorption" equation in combination with surface tension measurements, it was thought for most of the 20th century

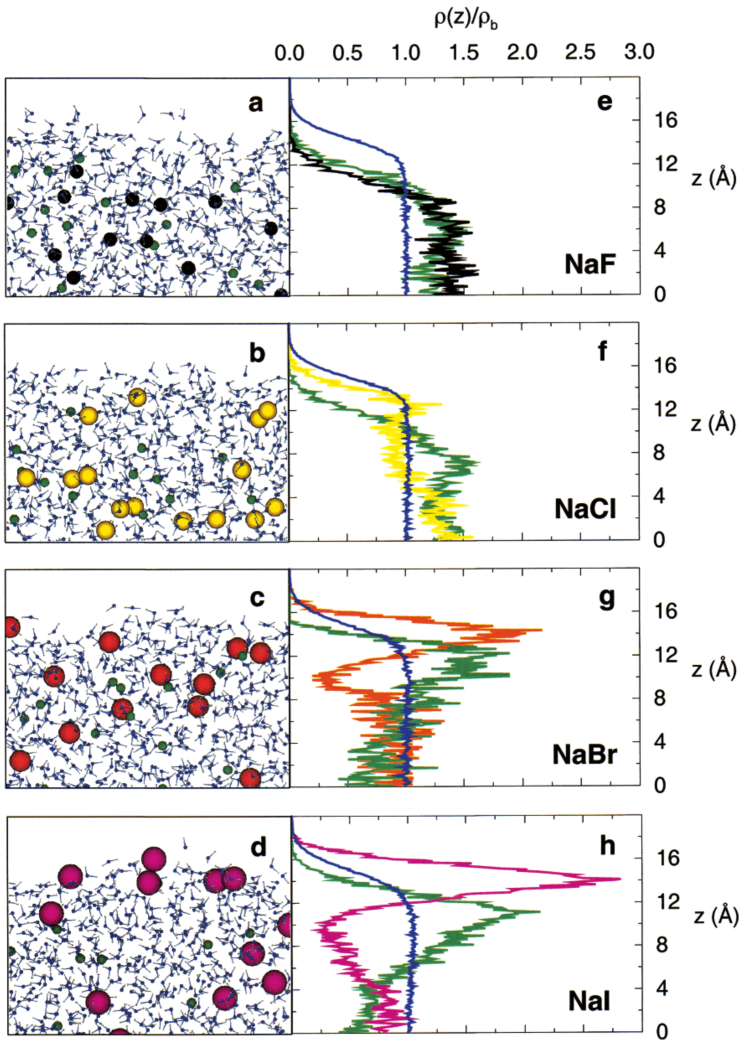

Figure 5.5: MD simulations from Jungwirth and Tobias show number densities of water, oxygen atoms, and ions, normalized by the bulk water density ρ_b, for several 1.2 M salt solutions.[9]

that the interfacial region is depleted of inorganic ions. This method involved describing ions as point particles which can be a good approximation for small, non-polarizable ions such as fluoride. However, these simplifications only hold for a very limited range of solutes and do not reflect the microscopic polarizability of ions or water molecules. Wilson et al. and Benjamin pioneered the molecular dynamics simulation of single anions in a water slab of several hundred water molecules, approximating the water/air interface. Their results, after 21 days of CPU time, pictured ions to be more energetically favored in the bulk which would support the hypothesis of a surface devoid of ions.[63] Nonetheless, the researchers realized that their simulations "do not provide a faithful

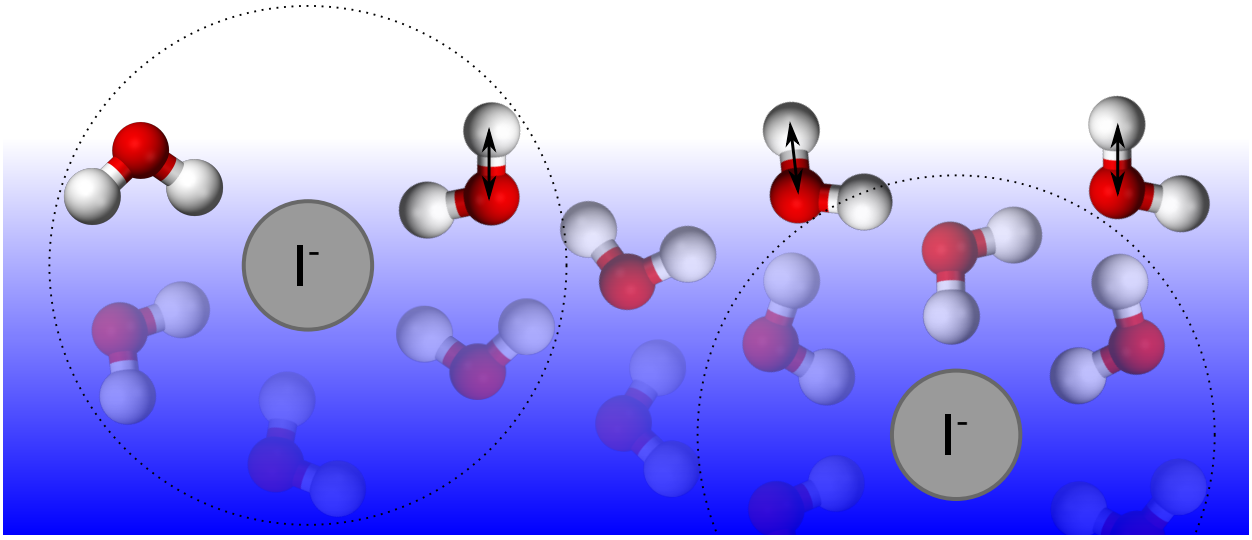

Figure 5.6: Schematic illustration of dangling OH bonds at the water/air interface showing dOH groups within the first (illustrated by the dashed circle) and second solvation shell of a iodine ion.

description of ions at the water interface" but should only be helpful to create better, more physical models.[64] Only recently, more accurate simulations and better spectroscopic methods have challenged the view that the surface is devoid of ions by collecting evidence that some inorganic ions exhibit a surface propensity.

In the early 1990s, photoelectron spectroscopy measurements by Markovich et al.[65] of $I^- \cdot (CO_2)_n$ ($n = 1, \ldots, 7$) clusters attracted the attention of researchers and motivated a series of molecular dynamics studies of clusters. Experimental limitations still prevented a thorough investigation of water clusters, but a few years later Markovich et al. expanded their initial study to water clusters with Cl^-, Br^-, and I^-.[66] At the time, molecular dynamics simulations were limited to studying clusters involving single anions and initially few, later several hundreds of, water molecules.[67, 68, 69, 70, 71, 72, 73, 74, 75, 76, 77, 78] Only molecular dynamic simulations that used polarizable force fields were able to reproduce the electron binding energies experimentally obtained with photoelectron spectroscopy. These simulations contradicted the initial hypothesis of a fully solvated ion and showed the larger anions with a stable coordination number of 3-5 water molecules at the surface of water clusters even with hundreds of water molecules. They established

the consensus for ions in water clusters: Hard, non-polarizable ions such as F^- or Na^+ that can be approximated as point charges are, within the classic Onsager-Samaras model[51], repelled from the surface by image charges. The comparison of polarizable and non-polarizable force fields suggests that the polarizability of ions is the driving force for the surface propensity of polarizable anions like Cl^-, Br^-, and I^-. In addition, the increasing polarizability of Cl^-, Br^-, and I^- manifests in an increasing surface propensity. The first indirect experimental evidence that bromide has a larger surface propensity than chloride was obtained by exposing a NaCl crystal doped with NaBr to water vapor. After redrying the surface was examined with X-ray photoelectron spectroscopy and scanning electron microscopy revealing substantial surface enrichment of Br^-.[79] MD simulations in aqueous solutions supported this conclusion.[80]

The question if this consensus would hold for larger clusters or for extended interfaces is unavoidable. Rather surprisingly, experimental evidence for the surface propensity of anions at extended interfaces arose by investigation of the phenomenon of ozone depletion at polar sunrise: A rapid drop in ozone levels and rise of chlorine gas levels is observed in the Arctic (Antarctic) when the sun rises for the first time at the spring (fall) equinox after months of darkness. Kinetic models of this phenomenon only considering bulk-phase reactions could not reproduce the recorded on-site measurements. They could only be reproduced satisfactorily by including anions at the water surface, which enables direct reactions at the interface. Since the surface propensity emerges upon including polarizability of ions and water molecules during simulations of clusters up to quasi-bulk dimensions, this suggests that bulk water might be similar to water clusters in terms of ion surface propensity.[81, 82]

Refined MD simulations paint an increasingly more detailed picture: Br^- and I^- anion concentrations at the interface are found to exceed their average bulk concentrations. For F^-, which is repelled from the surface, surface OH bonds prefer to point towards the F^- ions in the bulk. The opposite is true for NaBr and NaI solutions, where OH groups point to towards the ions which are enriched at the surface; the OH groups are therefore parallel to the surface. In the case of a NaCl solution, intermediate angles are observed.[9] If an aqueous solution contains two anions

that are attracted to the interface, at low bulk ion concentration both anions can be found at the interface. If the bulk concentration is high enough, the ion that experiences the higher surface propensity will take over the surface and replace "weaker" competing ion. In the case of a solution with high concentrations of Cl and Br anions, the Br^- will replace almost all Cl anions at the surface.[80] Another effect that manifests at high bulk salt concentrations is the increased ion pair formation in the bulk and at the interface. Ion pair formation increases from merely 5% at low concentration to 75% in the bulk and to 55% at the interface of a saturated NaCl solution.[83] This mechanism explains the 20% drop in hydration numbers at high salt concentrations compared to low salt concentrations.

With the establishment of SFG spectroscopy as a practical technique for surface studies, experiments could finally move forward. Using 1.7 M salt solutions and static SFG, the interfacial region was probed for spectral changes that indicated structural differences compared to neat water.[84] Fully coordinated interfacial bOH groups at $3325\,cm^{-1}$ experience a red shift by $40\,cm^{-1}$ due to engaging in stronger hydrogen bonds with small non-polarizable ions (e.g. F^-) while a blue shift of $35\,cm^{-1}$ is observed due to fully coordinated interfacial bOH groups engaging in weaker hydrogen bonds upon addition of large polarizable ions (Cl^-, Br^-, I^-). These shifts are indicative of the presence of ions in the vicinity of the surface. The same shifts are well documented for bOH in bulk solutions[85, 86, 87]. At the same salt concentration (1.7 M), only I^-, the halide with the largest surface propensity, affects tangential OH groups associated with water molecules with a dangling OH which are directly at the interface. The blue shift from $3450\,cm^{-1}$ by up to $50\,cm^{-1}$ of the feature associated with the tangential OH is experimental evidence that iodide anions are directly at the interface. At higher salt concentrations, closer to saturation, other studies have observed a blue shift for all the halides exhibiting a surface propensity.[86, 58, 88, 89] A similar SFG study used higher salt concentrations and was able to detect signs of a weakened hydrogen bond network in the interfacial region for NaBr and NaI solutions. No significant difference was detected while using NaF and NaCl solutions. These differences did not manifest themselves as blue shifts, but rather as increased intensity of the tangential bOH feature. The increase in intensity at that frequency

was attributed to an increase in depth of the interfacial region, and a corresponding increase in the number of water molecules contributing to the SFG signal.[90]

In 2005, Archontis et al. used MD simulations to answer the question of what exact interplay of interactions causes an ion to be attracted to the surface.[91] The Coulomb interactions between the permanent charges of I^- ions and the permanent dipole moment of H_2O would favor iodide ions in the bulk. However, the interaction of induced charges stabilizes the iodide ions at the interface. The most relevant contribution to this surface stabilization originates from dipole-dipole interactions between the induced dipole in the iodide and the permanent dipole of water molecules. The shorter range of dipole-dipole interactions supports the conclusion that they mainly originate among the ion and its first solvation shell. Archontis et al. also added to the accumulating research showing evidence, theoretically[92, 9, 80, 93] and experimentally[90, 94], for the existence of a double layer at the surface: The high density of ions with strong surface propensity causes ions of the opposite charge to accumulate just below them.

Further advances were made more recently by using phase-sensitive SFG spectroscopy. The relative surface propensity follows a Hofmeister series from the ion expressing the most surface propensity to the one expressing the least surface propensity: I^-, NO_3^-, NH_4^+, Cl^-, K^+, Na^+, and SO_4^{2-}.[95, 96] In bulk, introducing salt into neat water leads to structural changes of the hydrogen bond network caused by solvation shells or ion cooperativity. These interruptions also bring changes in dynamics. Since structural changes are also documented at the interface it is a reasonable assumption that the dynamics might differ from the neat water interface as well. To investigate this hypothesis we used three different salts: NaCl, NaI, and $MgSO_4$. NaCl has been identified as a salt introducing little change in structure and dynamics compared to other salts. Therefore, an experiment using NaCl is expected to yield results that are closest to neat water. With the strong surface propensity of I^-, NaI should be an ideal candidate to observe changes of dynamics at the interface that might be caused by the formation of solvation shells and the presence of iodide anions directly at the surface. To investigate the influence of cooperativity effects that are reaching further than the first solvation shell on the surface dynamics an aqueous solution with $MgSO_4$ is used.

	[ps]	H_2O	3M NaCl	3M NaI	3M $MgSO_4$
τ_{fast}	p-pump	1.34 ± 0.03	1.41 ± 0.01	1.10 ± 0.04	1.35 ± 0.03
	s-pump	1.55 ± 0.04	1.83 ± 0.03	1.76 ± 0.08	1.56 ± 0.03
τ_{slow}	shared	15 ± 2	31 ± 3	11 ± 1	20 ± 1
$\bar{\beta}'$	$T_1(t_0 = 2.0)$	1.46 ± 0.06	1.43 ± 0.03	1.60 ± 0.08	1.54 ± 0.07
	$T_1(t_0 = 0.6)$	1.42 ± 0.02	1.41 ± 0.01	1.32 ± 0.03	1.45 ± 0.02
	$\tau_{\bar{\beta}slow}$	15*	31*	11*	20*
$\Delta\beta$	$\tau_{\Delta\beta}$	0.74 ± 0.05	0.84 ± 0.03	0.56 ± 0.05	0.60 ± 0.08
	$\tau_{\Delta\beta slow}$	-	-	11*	-

Table 5.1: Summary of all time constants. * = fixed parameter.

5.3 Rotational dynamics of aqueous salt solutions at an extended hydrophobic interface

For the experiments using salt solutions the same procedure and analysis, as in the neat water case, were used. The calculation of rates/decay times is analogous to the neat water case and is not explicitly repeated in this section. The results of the measurements and fits are summarized in table 5.1. A more detailed discussion follows in the next section.

5.3.1 3M NaCl solution

NaCl is the salt where the least difference on rotational dynamics at the interface is expected due to it being the one having the least surface propensity. Like in the neat water case, a global fit with a double exponential (equation 4.1) is performed on the normalized p- and s-pump intensity traces with individual fast decay constants and a global slow decay constant. Significant deviations from the neat water case are observed in both fast time constants and the global slow constant and are listed in table 5.1. Yet, when continuing this analysis like in the neat water case the results (table 5.1) are similar: The fast time constants obtained from fitting $\bar{\beta}'$ starting at 0.7 ps and 2.1 ps are compatible with each other and are compatible with their equivalents in the neat water case which indicates that there is little leaking of orientational dynamics into $\bar{\beta}'$. Proceeding with the

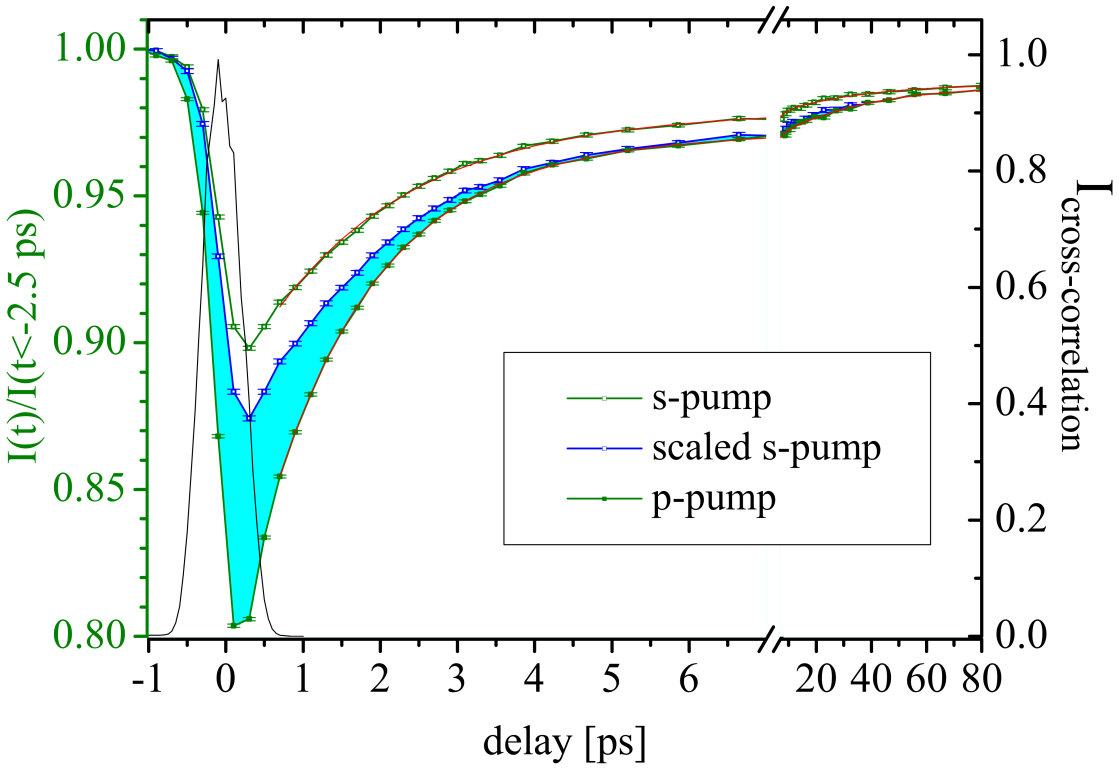

Figure 5.7: NaCl normalized SFG intensities

analysis like in the neat water case, the single exponential fit of $\Delta\beta$ yields an observed time constant of 0.84 ± 0.03 ps, which is slightly slower than in neat water (0.74 ± 0.05 ps) and, although not compatible within one standard deviation, is well within two standard deviations of the result for neat water. The final forward jump time for the dOH groups of a 3M NaCl solution is $1.61^{+0.04}_{-0.20}$ ps, not significantly different from that of neat water. For the in-plane orientational time scale, the limits of our experiment become apparent: Presumably, limitations caused by signal-to-noise and the double-differential measurement lead to an unphysical value for k_{ip} in the case of NaCl.

5.3.2 3M NaI solution

Iodide has been shown to have one of the strongest surface propensities among common ions and should be a good candidate for producing solvation shells at the surface. The 3M NaI solution is, in fact, the case where the largest deviation from neat water is measured. Figure 5.9 show the fit of the p- and s-pump traces with a double exponential and shared slow time constant (table 5.1). It reveals

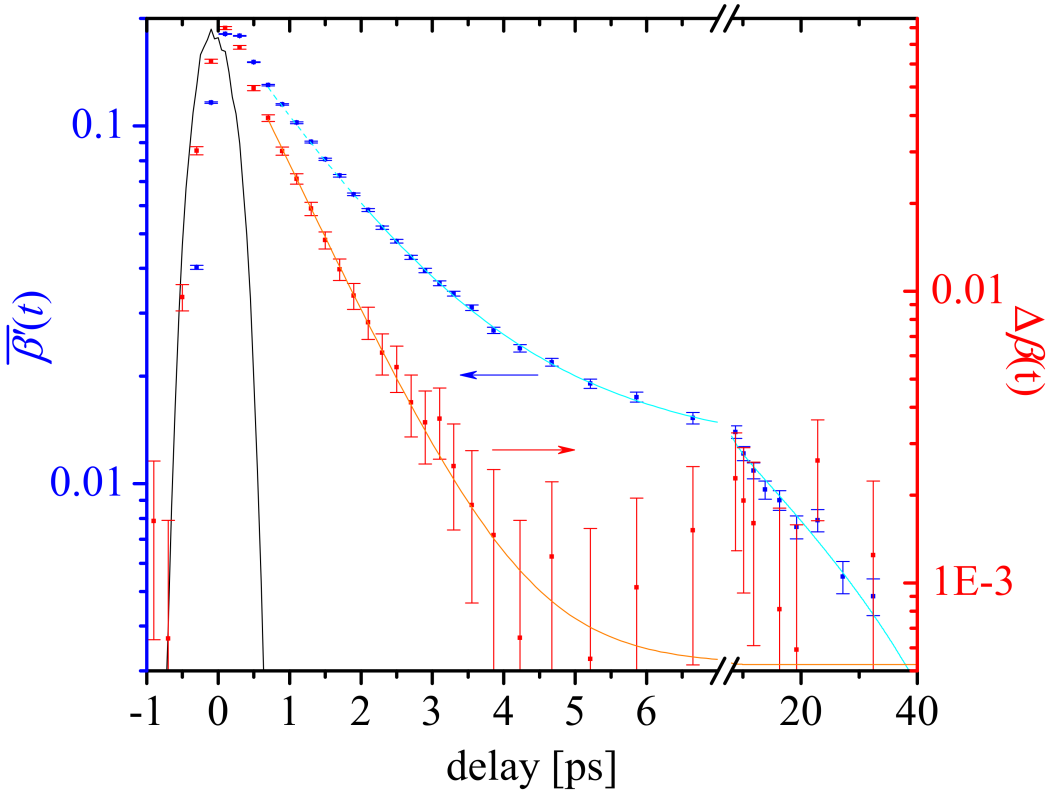

Figure 5.8: NaCl difference and average of bleach

	3M NaCl	
	k [ps^{-1}]	τ [ps]
fit parameters experimental values		
$\bar{\beta}'$	0.699 ± 0.015	1.43 ± 0.03
$\Delta\beta$	1.190 ± 0.043	0.84 ± 0.03
IET (H_2O)	$0.077^{+0.007}_{-0.077}$	$13.0^{+\infty}_{-1.2}$
calculated values		
jump^F	$0.622^{+0.078}_{-0.016}$	$1.61^{+0.04}_{-0.20}$
ip	$-0.13^{+0.09}_{-0.16}$	$-7.6^{+9.45}_{-5.45}$

Table 5.2: Summary table of experimentally obtained and calculated values for NaCl.

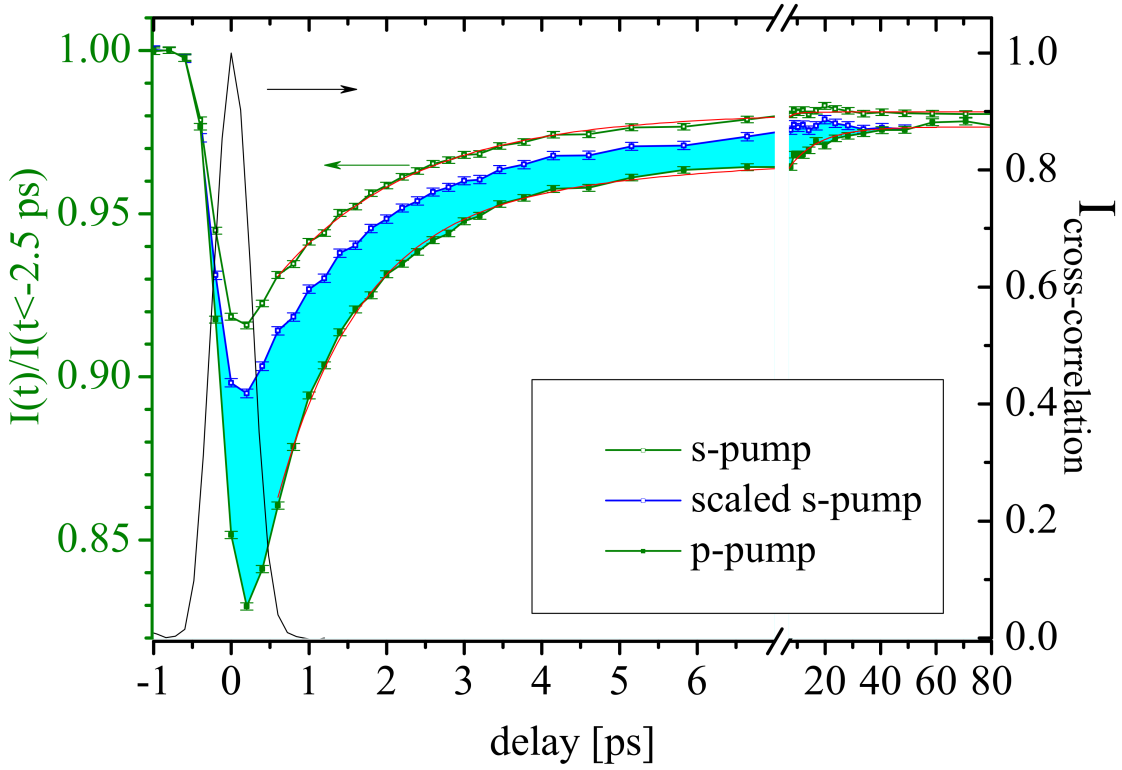

Figure 5.9: NaI normalized SFG intensities

differences compared to neat water. The fast time constant of the p-pump trace (1.10 ± 0.04 ps) is significantly faster than the one measured for neat water (1.34 ± 0.03 ps). However, the fast time constant of the s-pump trace (1.76 ± 0.08 ps) is compatible with neat water (1.55 ± 0.04 ps) within two standard deviations. Furthermore, the slow time constant (11.1 ± 1.4 ps) is 25% faster than but still within two standard deviations of the neat water case (15 ± 2 ps). The fitting of $\bar{\beta}'$ in figure 5.10 yields time constants listed in table 5.1 that are compatible with neat water to within two standard deviations. More importantly, the two fast time constants from starting the fit of $\bar{\beta}'$ at $t_0 = 0.6$ ps and $t_0 = 2.0$ ps are only compatible with each other within three standard deviations, indicating that a significant amount of orientational dynamics might have "leaked" into $\bar{\beta}'$. Looking at $\Delta\beta$ it also becomes apparent that there is "leaking" of the slow time constant from $\bar{\beta}'$. A fit with a single exponential is therefore unreasonable. Instead, a fit with a double exponential including the slow time constant from $\bar{\beta}'$ produces the fastest time constant (0.56 ± 0.05 ps) of the salts used, but is still within two standard deviations of neat water (0.74 ± 0.05 ps). An acceleration of dynamics by

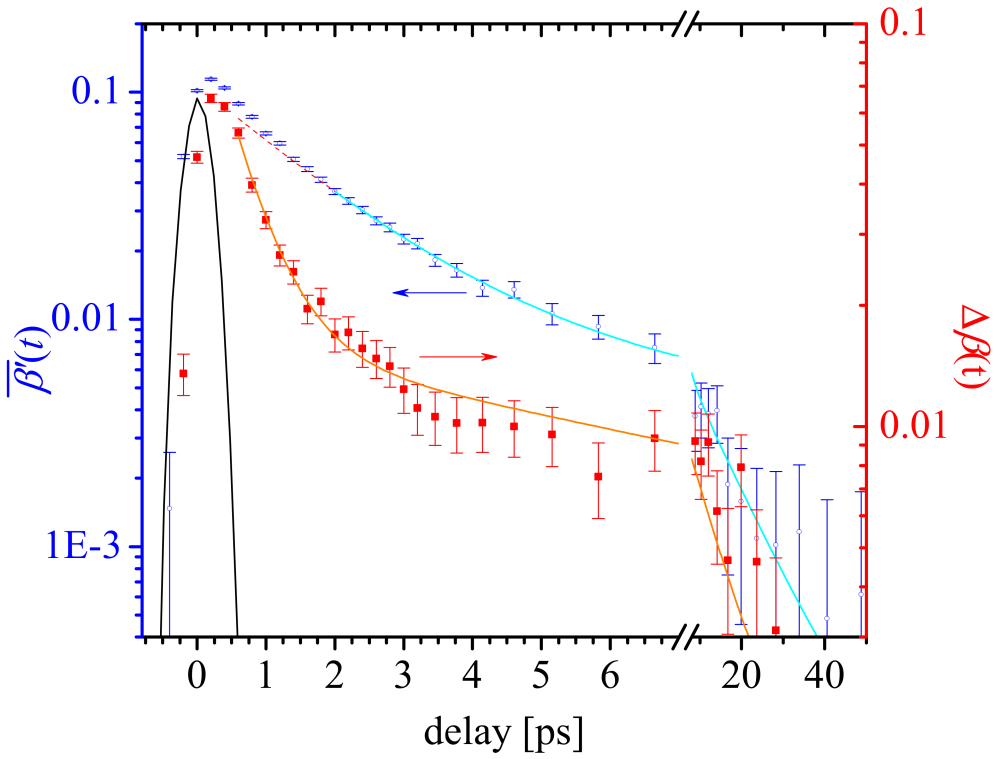

Figure 5.10: NaI difference and average of bleach

anions is counterintuitive because in bulk a slow down of dynamics is observed. The dangling OH forward jump time is, at $1.82^{+0.11}_{-0.28}$ ps, still compatible with the neat water case.

Because of the leakage of dynamics among $\bar{\beta}'$ and $\Delta\beta$, it was reasonable to assume that $\bar{\beta}'$ might follow a triple exponential decay instead of just a double exponential. The new third exponential would correspond to the short dynamics from $k_{\Delta\beta}$ that leaked in. Nonetheless, the fit came back with a negligible amplitude associated with $k_{\Delta\beta}$ and the idea of using a triple exponential was discarded. The in-plane orientational time scale is with $1.63^{+0.61}_{-0.50}$ ps shorter than expected. It is important to note though, that the reliability of this result might be affected by the leaking of time constants as discussed above.

5.3.3 $MgSO_4$ solution

$MgSO_4$ is expected to display a cooperativity effect between the ions which, in bulk, leads to a slow down of reorientational dynamics affecting water molecules beyond the first solvation shell: The

	3M NaI	
	k [ps^{-1}]	τ [ps]
experimental values		
$\bar{\beta}'$	0.625 ± 0.031	1.60 ± 0.08
$\Delta\beta$	1.79 ± 0.16	0.56 ± 0.05
IET (H_2O)	$0.077^{+0.007}_{-0.077}$	$13.0^{+\infty}_{-1.2}$
calculated values		
jump^F	$0.548^{+0.083}_{-0.032}$	$1.82^{+0.11}_{-0.28}$
ip	$0.61^{+0.19}_{-0.23}$	$1.63^{+0.61}_{-0.50}$

Table 5.3: Summary table of experimentally obtained and calculated values for NaI.

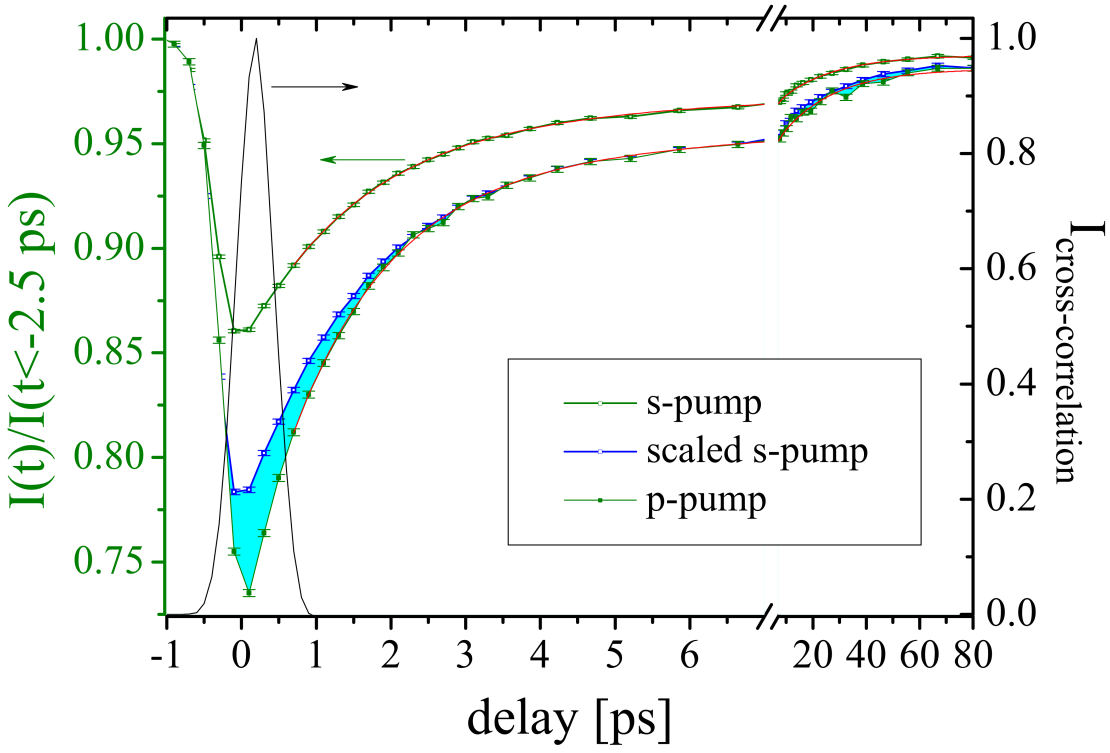

Figure 5.11: $MgSO_4$ normalized SFG intensities

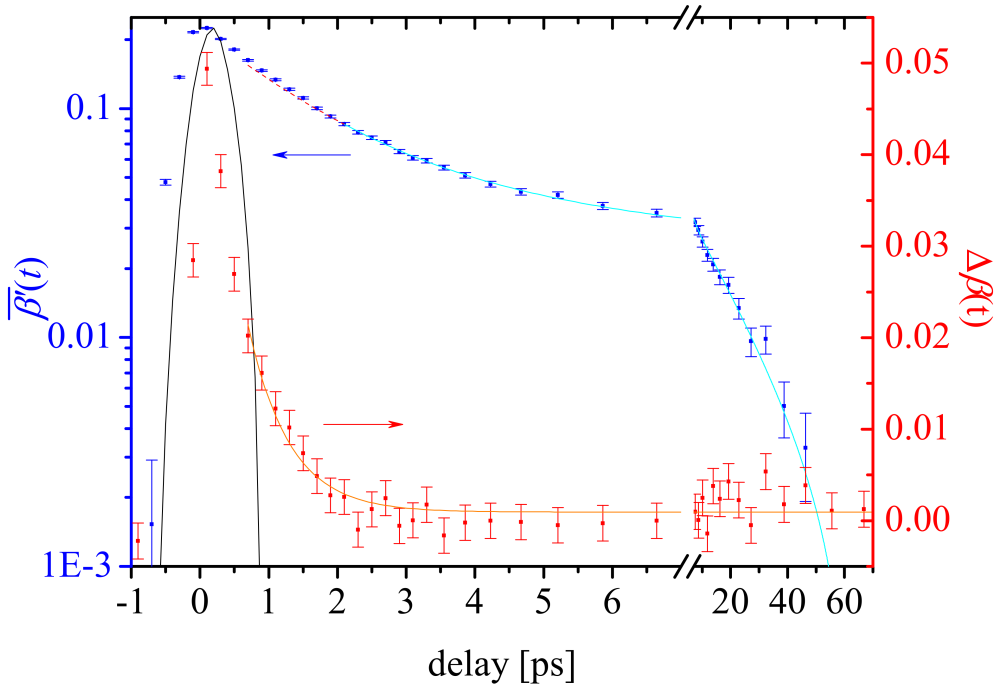

Figure 5.12: $MgSO_4$ difference and average of bleach

hydrogen-bond network between the ions is locked in multiple directions. However, the surface propensities of SO_4^{2-} and Mg^{2+} are expected to be lower compared to the previous salts. Figure 5.11 shows the p- and s-pump traces that look qualitatively very similar to the neat water case. Double exponential fits with a common slow time constant yield fast time constants that are compatible with the neat water fit (table 5.1). The slow time constant obtained for $MgSO_4$ (20 ± 1 ps) is only compatible with neat water (15 ± 2 ps) within two standard deviations. Examining the average of the p- and s-pump bleach $\bar{\beta}'$ with a double exponential fit using again the slow constant from before, the fast time constants agree again with the neat water experiment. Finally, the fit of $\Delta\beta$ with a single exponential yields a time constant (0.60 ± 0.08 ps) that is just barely incompatible within one standard deviation compared to neat water (0.74 ± 0.05 ps), but well compatible within two. The dangling OH forward jump time is, at $1.75^{+0.09}_{-0.25}$ ps, compatible with the neat water case. Interestingly, the in-plane orientational time scale is with $2.2^{+1.4}_{-1.2}$ ps compatible with the bulk orientational time scale of 3.3 ps.[10]. Even though the result is lower than expected, it is not in a completely unphysical range. Unfortunately, the outcome for the in-plane orientational time

	3M $MgSO_4$	
	k [ps^{-1}]	τ [ps]
experimental values		
$\bar{\beta}'$	0.649 ± 0.030	1.54 ± 0.07
$\Delta\beta$	1.67 ± 0.22	0.60 ± 0.08
IET (H_2O)	$0.077^{+0.007}_{-0.077}$	$13.0^{+\infty}_{-1.2}$
calculated values		
jump^F	$0.572^{+0.082}_{-0.030}$	$1.75^{+0.09}_{-0.25}$
ip	$0.44^{+0.24}_{-0.28}$	$2.2^{+1.4}_{-1.2}$

Table 5.4: Summary table of experimentally obtained and calculated values for $MgSO_4$.

scales in the previous two cases involving salt solutions indicates that this result might also not be a reliable quantity.

5.4 Summary and discussion

Within these experiments, we found no significant evidence for an effect of salts on the orientational dynamics of the dOH. Table 5.5 provides a summary of the results. All three tested 3M salt solutions (NaCl, NaI, $MgSO_4$) yielded forward jump orientation times that are compatible with neat water.

If these results hold true, this would indicate that anions like I^- which have a high surface propensity and are know to form solvation shells have little influence on the forward jump motion of the dOH. This could mean that the bulk concentration of NaI was insufficient and caused only few dOH groups to be in the range of influence of iodide ions at the interface and the experiment was not

[ps]	H_2O	3M NaCl	3M NaI	3M $MgSO_4$
τ_{IET}	$13^{+\infty}_{-1.24}$	-	-	-
τ^F_{jump}	$1.64^{+0.08}_{-0.22}$	$1.61^{+0.04}_{-0.20}$	$1.82^{+0.11}_{-0.28}$	$1.75^{+0.09}_{-0.25}$
τ_{ip}	$17^{+\infty}_{-12}$	N/A	$1.63^{+0.61}_{-0.50}$	$2.2^{+1.4}_{-1.2}$

Table 5.5: Summary of experimentally obtained constants.

sensitive to their change in reorientation, or that very little dOH bonds exist in the vicinity of an iodide ion. For example, the partially positively charged hydrogen of dOH bonds rotate toward an anion and could form a hydrogen bond with the ion. Now being a bOH, it would therefore be out of our detection range.

Furthermore, cooperativity effects beyond the first solvation shell from salts like $MgSO_4$ do not seem to influence the τ^F_{jump} either. In this case, the explanation could be that due to the relatively low surface propensity of Mg^{2+} and SO_4^{2-} the "locked in" water molecules due to the cooperativity effect might not extend to the interface and would therefore not be detectable.

It is notable that the slow dynamics of the salt solutions deviate from the neat water values, especially in the case of the 3M NaCl solution. This could be due to several potential issues. First, a systematic experimental error, such as a slight misalignment of pump path down the delay stage, could cause effects at long delays that are not noticeable at short delays due to the higher signal-to-noise ratio. Second, the proximity of ions at or near the surface could lead to formation of hydrogen bonds between ions and water molecules. Due to the nature of the salts that were used, these ion-water hydrogen bonds would be weaker than hydrogen bonds between water molecules. The ion-water hydrogen bond would be blue-shifted and would have less spectral overlap with the surrounding bOH which would result in a slow down of dynamics that are related to transient heating.

As discussed earlier, the reliability of the in-plane orientational time scale results is questionable. This might simply be due to the double-differential nature of the approach in this dissertation: Since pump-probe measurements are differential measurements, calculating the difference of such measurements to obtain quantities like the in-plane orientational time scale has to be viewed with caution since signal-to-noise issues are increasingly influential. The results that yield physical values should be backed up by further simulations or measurements.

CHAPTER 6

SUMMARY AND OUTLOOK

6.1 Orientational dynamics of neat water at hydrophobic interfaces

At the interface between neat water and an extended hydrophobic surface, realized by a hydrophobic OTS SAM, the out-of-plane orientational dynamics of dangling OH groups was measured to occur on a $1.64^{+0.08}_{-0.22}$ ps timescale. The measurement was performed in a total internal reflection geometry that yields high signal-to-noise and simplifies the analysis by heavily weighting the $\chi^{(2)}_{zzz}$ contribution to the second order optical susceptibility. Our result for the out-of-plane orientational dynamics of dangling OH groups at a hydrophobic interface is twice as fast as the orientational dynamics of water in bulk and about 50% slower than the out-of-plane orientational dynamics at the water/air interface. Our interpretation of the pump-probe SFG data was confirmed with MD simulations by our collaborators Guillaume Stirnemann and Damien Laage. Their MD simulations suggest that the slower out-of-plane orientational dynamics at the hydrophobic interface is a result of the dangling OH groups being slightly more stabilized by the hydrophobic medium. This interpretation aligns with the $20\,\mathrm{cm}^{-1}$ redshift observed in stativ SFG spectra of the dangling OH peak at the water/hydrophobic surface compared to water/air.

6.2 Orientational dynamics of salt solutions at hydrophobic interfaces

Upon adding 3M of each of the salts NaCl, NaI, and $MgSO_4$ to neat water, measurements of the out-of-plane orientational dynamics of the dangling OH groups were repeated. Despite the fact that these salts have shown surface propensity and evidence in the literature for a slow down in orientational dynamics in bulk salt solutions, no significant change of the out-of-plane orientational dynamics of the dangling OH groups was detected. The time scales for out-of-plane reorientation for NaCl, NaI, and $MgSO_4$ were measured to be $1.61^{+0.04}_{-0.20}$ ps, $1.82^{+0.11}_{-0.28}$ ps, and $1.75^{+0.09}_{-0.25}$ ps, respectively. In principle, the potential changes could be beyond our ability of detection and might

be detectable at higher salt concentrations. If the salt concentration was appropriate, for anions like I^- that display a high surface propensity and form solvation shells at the interface, this would indicate that a solvation shell at the interface might not have any slowing effects even if water molecules with dOH are in the vicinity or even part of the first solvation shell. In the case of $MgSO_4$, the surface propensity of its ions is considerably lower than for iodide. A reasonable explanation for not being to detect a difference for $MgSO_4$ could be that the cooperativity effects between $Mg2+$ and SO_4^{2-} might not extend to the uppermost portion of the interface. The dOH would therefore be unaffected.

6.3 Outlook

The measurement of the dynamics of the dOH stretch vibration at the interface with a hydrophobic medium ensures the hightest degree of surface specificity. By tuning the infrared to the bonded OH stretch vibration, the dynamics of bonded OH groups in the immediate vicinity of the interface can be examined. In addition, many water interfaces involve hydrophilic substances, where no dangling OH groups exist. In that case, a measurement where the pump and probe IR pulses are resonant with the bonded OH stretch vibration would enable measuring the dynamics directly at the water/hydrophilic interface. Finally, measurements resonant to the bonded OH stretch vibration might help with the detection of changes in interfacial dynamics of salt solutions. Since water molecules participate in solvation shells around ions, and thereby form hydrogen bonds with anions, being able to specifically probe those hydrogen bonds would be of advantage.

APPENDIX

A.1 Calculation of error bars in figures

For a given pump-probe delay t, the CCD detects N_{ij} number of photons in pixel ij: N_{ij} with an associated uncertainty $\sigma(N_{ij}) = \sqrt{N_{ij}}$. Summation over a certain pixel range yields the intensity: $s_j = \sum_i N_{ij}$ with an uncertainty of

$$\sigma(s_j) = \sqrt{\sigma(N_{1j})^2 + (\sigma(N_{2j})^2 + \ldots} = \sqrt{N_{1j} + N_{2j} + \ldots} = \sqrt{s_j}. \tag{1}$$

The pixel range is measured n times and averaged to $I = \frac{1}{n}\sum_{j=1}^{n} s_j$ with the uncertainty

$$\sigma(I) = \frac{1}{n}\sqrt{\sigma(s_1)^2 + \sigma(s_1)^2) + \ldots} = \frac{1}{n}\sqrt{s_1 + s_2 + \ldots} = \frac{1}{n}\sqrt{n \times I} = \sqrt{\frac{I}{n}} \tag{2}$$

In figure 4.2 the normalized quantity $I^{norm} = \frac{I_{on}}{I_{off}}$ is plotted where

$$\frac{\sigma(I^{norm})}{I^{norm}} = \sqrt{\left(\frac{\sigma(I_{on})}{I_{on}}\right)^2 + \left(\frac{\sigma(I_{off})}{I_{off}}\right)^2} = \sqrt{\frac{1}{n \times I_{on}} + \frac{1}{n \times I_{off}}} \tag{3}$$

$$\sigma(I^{norm}) = I^{norm} \times \frac{1}{\sqrt{n}}\sqrt{\frac{1}{I_{on}} + \frac{1}{I_{off}}} = \frac{1}{\sqrt{n}}\sqrt{\frac{I_{on}}{I_{off}^2} + \frac{I_{on}^2}{I_{off}^3}} \tag{4}$$

determines the size of the error bars, which are the same size for the bleach $\beta = 1 - I^{norm}$:

$$\sigma(\beta) = \sigma(I^{norm}) = \frac{1}{\sqrt{n}}\sqrt{\frac{I_{on}}{I_{off}^2} + \frac{I_{on}^2}{I_{off}^3}} \tag{5}$$

The error bars of the scaled s-pump trace is simply the original s-pump trace error bars multiplied by the scaling factor:

$$\sigma(I^{norm}_{s,scaled}) = \sigma(\beta_{s,scaled}) = \frac{\beta_p(t \gg k_{or}^{-1})}{\beta_s(t \gg k_{or}^{-1})} \times \sigma(\beta_s) \tag{6}$$

Finally, the error bars for $\Delta\beta = \beta_p - \beta_s$ and $\bar{\beta} = \frac{1}{2}(\beta_p + \beta_s)$, plotted in figure 4.3, are:

$$\sigma(\Delta\beta) = \sqrt{\sigma(\beta_p)^2 + \sigma(\beta_{s,scaled})^2} \tag{7}$$

$$\sigma(\bar{\beta}) = \frac{1}{2}\sqrt{\sigma(\beta_p)^2 + \sigma(\beta_{s,scaled})^2} \tag{8}$$

BIBLIOGRAPHY

BIBLIOGRAPHY

[1] D. Laage and J. T. Hynes. On the molecular mechanism of water reorientation. *The Journal of Physical Chemistry B*, 112:14230–14242, 2008.

[2] C. S. Tian and Y. R. Shen. Structure and charging of hydrophobic material/water interfaces studied by phase-sensitive sum-frequency vibrational spectroscopy. *Proceedings of the National Academy of Sciences*, 106:15148–15153, 2009.

[3] H.-K. Nienhuys and M. Bonn. Measuring molecular reorientation at liquid surfaces with time-resolved sum-frequency spectroscopy: A theoretical framework. *The Journal of Physical Chemistry B*, 113:7564–7573, 2009.

[4] S. Xiao, F. Figge, G. Stirnemann, D. Laage, and J. A. McGuire. Orientational dynamics of water at an extended hydrophobic interface. *Journal of the American Chemical Society*, 138:5551–5560, 2016.

[5] Wikipedia. Octadecyltrichlorosilane - wikipedia, the free encyclopedia. `https://en.wikipedia.org/wiki/Octadecyltrichlorosilane`, 2016. [Online; accessed 23-February-2016].

[6] G. Lamour, A. Hamraoui, A. Buvailo, Y. Xing, S. Keuleyan, V. Prakash, A. Eftekhari-Bafrooei, and E. Borguet. Contact angle measurements using a simplified experimental setup. *Journal of Chemical Education*, 87:1403–1407, 2010.

[7] K. J. Tielrooij, N. Garcia-Araez, M. Bonn, and H. J. Bakker. Cooperativity in ion hydration. *Science*, 328:1006–1009, 2010.

[8] D. Laage and J. T. Hynes. Reorientional dynamics of water molecules in anionic hydration shells. *Proceedings of the National Academy of Sciences*, 104:11167–11172, 2007.

[9] P. Jungwirth and D. J. Tobias. Molecular structure of salt solutions: A new view of the interface with implications for heterogeneous atmospheric chemistry. *The Journal of Physical Chemistry B*, 105:10468–10472, 2001.

[10] G. Stirnemann, P. J. Rossky, J. T. Hynes, and D. Laage. Water reorientation, hydrogen-bond dynamics and 2D-IR spectroscopy next to an extended hydrophobic surface. *Faraday Discussions*, 146:263–281, 2010.

[11] D. Laage and J. T. Hynes. A molecular jump mechanism of water reorientation. *Science*, 311:832–835, 2006.

[12] H. Graener, G. Seifert, and A. Laubereau. Direct observation of rotational relaxation times by time-resolved infrared spectroscopy. *Chemical Physics Letters*, 172:435–439, 1990.

[13] S. Woutersen and H. J. Bakker. Resonant intermolecular transfer of vibrational energy in liquid water. *Nature*, 402:507–509, 1999.

[14] Q. Du, R. Superfine, E. Freysz, and Y. R. Shen. Vibrational spectroscopy of water at the vapor/water interface. *Physical Review Letters*, 70:2313–2316, 1993.

[15] J. D. Eaves, J. J. Loparo, C. J. Fecko, S. T. Roberts, A. Tokmakoff, and P. L. Geissler. Hydrogen bonds in liquid water are broken only fleetingly. *Proceedings of the National Academy of Sciences*, 102:13019–13022, 2005.

[16] A. Vila Verde, P. G. Bolhuis, and R. Kramer Campen. Statics and dynamics of free and hydrogen-bonded OH groups at the air/water interface. *The Journal of Physical Chemistry B*, 116:9467–9481, 2012.

[17] C.-S. Hsieh, R. K. Campen, M. Okuno, E. H. G. Backus, Y. Nagata, and M. Bonn. Mechanism of vibrational energy dissipation of free OH groups at the air-water interface. *Proceedings of the National Academy of Sciences*, 110:18780–18785, 2013.

[18] T. Ishiyama and A. Morita. Molecular dynamics study of gas-liquid aqueous sodium halide interfaces. I. Flexible and polarizable molecular modeling and interfacial properties. *The Journal of Physical Chemistry C*, 111:721–737, 2007.

[19] T. Ishiyama and A. Morita. Molecular dynamics study of gas-liquid aqueous sodium halide interfaces. II. Analysis of vibrational sum frequency generation spectra. *The Journal of Physical Chemistry C*, 111:738–748, 2007.

[20] X. Wei, P. B. Miranda, and Y. R. Shen. Surface vibrational spectroscopic study of surface melting of ice. *Physical Review Letters*, 86:1554–1557, 2001.

[21] R. Superfine, J. Y. Huang, and Y. R. Shen. Nonlinear optical studies of the pure liquid/vapor interface: Vibrational spectra and polar ordering. *Physical Review Letters*, 66:1066–1069, 1991.

[22] X. Wei. *Sum-Frequency Spectroscopic Studies I. Surface Melting of Ice II. Surface Alignment of Polymers*. PhD thesis, University of California at Berkeley, 2000.

[23] D. Eisenberg and W. Kauzmann. *The Structure and Properties of Water*. OXFORD UNIV PR, 1969.

[24] A. J. Lock, S. Woutersen, and H. J. Bakker. Ultrafast energy equilibration in hydrogen-bonded liquids. *The Journal of Physical Chemistry A*, 105:1238–1243, 2001.

[25] Z. Gengeliczki, D. E. Rosenfeld, and M. D. Fayer. Theory of interfacial orientational relaxation spectroscopic observables. *The Journal of Chemical Physics*, 132:244703, 2010.

[26] S. Ashihara, N. Huse, A. Espagne, E.T.J. Nibbering, and T. Elsaesser. Vibrational couplings and ultrafast relaxation of the O-H bending mode in liquid H_2O. *Chemical Physics Letters*, 424:66–70, 2006.

[27] J. A. McGuire and Y. R. Shen. Ultrafast vibrational dynamics at water interfaces. *Science*, 313:1945–1948, 2006.

[28] M. Smits, A. Ghosh, M. Sterrer, M. Müller, and M. Bonn. Ultrafast vibrational energy transfer between surface and bulk water at the air-water interface. *Physical Review Letters*, 98:098302, 2007.

[29] M. L. Cowan, B. D. Bruner, N. Huse, J. R. Dwyer, B. Chugh, E. T. J. Nibbering, T. Elsaesser, and R. J. D. Miller. Ultrafast memory loss and energy redistribution in the hydrogen bond network of liquid H_2O. *Nature*, 434:199–202, 2005.

[30] S. Woutersen, U. Emmerichs, H.-K. Nienhuys, and H. J. Bakker. Anomalous temperature dependence of vibrational lifetimes in water and ice. *Physical Review Letters*, 81:1106–1109, 1998.

[31] Z. Zhang, L. Piatkowski, H. J. Bakker, and M. Bonn. Ultrafast vibrational energy transfer at the water/air interface revealed by two-dimensional surface vibrational spectroscopy. *Nature Chemistry*, 3:888–893, 2011.

[32] I. V. Stiopkin, C. Weeraman, P. A. Pieniazek, F. Y. Shalhout, J. L. Skinner, and A. V. Benderskii. Hydrogen bonding at the water surface revealed by isotopic dilution spectroscopy. *Nature*, 474:192–195, 2011.

[33] M. Sovago, R. Kramer Campen, H. J. Bakker, and M. Bonn. Hydrogen bonding strength of interfacial water determined with surface sum-frequency generation. *Chemical Physics Letters*, 470:7–12, 2009.

[34] K. B. Eisenthal. Measurement of intermolecular energy transfer using picosecond light pulses. *Chemical Physics Letters*, 6:155–157, 1970.

[35] S. A. Corcelli and J. L. Skinner. Infrared and Raman line shapes of dilute HOD in liquid H_2O and D_2O from 10 to 90°C. *The Journal of Physical Chemistry A*, 109:6154–6165, 2005.

[36] J. R. Schmidt, S. A. Corcelli, and J. L. Skinner. Pronounced non-Condon effects in the ultrafast infrared spectroscopy of water. *The Journal of Chemical Physics*, 123:044513, 2005.

[37] J. J. Loparo, S. T. Roberts, R. A. Nicodemus, and A. Tokmakoff. Variation of the transition dipole moment across the OH stretching band of water. *Chemical Physics*, 341:218–229, 2007.

[38] R. A. Kaindl, M. Wurm, K. Reimann, P. Hamm, A. M. Weiner, and M. Woerner. Generation, shaping, and characterization of intense femtosecond pulses tunable from 3 to 20 μm. *Journal of the Optical Society of America B*, 17:2086, 2000.

[39] A. Ghosh, M. Smits, J. Bredenbeck, N. Dijkhuizen, and M. Bonn. Femtosecond time-resolved and two-dimensional vibrational sum frequency spectroscopic instrumentation to study structural dynamics at interfaces. *Review of Scientific Instruments*, 79:093907, 2008.

[40] S. Babar and J. H. Weaver. Optical constants of Cu, Ag, and Au revisited. *Applied Optics*, 54:477, 2015.

[41] J. Sagiv. Organized monolayers by adsorption. 1. Formation and structure of oleophobic mixed monolayers on solid surfaces. *Journal of the American Chemical Society*, 102:92–98, 1980.

[42] W. Rasband. Imagej. https://imagej.nih.gov/ij/, 1997-2017.

[43] M. Brugnara. Contact angle plugin (for imagej software). https://imagej.nih.gov/ij/plugins/contact-angle.html, 2006.

[44] W. Hua, D. Verreault, E. M. Adams, Z. Huang, and H. C. Allen. Impact of salt purity on interfacial water organization revealed by conventional and heterodyne-detected vibrational sum frequency generation spectroscopy. *The Journal of Physical Chemistry C*, 117:19577–19585, 2013.

[45] S. Ye, S. Nihonyanagi, and K. Uosaki. Sum frequency generation (SFG) study of the pH-dependent water structure on a fused quartz surface modified by an octadecyltrichlorosilane (OTS) monolayer. *Physical Chemistry Chemical Physics*, 3:3463–3469, 2001.

[46] A. Eftekhari-Bafrooei, S. Nihonyanagi, and E. Borguet. Spectroscopy and dynamics of the multiple free OH species at an aqueous/hydrophobic interface. *The Journal of Physical Chemistry C*, 116:21734–21741, 2012.

[47] D. E. Goldsack and R. Franchetto. The viscosity of concentrated electrolyte solutions. I. Concentration dependence at fixed temperature. *Canadian Journal of Chemistry*, 55:1062–1072, 1977.

[48] D. K. Chattoraj and K. S. Birdi. *Adsorption and the Gibbs Surface Excess*. Springer US, 1984.

[49] A. W. Omta, M. F. Kropman, S. Woutersen, and H. J. Bakker. Negligible effect of ions on the hydrogen-bond structure in liquid water. *Science*, 301:347–349, 2003.

[50] J. W. Gibbs. *The Collected Works of J. W. Gibbs*. 1928.

[51] L. Onsager and N. N. T. Samaras. The surface tension of Debye-Hückel electrolytes. *The Journal of Chemical Physics*, 2:528–536, 1934.

[52] T. Yamaguchi, O. Lindqvist, T. Claeson, and J. B. Boyce. EXAFS and X-ray diffraction studies of the hydration structure of stereochemically active Sn(II) ions in aqueous solution. *Chemical Physics Letters*, 93:528–532, 1982.

[53] Y. Kameda, H. Saitoh, and O. Uemura. The hydration structure of NO_3^- in concentrated aqueous sodium nitrate solutions. *Bulletin of the Chemical Society of Japan*, 66:1919–1923, 1993.

[54] T. Yamaguchi, M. Niihara, T. Takamuku, H. Wakita, and H. Kanno. Scandium(III) hydration in aqueous solution from X-ray diffraction and X-ray absorption fine structure measurements. *Chemical Physics Letters*, 274:485–490, 1997.

[55] J. C. Hindman, A. Svirmickas, and M. Wood. Relaxation processes in water. A study of the proton spin-lattice relaxation time. *The Journal of Chemical Physics*, 59:1517–1522, 1973.

[56] D. W. G. Smith and J. G. Powles. Proton spin-lattice relaxation in liquid water and liquid ammonia. *Molecular Physics*, 10:451–463, 1966.

[57] M. F. Kropman and H. J. Bakker. Dynamics of water molecules in aqueous solvation shells. *Science*, 291:2118–2120, 2001.

[58] M. F. Kropman and H. J. Bakker. Femtosecond mid-infrared spectroscopy of aqueous solvation shells. *The Journal of Chemical Physics*, 115:8942–8948, 2001.

[59] A. Einstein. Investigations on the theory of the Brownian movement. *Fürth, Methuen, London*, 1926.

[60] R. Buchner, T. Chen, and G. Hefter. Complexity in "simple" electrolyte solutions: Ion pairing in $MgSO_4$(aq). *The Journal of Physical Chemistry B*, 108:2365–2375, 2004.

[61] W. Wachter, Š. Fernandez, R. Buchner, and G. Hefter. Ion association and hydration in aqueous solutions of LiCl and Li_2SO_4 by dielectric spectroscopy. *The Journal of Physical Chemistry B*, 111:9010–9017, 2007.

[62] R. Buchner, S. G. Capewell, G. Hefter, and P. M. May. Ion-pair and solvent relaxation processes in aqueous Na_2SO_4 solutions. *The Journal of Physical Chemistry B*, 103:1185–1192, 1999.

[63] I. Benjamin. Theoretical study of ion solvation at the water liquid-vapor interface. *The Journal of Chemical Physics*, 95:3698–3709, 1991.

[64] M. A. Wilson and A. Pohorille. Interaction of monovalent ions with the water liquid-vapor interface: A molecular dynamics study. *The Journal of Chemical Physics*, 95:6005–6013, 1991.

[65] G. Markovich, R. Giniger, M. Levin, and O. Cheshnovsky. Photoelectron spectroscopy of negative ions solvated in clusters. *Zeitschrift für Physik D Atoms, Molecules and Clusters*, 20:69–72, 1991.

[66] G. Markovich, S. Pollack, R. Giniger, and O. Cheshnovsky. Photoelectron spectroscopy of Cl^-, Br^-, and I^- solvated in water clusters. *The Journal of Chemical Physics*, 101:9344–9353, 1994.

[67] L. Perera and M. L. Berkowitz. Many-body effects in molecular dynamics simulations of $Na^+(H_2O)_n$ and $Cl^-(H_2O)_n$ clusters. *The Journal of Chemical Physics*, 95:1954–1963, 1991.

[68] L. Perera and M. L. Berkowitz. Structure and dynamics of $Cl^-(H_2O)_{20}$ clusters: The effect of the polarizability and the charge of the ion. *The Journal of Chemical Physics*, 96:8288–8294, 1992.

[69] L. Perera and M. L. Berkowitz. Stabilization energies of Cl^-, Br^-, and I^- ions in water clusters. *The Journal of Chemical Physics*, 99:4222–4224, 1993.

[70] L. Perera and M. L. Berkowitz. Structures of $Cl^-(H_2O)_n$ and $F^-(H_2O)_n$ (n=2,3,...,15) clusters. Molecular dynamics computer simulations. *The Journal of Chemical Physics*, 100:3085–3093, 1994.

[71] L. S. Sremaniak, L. Perera, and M. L. Berkowitz. Enthalpies of formation and stabilization energies of $Br^-(H_2O)_n$ (n=1,2, ..., 15) clusters. Comparisons between molecular dynamics computer simulations and experiment. *Chemical Physics Letters*, 218:377–382, 1994.

[72] I.-C. Yeh, L. Perera, and M. L. Berkowitz. Photodetachment spectra of $Cl^-(H_2O)_n$ clusters. Predictions and comparisons. *Chemical Physics Letters*, 264:31–38, 1997.

[73] L. X. Dang and B. C. Garrett. Photoelectron spectra of the hydrated iodine anion from molecular dynamics simulations. *The Journal of Chemical Physics*, 99:2972–2977, 1993.

[74] L. X. Dang and D. E. Smith. Molecular dynamics simulations of aqueous ionic clusters using polarizable water. *The Journal of Chemical Physics*, 99:6950–6956, 1993.

[75] L. X. Dang. Characterization of water octamer, nanomer, decamer, and iodide-water interactions using molecular dynamics techniques. *The Journal of Chemical Physics*, 110:1526–1532, 1999.

[76] S. J. Stuart and B. J. Berne. Effects of polarizability on the hydration of the chloride ion. *The Journal of Physical Chemistry*, 100:11934–11943, 1996.

[77] S. J. Stuart and B. J. Berne. Surface curvature effects in the aqueous ionic solvation of the chloride ion. *The Journal of Physical Chemistry A*, 103:10300–10307, 1999.

[78] G. H. Peslherbe, B. M. Ladanyi, and J. T. Hynes. Structure of NaI ion pairs in water clusters. *Chemical Physics*, 258:201–224, 2000.

[79] S. Ghosal, A. Shbeeb, and J. C. Hemminger. Surface segregation of bromine in bromide doped NaCl: Implications for the seasonal variations in arctic ozone. *Geophysical Research Letters*, 27:1879–1882, 2000.

[80] P. Jungwirth and D. J. Tobias. Ions at the air/water interface. *The Journal of Physical Chemistry B*, 106:6361–6373, 2002.

[81] J. H. Hu, Q. Shi, P. Davidovits, D. R. Worsnop, M. S. Zahniser, and C. E. Kolb. Reactive uptake of Cl_2(g) and Br_2(g) by aqueous surfaces as a function of Br^- and I^- ion concentration: The effect of chemical reaction at the interface. *The Journal of Physical Chemistry*, 99:8768–8776, 1995.

[82] E. M. Knipping, M. J. Lakin, K. L. Foster, P. Jungwirth, D. J. Tobias, R. B. Gerber, D. Dabdub, and B. J. Finlayson-Pitts. Experiments and simulations of ion-enhanced interfacial chemistry on aqueous NaCl aerosols. *Science*, 288:301–306, 2000.

[83] P. Jungwirth and D. J. Tobias. Surface effects on aqueous ionic solvation: A molecular dynamics simulation study of NaCl at the air/water interface from infinite dilution to saturation. *The Journal of Physical Chemistry B*, 104:7702–7706, 2000.

[84] E. A. Raymond and G. L. Richmond. Probing the molecular structure and bonding of the surface of aqueous salt solutions. *The Journal of Physical Chemistry B*, 108:5051–5059, 2004.

[85] P. Terpstra, D. Combes, and A. Zwick. Effect of salts on dynamics of water: A raman spectroscopy study. *The Journal of Chemical Physics*, 92:65–70, 1990.

[86] F. Rull and J. A. de Saja. Effect of electrolyte concentration on the raman spectra of water in aqueous solutions. *Journal of Raman Spectroscopy*, 17:167–172, 1986.

[87] N. Abe and M. Ito. Effects of hydrogen bonding on the Raman intensities of methanol, ethanol and water. *Journal of Raman Spectroscopy*, 7:161–167, 1978.

[88] P. Ayotte, G. H. Weddle, J. Kim, and M. A. Johnson. Vibrational spectroscopy of the ionic hydrogen bond: Fermi resonances and ion-molecule stretching frequencies in the binary $X^{-}\cdot H_2O$ (X = Cl, Br, I) complexes via argon predissociation spectroscopy. *Journal of the American Chemical Society*, 120:12361–12362, 1998.

[89] P. Ayotte, G. H. Weddle, and M. A. Johnson. An infrared study of the competition between hydrogen-bond networking and ionic solvation: Halide-dependent distortions of the water trimer in the $X^{-}\cdot(H_2O)_3$, (X=Cl, Br, I) systems. *The Journal of Chemical Physics*, 110:7129–7132, 1999.

[90] D. Liu, G. Ma, L. M. Levering, and H. C. Allen. Vibrational spectroscopy of aqueous sodium halide solutions and air-liquid interfaces: Observation of increased interfacial depth. *The Journal of Physical Chemistry B*, 108:2252–2260, 2004.

[91] G. Archontis, E. Leontidis, and G. Andreou. Attraction of iodide ions by the free water surface, revealed by simulations with a polarizable force field based on Drude oscillators. *The Journal of Physical Chemistry B*, 109:17957–17966, 2005.

[92] E. C. Brown, M. Mucha, P. Jungwirth, and D. J. Tobias. Structure and vibrational spectroscopy of salt water/air interfaces: Predictions from classical molecular dynamics simulations. *The Journal of Physical Chemistry B*, 109:7934–7940, 2005.

[93] L. Vrbka, M. Mucha, B. Minofar, P. Jungwirth, E. C. Brown, and D. J. Tobias. Propensity of soft ions for the air/water interface. *Current Opinion in Colloid & Interface Science*, 9:67–73, 2004.

[94] S. Ghosal, J. C. Hemminger, H. Bluhm, B. S. Mun, E. L. D. Hebenstreit, G. Ketteler, D. F. Ogletree, F. G. Requejo, and M. Salmeron. Electron spectroscopy of aqueous solution interfaces reveals surface enhancement of halides. *Science*, 307:563–566, 2005.

[95] C. Tian, S. J. Byrnes, H.-L. Han, and Y. Ron Shen. Surface propensities of atmospherically relevant ions in salt solutions revealed by phase-sensitive sum frequency vibrational spectroscopy. *The Journal of Physical Chemistry Letters*, 2:1946–1949, 2011.

[96] L. Piatkowski, Z. Zhang, E. H. G. Backus, H. J. Bakker, and M. Bonn. Extreme surface propensity of halide ions in water. *Nature Communications*, 5, 2014.